Full-metal antennas based on magnified 3D discrete lenses : additive manufacturing and space applications

Lisa Berretti

COLLEGE MATHS, TELECOMS
DOCTORAL INFORMATIQUE, SIGNAL
BRETAGNE SYSTEMES, ELECTRONIQUE

INSA INSTITUT NATIONAL DES SCIENCES APPLIQUÉES RENNES

THÈSE DE DOCTORAT DE

L'INSTITUT NATIONAL DES SCIENCES APPLIQUÉES DE RENNES

ÉCOLE DOCTORALE N° 601
Mathématiques, Télécommunications, Informatique, Signal, Systèmes, Électronique
Spécialité : *Électronique*

Par
Lisa BERRETTI

Full-metal antennas based on magnified 3D discrete lenses : additive manufacturing and space applications

Thèse présentée et soutenue à Rennes, France, le 6 Février 2024
Unité de recherche : IETR (UMR 6164)
Thèse N° : 24ISAR 01 / D24 - 01

Rapporteurs avant soutenance :

Cyrille MENUDIER	Professeur des Universités, XLIM - Université de Limoges, France
Paolo ROCCA	Maitre de Conférences, HdR, Université de Trento, Italie
Pablo PADILLA	Maitre de Conférences, HdR, Université de Granada, Espagne

Composition du Jury :

Président :	Cyrille MENUDIER	Professeur des Universités, XLIM - Université de Limoges, France
Examinateurs :	Elodie RICHALOT	Professeure des Universités, Université de Gustave Eiffel, France
	Dimitra PSYCHOGIOU	Professeure, Université de Cork, Irlande
Dir. de thèse :	María GARCÍA-VIGUERAS	Maîtresse de Conférences, HdR, INSA, Rennes, France
Co-encadr. de thèse :	Renaud LOISON	Professeur, INSA, Rennes, France

Invités :

Giovanni TOSO	Docteur et ingénieur, European Space Agency (ESA), Pays-Bas
Esteban MENARGUES	Ingénieur, SWISSto12, Renens, Suisse

Acknowledgement

I believe that the proverb "it takes a village to raise a child" perfectly describes my experience as a PhD student. I am firmly convinced that this journey has only been possible with the support of a whole community that has contributed to make this PhD journey fantastic. For this reason, I would like to express my deep appreciation to all those who have participated in it.

First of all, I must express my gratitude to the exceptional research team that I have been privileged to be a part of. Their mentorship has been absolutely essential in shaping both my academic research and personal development over the past three years.

I wish to thank with my sincerest appreciation to my PhD supervisor, Prof. María García-Vigueras. Your guidance from the beginning of this thesis has been invaluable. Your rigor and energy have inspired me to excel and truly enjoy my work. Thank you for your support, which has been indispensable to me.

I extend my deep gratitude to my PhD co-supervisor, Prof. Renaud Loison. Your insightful mentorship has emphasized my curiosity, delving into the depths of my research field. I really appreciate the knowledge you have shared with me and the time spent collaborating together.

I thank my ESA's referent, Dr. and Ing. Giovanni Toso, for believing in me from the first day we met in 2019. It has been a pleasure to work with you and to experience the ESTEC this time in real life. I really appreciate your involvement in the project.

Lastly, I extend my thanks to Ing. Esteban Menargues of SWISSto12 for generously sharing your invaluable industry insights with me. Your suggestions have been very valuable, and I appreciate the knowledge gained from our interactions.

I would like to acknowledge all the committee members of the jury: Prof. Cyrille Menudier, Prof. Pablo Padilla, Prof. Paolo Rocca, Prof. Dimitra Psychogiou, Prof. Elodie Richalot for your invaluable suggestions and for accepting to participate in my

final defence. A special thanks to the reviewers for their diligent work in revising the manuscript in detail in the months leading up to my thesis defence and to all the comments received.

I am very grateful to those who have collaborated with me along the way: Dr. and Ing. Santiago Capdevila from SWISSto12, thank you for the numerous feedbacks on meandered waveguides and the VBA code at the beginning of my thesis. Also to Dr. and Ing. Lucas Polo-López from INSA, for your past and present collaborations. It has been a pleasure not only to work together, but also to share many moments with you as a friend.

To my colleagues who have shared this journey with me from the beginning here in Bretagne. Thank you very much: Baptiste, Clement, Corentin, Diego, Erwan, Guillaume, Hugo, Jean Claude, Matthieu, Mats and Sarah. I will always remember our time spent together with each of you.

Thanks also to all the colleagues in Building 6, it is a pleasure to work at INSA. I have to admit that, although I am Italian, my caffeine intake has increased significantly due to the many coffee breaks! In any case, it has been very enriching to share and interact with all of you, thank you all.

I am grateful to the RF Microwave and Electromagnetics Group at the University of Florence, headed by Stefano Selleri, where I completed my Master's and Bachelor's theses. It was in this welcoming environment that I was introduced to the world of research, setting me on the path towards a PhD.

If I am standing here today, it is because I have been supported even from Italy (and not only).

Thank you for my second heart, MAMMA Claudia and BABBO Daniele (yes, we say that in maremmano). Mamma, thank you for loving me and allowing me to fly, to build my life in the happiest way possible. Babbo, I am sure that you are proud of me and of my path so far. You are always with me.

I would also like to express my strongest gratitude to the person who shares my daily life, Eva. Thank you, my companion, for believing in me and giving me strength when I do not have it. I am very happy and lucky to have met you on my way.

I would like to thank all of my family that I love and always miss. You are the people that I will never forget in my life. Thanks to: Adua, Alessandra, Andrea, Annalena, Barbara, Enna, Enzo, Filippo, Franca, Giulia, Guglielmo, Ivo, Jode, Julius, Leonard, Licia, Loris, Luda, Mara, Marie, Matilde, Niccolò, Nicola, Nina Viola, Omero, Paola, Rina,

Roberta, Sandra, Sandro.

I would also like to thank my Castiglione's friends, who have always been there for me, even though we are kilometers apart. Thank you from the bottom of my heart to the Galline: Alessandra, Benedetta, Camilla, Gioia, Lucia, Maria Caterina, Martina and Sole. And to my favorite group of crazy people: the Mean Extra, Jessy and Pasto, I miss you!

From Santa Marta with love: I want to thank the companions who journeyed through university with me. Thanks to Claudia, Faber, Fedez, Pagno, and Rachele. Without you, this experience would have not been possible. I still remember our times together, from Francesca's meals, to attending Landu's courses!

To my adopted grandparents from the Netherlands-Montreal axis, Hoda and Mahdi. The memories we made together in Leiden hold a special place in my heart. Thanks also to the most funniest and lovely cats Cyrano and Arpege!

A strong thanks also to Maria Elena, Roberta, Tamara, as well as Luchino, Carlino, and Lele Minimale, and their entire family, for the kindness, even when if we don't see each other for a long time.

Thanks to Eva's Breton family, who supported me on this journey and whom I cherish, even when they joke about butter and Italy.

I dedicate this PhD thesis to all these people who have contributed to making this journey truly remarkable and have played a part in shaping the woman I have become today.

...Now it is time to leave because I still have to prepare my TIRAMISU for the "pot de thèse" of tomorrow!

Note for Readers: In the digital format, you can easily navigate through each chapter, section, figure, table, equation, reference and acronym by simply clicking on them.

Enjoy your reading!

Table of Contents

Acronyms

2D Two-Dimensional

3D Three-Dimensional

AA Active Antenna

AFSIW Air-Filled Substrate Integrated Waveguide

AM Additive Manufacturing

BFN Beam-Forming Network

CST CST Microwave Studio

DMLS Direct Metal Laser Sintering

DoF Degree of Freedom

EQA Evanescent Quadridge Antenna

FDM Fused Deposition Modeling

FoV Field-of-View

GaN Gallium Nitride

GEO Geostationary Earth Orbit

GL Grating-Lobe

GO Geometrical Optics

LEO Low Earth Orbit

LHCP Left-Hand Circular Polarization

MEO Medium Earth Orbit

MFPB Multiple-Feed-Per-Beam

MW Meandered Waveguide

PCB Printed Circuit Boards

PEW Perfect Electric Wall

PMW Perfect Magnetic Wall

PPW Parallel-Plate Waveguide

RA Reflect Array

RF Radio-Frequency

RHCP Right-Hand Circular Polarization

RMW Ridged Meandered Waveguide

Rx Reception

SFPB Single-Feed-Per-Beam

SIW Substrate Integrated Waveguide

SLA Stereolitography

SLM Selective Laser Melting

TA Transmit Array

TEM Transverse Electro-Magnetic

TM Traditional Manufacturing

Tx Transmission

XPD Cross-Polar Discrimination

Introduction

Context and motivation

Nowadays, we are experiencing a drastic change in the space industry which is in line with the New Space paradigm as a leap forward in terms of very high throughput and data rates, network connectivity, reliability and high efficiency but also a democratization of space and the appearance of small constellation of satellites [1]–[4].

Flexibility has become a priority in the design of Radio-Frequency (RF) systems, mainly in terms of coverage, power allocation, spectrum use, polarization and number and shape of the beams. Such flexibility is required both, at ground and non-terrestrial levels [5]–[7]. Multibeam reconfiguration, beam-hopping techniques, frequency and polarization reuse are indeed on the verge of becoming some of the requirements of the emerging systems [8]–[10]. In addition to such flexibility, high power handling comes as an additional requirement when considering space applications. Namely, due to the need to assure a link budget with the satellite. Hence, the role and position of the radiating antenna is crucial in the design of such systems and in particular, it represents one of the motivations of the present thesis.

The antenna solution providing the highest flexibility is the Active electronically steerable Antenna (AA). Differently from passive antennas, AAs allow for electronic (without mechanically movable parts) mission reconfiguration (i.e. flexible number of beams, and for each beam, flexible steering, flexible beam-shape or flexible power allocation). We are witnessing a common trend in the space industry nowadays, related to the development of flexible payloads (e.g. Eutelsat Quantum [11], Hispasat 36W-1 [12], OneSat [13], HummingSat [14] (Europe) or Winds [15] (Japan)). Analogously, these new solutions based on AAs have been introduced for ground applications (e.g.

new concept of arrays as gateway antennas from: Thinkom [16], Starlink [17]). However, the introduction of these features means increased manufacturing costs and complexity in incorporating amplification, cooling modules, digital processing, real-time calibration blocks. It also leads to a subsequent increase in losses and energy consumption.

The challenge to make AAs more affordable is a great source of motivation, both at industry and research levels. Efforts are being made in order to reduce their complexity, and to increase their power efficiency, such as sparse or irregular arrays [18], [19], hybrid payloads [20], improvement of Gallium Nitride (GaN) technology [21].

One of the main motivations for this thesis is to further explore a promising antenna architecture known as Three-Dimensional (3D) discrete lens [22]. This antenna holds strong potential for the implementation of AA as it offers a trade-off between complexity and flexibility.

On the fabrication side, Additive Manufacturing (AM) or 3D printing [23]–[25] has been identified as one of the enabling technologies that can contribute to ease the development of AAs [26]. Exploring the potential of AM is another motivation of the present thesis. The use of AM techniques in the design of RF components has represented an appealing opportunity to reach enhanced design freedom, but also to reduce volume and costs an enhance RF performances. This evolution spans from applying metallic coatings onto 3D printed plastic components, such as those produced through Stereolitography (SLA) [27], [28], to the emergence of full-metal AM methods like Selective Laser Melting (SLM) [29] and Direct Metal Laser Sintering (DMLS) [30]. These advanced methods achieve high degrees of flexibility, allowing the integration of complex geometries into single-piece components while simultaneously reducing losses, saving energy and allowing high power handling — a capability that conventional manufacturing approaches cannot replicate [31]–[33].

Objectives and research hypotheses

This thesis aims to propose innovative solutions of AAs with reduced cost and flexibility. The main objectives are outlined as follows:

- design of high-gain multibeam antennas;
- develop systems with low losses and high efficiency;
- enable dual polarization and broad bandwidth capabilities;

- enhance capacity and simplify the system accommodation.

The work presented in this thesis is based on the hypothesis that exploiting magnification factors in 3D discrete lenses, and with the implementation of AM, can lead to AAs with reduced cost and high flexibility. These systems can support large frequency bandwidths and allow for dual polarization features. In addition, they can be employed in various scenarios, spanning both narrow and wide Field-of-Views (FoVs).

Organization of the thesis

The thesis is subdivided into four chapter:

- Chapter 1 shows an overview on antennas providing different means to reach flexible operation, high efficiency and a good trade-off between cost and complexity. First of all, a comparison on highly efficient full-metal antennas to provide multibeam scanning and high power handlings is provided. Subsequently, antennas fabricated via full-metal AM are introduced, with an analysis of their principal strengths and weak points. Finally, the proposal to focus on 3D discrete lens systems in waveguide technology through AM and their characterization is provided.
- Chapter 2 focuses on Meandered Waveguides (MWs) as an innovative solution employed in full-metal 3D discrete lenses to allow spatial routing between the two radiating profiles. First, the general guidelines to build the modulated trajectories are pointed out. Then, the phase delay synthesis is performed, proposing examples with exotic meanderings and comparing expected and simulated results. Additionally, some implementations of MW through 3D cluster are presented.
- Chapter 3 deals with the design of 3D discrete lenses for narrow FoV scenarios. The general lens architecture to target such applications is firstly described and then, the implementation in waveguide technology is investigated. In particular, a 3D discrete lens for Geostationary Earth Orbit (GEO) scenario implementing the MW cluster in a 7x7 system is proposed and simulated in all its parts. While in the end, a smaller prototype is manufactured and measured to show the real reached performance.
- Chapter 4 presents a 3D discrete lens for wide FoV scenarios. The first section provides an overview of the overall structure, offering a comprehensive descrip-

tion of each constitutive element. Meanwhile, the second section is dedicated to the finite lens analysis and its validation process. A detailed explanation of a rigorous full-wave methodology for simulating large arrays is then provided, along with a validation case study. Finally, the simulation results of the examined lens are presented.

CHAPTER 1

State of the art

Present and next generations of space and ground platforms for telecommunications services require progressively dedicated antennas to cope with the rising demands of global connectivity, improved data transmission speeds and high power handlings [5]–[7].

To tackle these demands, innovative radiative systems have been developed to face the trade-off between reconfigurability (in terms of beam pointing, power, frequency, and polarization), cost and accommodation [9], [10]. In particular, electronically steerable high-gain antennas are required to achieve multiple spot beams implementing frequency, polarization reuse and power allocation to provide global regular or irregular coverages (such as the multi spot beam European coverage depicted in Fig. 1.1a or the irregular shaped one showed in Fig. 1.1b).

Space constitutes an extremely harsh environment for RF equipment [36], [37]. Various phenomena can occur, including substantial thermal gradients (e.g. $\Delta T = [-150, 150]^{\circ}$), exposure to radiations, out-gassing from plastic materials and the risk of electrostatic discharge to name a few. Due to these factors, the preferred approach for attaining an high power handling systems with minimal insertion losses is to use metallic materials. High power handling is a well known requirement in space systems, both on-ground and on-board. It is the need for flexibility that comes as an new requirement [5]. The antenna solutions that will be considered in this chapter will be fully metallic.

This chapter presents a state of the art on full-metal space antenna systems providing some degrees of flexibility. The first section focuses on high-gain antennas achieving

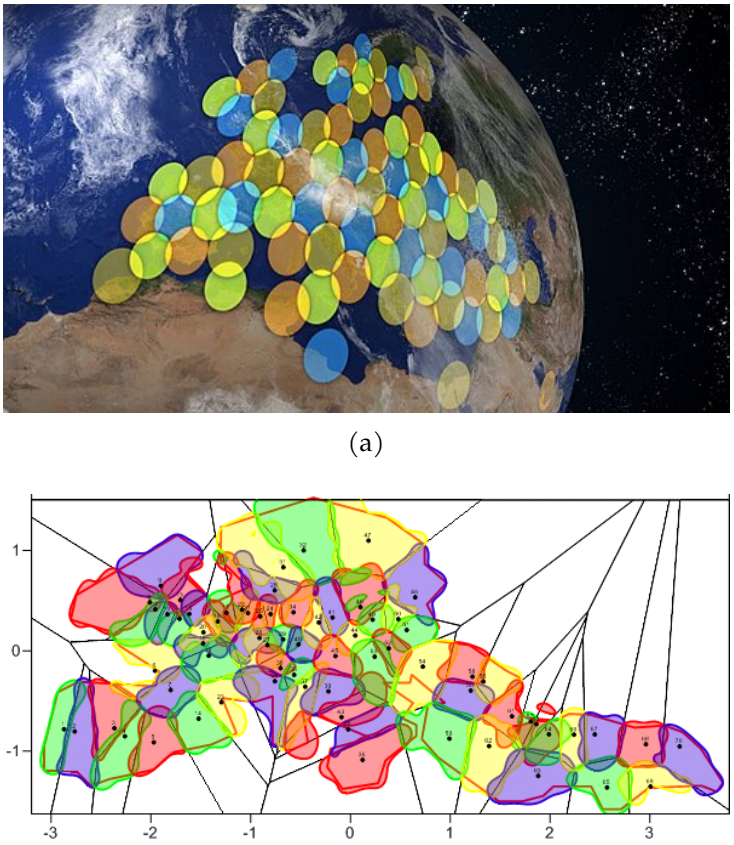

(a)

(b)

Figure 1.1 – (a) Eutelsat's KA-SAT satellite [34] spot beams coverage over Europe and the Mediterranean Basin (different colors show frequency reuse) (from Wikipedia). (b) Irregular European coverage based on tesselation polygons (from [35]).

multibeam scanning, showing a comparison between several full-metal configurations as high power handling solutions. Secondly, the AM technology is introduced to fabricate full-metal radiators. This technology not only facilitates the production of highly complex geometric designs but also contributes significantly to reducing overall weight and volume. Finally, a solution based on 3D discrete lenses is presented, which can be fabricated through full-metal AM, offering a valuable compromise between performances and ease of fabrication.

1.1 High-gain multibeam antennas for space

This section offers a comprehensive comparison on the antenna systems that are mainly been developed providing some kind of flexible operation.

In the following, we can distinguish solutions based on reflectors, antenna arrays, and lenses. Each solution is examined individually, highlighting the associated strengths and weaknesses. Towards the conclusion, a comparison of the potential solutions is then briefly showed. Specifically, the comparison considers RF performances in terms of scanning capabilities, feasibility in active control implementation, dual polarization features, frequency bandwidth, cost and complexity of the system and volume accommodation. The aim is to highlight their main advantages and disadvantages while identifying the potential configuration that will be studied in the next chapters.

1.1.1 Reflector-based antennas

Reflector-based antennas are often chosen in space applications for their robust performance and broad bandwidth. The fundamental operational concept of a typical parabolic reflector [38] is illustrated in Fig. 1.2.

These antennas have the versatility to be utilized for both transmission (Tx) and reception (Rx) modes. They typically feature a reflective surface (indicated in red) that focuses electromagnetic energy towards a feed (depicted as a green dot), which is placed in the focal point. In particular, the position of the focal point permits the transformation of spherical wavefronts into flat parallel wavefronts toward the desired directions. In the Rx mode, reflector antennas collect incoming signals towards the focal point; while for Tx, they propagate signals from the focal point towards the desired direction.

Reflector dishes can be found using different shapes (e.g. parabolic or spherical are the most common ones). Typically, these antennas are constructed from lightweight materials, such as metals or composites, to reduce the overall weight of the system. In modern applications, the feeding component of these antennas can be based on various elements, including arrays, lens antennas or additional reflectors, in order to enhance the antenna's performance, as detailed in [39].

In space-borne payloads, reflector antennas are usually employed using a Single-Feed-Per-Beam (SFPB) configuration [40], [41]. The most consolidated passive antenna solution to create multiple beams is based on 3 or 4 reflectors generating inter-

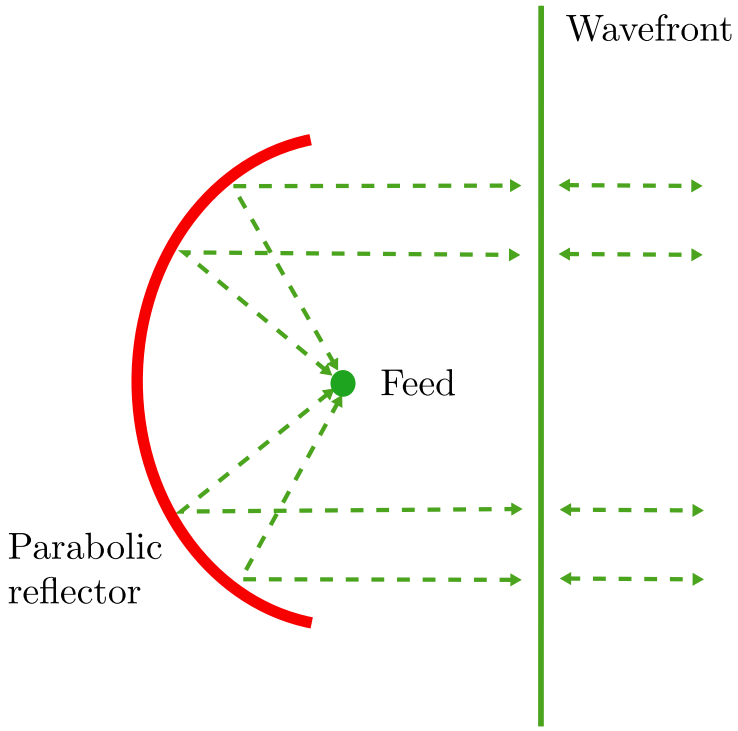

Figure 1.2 – Working principle of a generic parabolic reflector.

leaved beams and using one feed for every beam. The introduction of this solution is justified by the challenge of implementing a single reflector that can efficiently accommodate a group of directive feeds while simultaneously achieving a crossover level around -4 dB, high isolation and providing a multibeam coverage [41].

To exemplify this, various industrial products employing the SFPB configuration are provided as examples: Anik-F2 (in Ka-band) [42], Spaceway-3 Ka-Sat [34], IPSTAR (Thaicom-4) [43] in Ku-band, and Eutelsat 172B [44]. Two of these products are visually represented in Fig. 1.3. On the left, Ka-Sat is characterized by four reflectors operating in Ka-band, while on the right, Eutelsat features three reflectors working in Ku-Band and three in C-band. Both of these satellites are positioned in GEO.

The main drawbacks of the SFPB configuration are related to the significant volume required to accommodate multiple reflectors within a single platform and the limited flexibility in achieving multibeam scanning as well as the possibility to provide reconfigurable beams. To overcome the issue of the accommodation of multiple reflectors, the Multiple-Feed-Per-Beam (MFPB) configuration has been introduced in the scientific literature [40], [41]. MFPB solutions exploit overlapped sub-arrays connected to Beam-Forming Networks (BFNs) to feed the single reflector. Overlapped sub-arrays

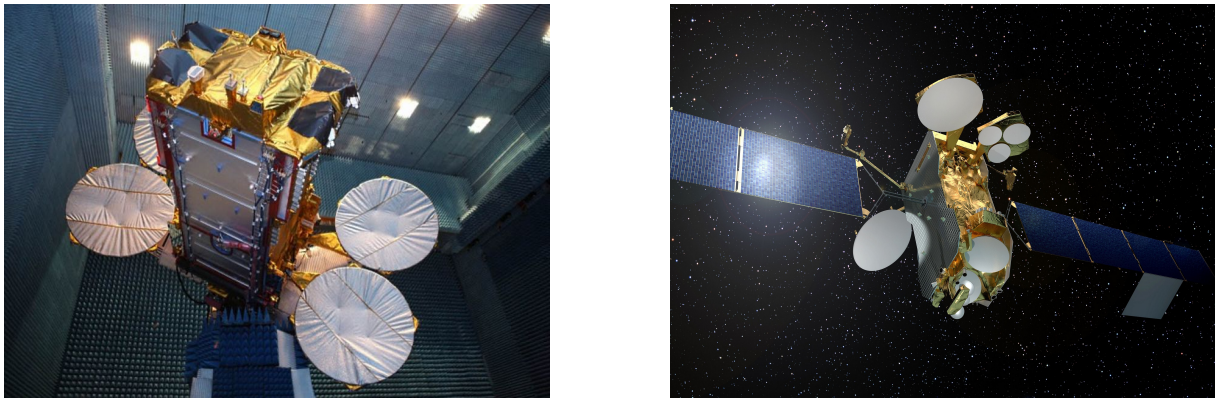

(a) (b)

Figure 1.3 – Satellites implementing SFPB configuration employing multiple reflectors. (a) Ka-Sat (launched in December 2010) (from [34]), (b) Eutelsat 172B (launched in June 2017) (from Wikipedia).

share some radiating elements with the contiguous sub-arrays to enable multi spots coverage, without increasing spillover losses and crossover levels [40]. In the example reported in Fig. 1.4, a specific MFPB feed cluster is depicted on the right and the correspondent sub-array overlapping scheme is shown on the left. In fact, in order to generate a multibeam coverage with a good isolation and crossover levels around -4 dB, multiple colors (i.e. different frequencies and polarisations) are exploited.

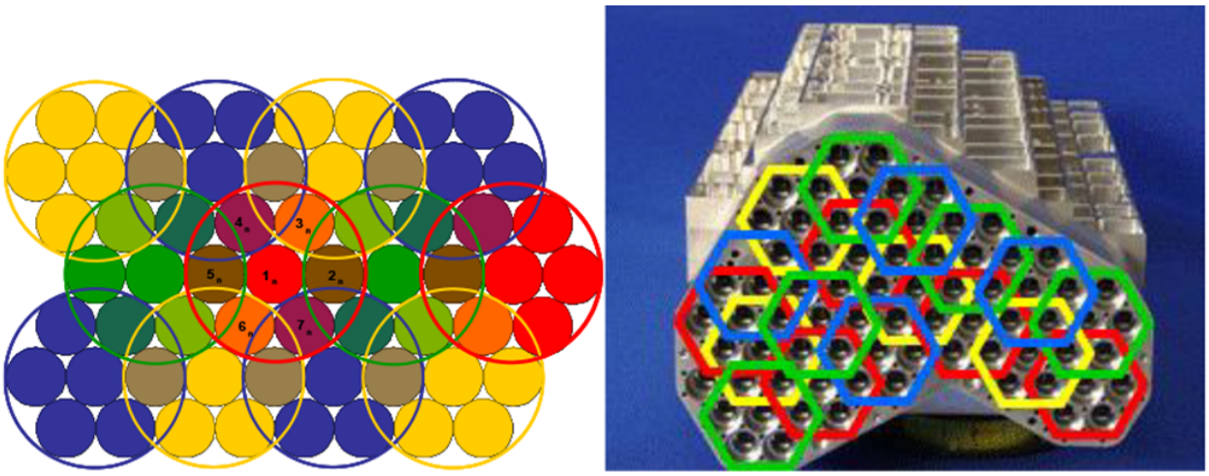

Figure 1.4 – Example of schematic MFPB cluster feed of a reflector antenna based on an overlapped sub-arrays configuration as feeding network (from [45]).

This solution leads to more flexibility employing only one reflector, at the cost of increasing the complexity of the BFNs at the feed level. An illustration of a cluster feed

and associated BFN employed in a MFPB setup for the Medusa Tx cluster [45], [46] can be observed into details in Fig. 1.5. These systems are characterized by complex BFN geometries in order to reduce the volume and the accommodation of multiple reflectors of the SFPB configuration. Additional examples of MFPB reflector configurations can be found in [47].

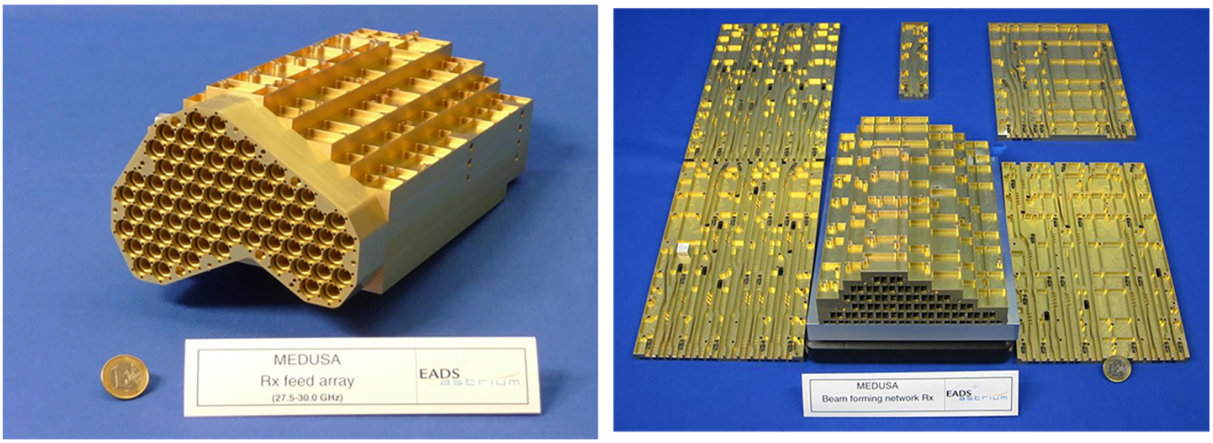

Figure 1.5 – Medusa Tx feed cluster and its BFN (from [45]).

The same trend is observed in the RF systems envisioned to be deployed on-ground. Reflectors are typically employed in gateways to control Low Earth Orbit (LEO) satellites to point beams up to low elevation angles (i.e. 15 degrees as measured from the horizon) [5]. These antennas frequently employ multiple reflectors equipped with mechanical scanning systems to follow the movements of the satellite. Typically, each reflector generates a single beam and it is used to connect to a single satellite. For this reason, it is crucial to ensure multibeam flexibility by installing multiple reflectors. Some solutions of ground-based reflectors [48] provided by Intelsat are shown in Fig. 1.6. The solution installed in Fuchsstadt (on the left) is characterized by over 70 antennas connecting three oceans and providing service to five continent. The other solution based in Atlanta (on the right) is characterized by 66 antennas supporting access to satellites with connectivity to a global network of commercial teleports. This illustration serves to emphasize the vast physical footprints that these installations require on-ground gateways. These systems tend to be extremely expensive since a separation is needed between the reflectors and significant costs are associated to their maintenance. Furthermore, their flexibility in scanning is limited because their configurations in very large arrays are based mainly on mechanical steering systems.

(a) (b)

Figure 1.6 – Reflectors for ground-based applications produced by Intelsat. (a) Fuchsstadt Teleport – Fuchsstadt, Germany (from [48]). (b) Atlanta Teleport – Ellenwood, Georgia (from [48]).

Reflector-based antennas implemented for both on-ground or on-board space applications offer the advantage of a broad frequency bandwidth. They provide also the possibility to achieve dual polarization, depending on the chosen feed chain. However, the common limitation they face is their inability to incorporate active controls in the reflector aperture to optimize its illumination efficiency. This constraint can impact their performance when compared to antennas that can actively manipulate the radiated field over the aperture.

1.1.2 Antenna arrays

In this subsection the more representative solutions of antenna arrays are presented including reflectarrays and transmitarrays as potential alternative configurations of conventional arrays.

An array of antennas can be seen as a group of multiple antennas fed simultaneously and connected to a shared receiver or transmitter to enhance gain and directivity in a specific direction. They are primarily used in applications like wireless communications to amplify sensitivity and improve signal reception. A particular sub-group of antenna arrays, known as phased arrays, can be found in space applications [49].

Phased arrays [50], [51] (depicted in Fig. 1.7) are still characterized by multiple antennas working together (highlighted in blue), but this time they introduce the capability to individually control the amplitude and phase of each element (displayed inside the red box). These precise controls allow for advanced operation modes like

beamforming and broad scanning flexibility across multiple desired directions, making them particularly valuable in this context.

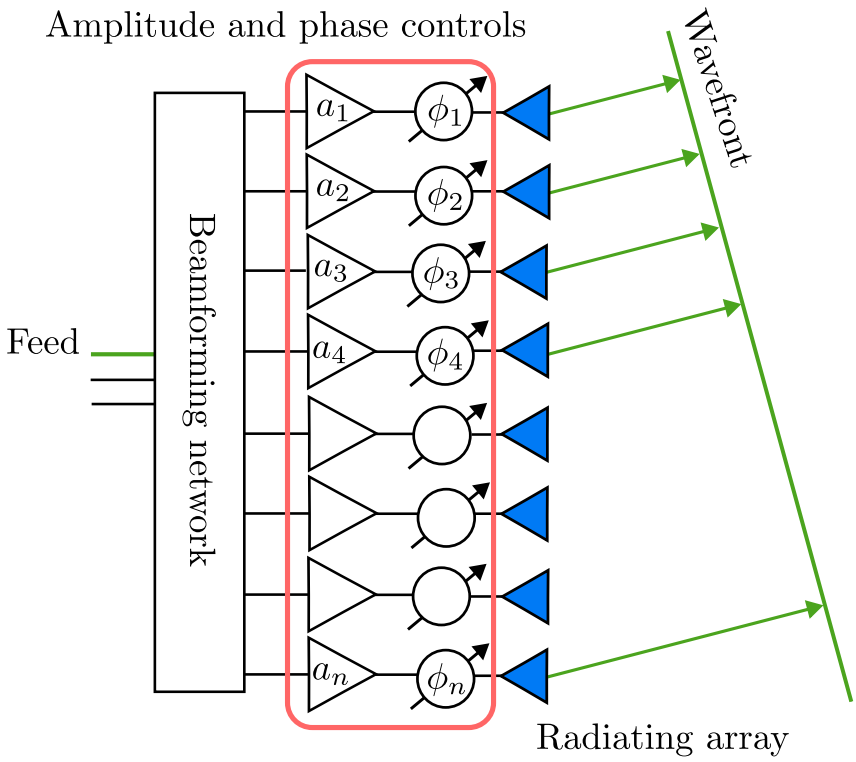

Figure 1.7 – Working principle of a phased array.

In general, phased arrays can be subdivided in two main categories: passive and active. Passive arrays [50] primarily rely on the manipulation of RF signals through passive components, including phase shifters, passive attenuators, and passive BFNs (e.g. Butler, Blass or Nolen matrices [52]) to steer the beam. They offer a less power consuming and lower cost solution employing only passive components. However, this architecture inherently features reduced multibeam flexibility and reconfigurability for the reduced number of controls. Active arrays [53], on the other hand, incorporate active components (e.g. low noise amplifiers for Rx and power amplifiers for Tx and variable phase shifters) to enhance gain and improve system RF performances, including dynamic beam steering and versatile multibeam capabilities, as reported in [54]. They exhibit greater complexity than the passive ones, necessitating higher power consumption due to the strong use of solid-state technologies, digital processing, active BFNs, cooling systems and thermal management.

Some manufactured examples of phased arrays are depicted in Fig 1.8 considering

on-board satellite applications. In Fig. 1.8a, the S-band Tx antenna installed on the Globalstar-1 satellite is showed. While in Fig. 1.8b, Ka- and Ku-band antennas employed in the Starlink constellation are characterized each one by almost one thousand of radiating elements.

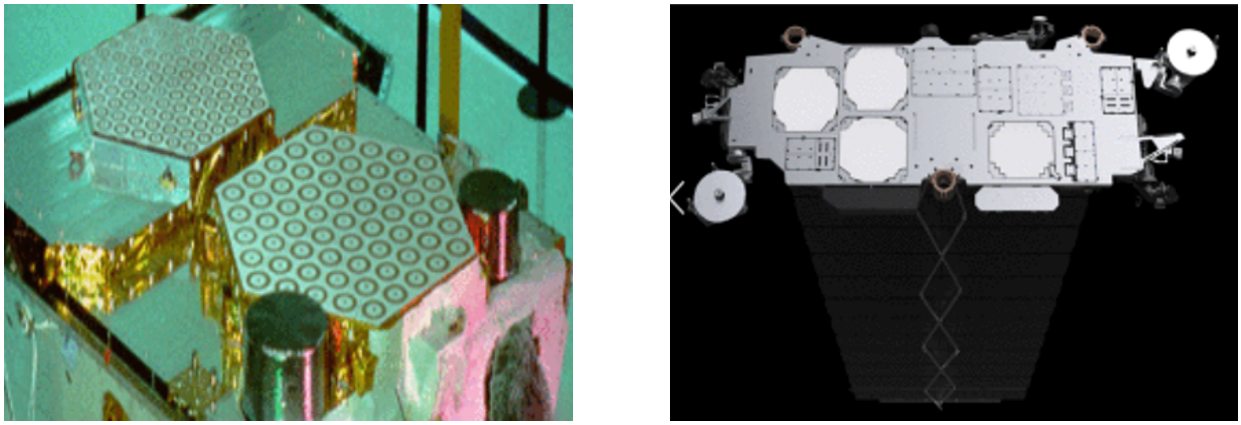

(a) (b)

Figure 1.8 – Configurations of arrays implemented on-board satellites. (a) S-band Tx antenna installed on the Globalstar-1 satellite (cycle of life: 1998–2007). (b) Ka- and employed Ku-band radiating apertures (in white) in the Starlink constellation (launched in 2018) (from [54]).

Some recent developments of phased arrays have been also implemented for ground based applications [5], as displayed in Fig. 1.9. These novel on-ground architectures, permit to substitute gateway reflectors with more compact solutions, such as the one developed by Ball Aerospace and Technologies Corporation in Fig. 1.9a implementing a geodesic dome array, the new concept developed by Thinkom [16] in Fig. 1.9b or the new Starlink user terminal antenna in Fig. 1.9c [17] characterized by a phased array of 1280 identical antennas arranged in a hexagonal lattice.

As previously showed, several technologies of phased arrays can be employed today spanning from printed to full-metal ones, depending on the specific application (both on-board and on-ground) [54]–[56]. The space market is developing AAs for their good performance on scanning and reconfigurability (e.g. Iridium NEXT [57], Globalstar-2 [58] satellites are some examples). Solutions to handle the huge complexity and accommodation of these systems are improved through different architectures employing configurations like: sparse arrays (elements located in irregular grids) [18], [19], [59], clustered arrays (the whole array is partitioned in smaller sub-arrays to reduce the number of active controls) [60]–[62], thinned arrays (some elements within

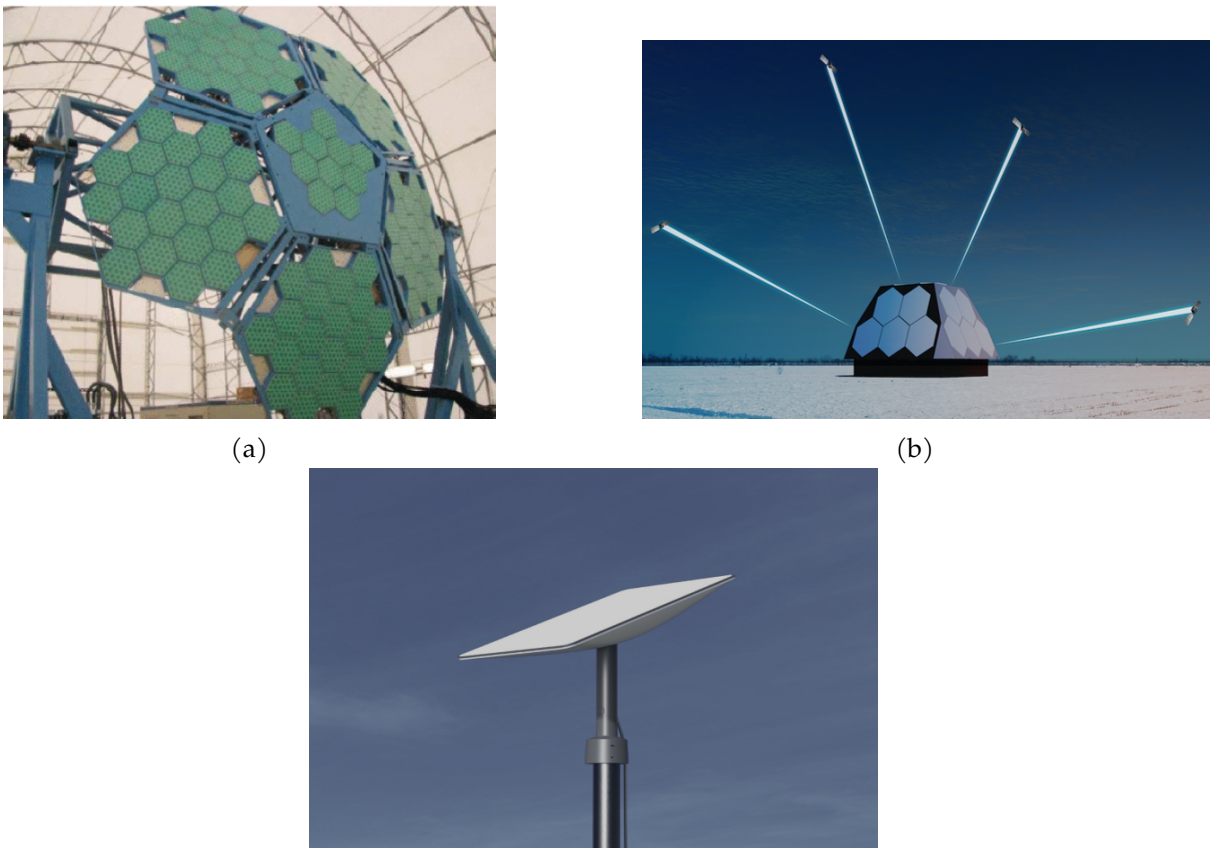

Figure 1.9 – Configuration of phased arrays implemented on-ground. (a) Geodesic Dome Phased Array Antenna built by Ball Aerospace and Technologies Corp (from [54]). (b) New concept of gateway solution for the next generation of satellites developed by Thinkom (from [16]). (c) Starlink's user terminal gateway antenna built in a dish of 1280 elements (from [17]).

the original array are turned off) [63]–[65] or hybrid arrays (combining digital and analog parts) [20]. Technological efforts are also pursued concerning the improvement of GaN amplifiers [66], entire digital building blocks [67] and new fabrication techniques such as full-metal AM to minimize power consumption and losses and maximize the power handling capability [26].

Full-metal phased arrays are gaining attention today. Some examples are based on Vivaldi antennas [68]–[70], ridged-gap waveguide radiators [71]–[73], slot antennas [74], [75], bow-tie cavities [76] or frequency-scaled ultra-wide spectrum element antennas [77], to name a few. Figure 1.10a presents a Vivaldi array in metal within a 8×8 dual polarized flared-notches [70]. An example of ridge-gap waveguide is depicted in Fig. 1.10b, showing the possibility to design radiators using sub-wavelength waveguide

dimensions through more compact systems in order to scan wide angles [73]. Figure 1.10c shows an example of conformal slot array fabricated through full-metal AM [75].

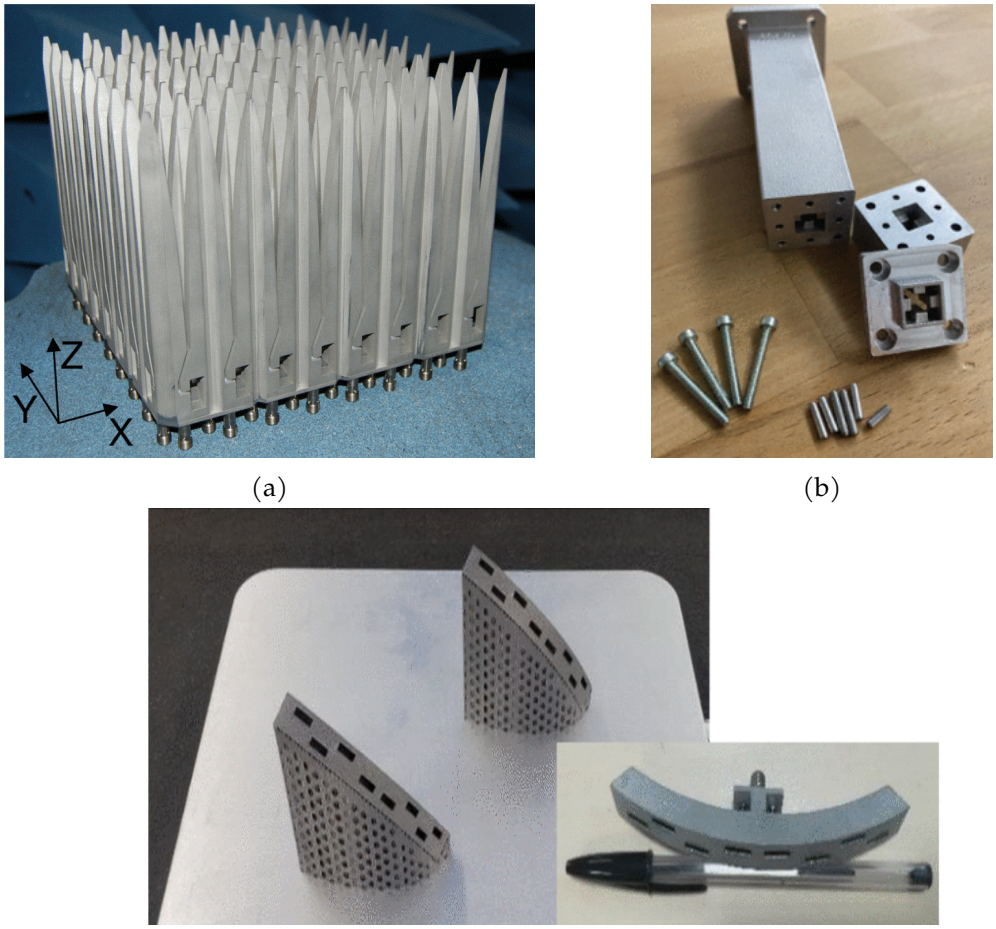

(a) (b)

(c)

Figure 1.10 – Examples of full-metal antenna arrays. (a) Vivaldi elements [70], (b) sub-wavelengths radiators [73], (c) conformal array of slot elements [75].

These solutions effectively address the need for low insertion losses, high power handling related to the avoidance of dielectric components. Their weak points are mainly based on their complexity due to the accommodation of thermal and active controls, digital systems and BFNs through metallic structures. Additionally, they provide wide frequency bandwidths. Dual polarization can be also supported, but at the expense of increasing the complexity on the final design of the system that will consider a double implementation of BFNs.

An alternative configuration to phased arrays are reflectarrays (RAs) [78]. Typically, a RAs permits to steer and shape electromagnetic waves, as displayed in Fig. 1.11.

Specifically, these systems have the capability to adjust the phase of the incoming electromagnetic wave from a generic feed (in green) when interacting with a radiating array (in blue). This phase adjustment allows them to reflect the wave in the desired direction. In particular, the phase can be controlled typically using elements, such as metal patches or dipoles. RAs have been exploited for a long time adopting several geometries. In [79], a detailed review to synthesize the RAs employed for space applications using different technologies is carried out.

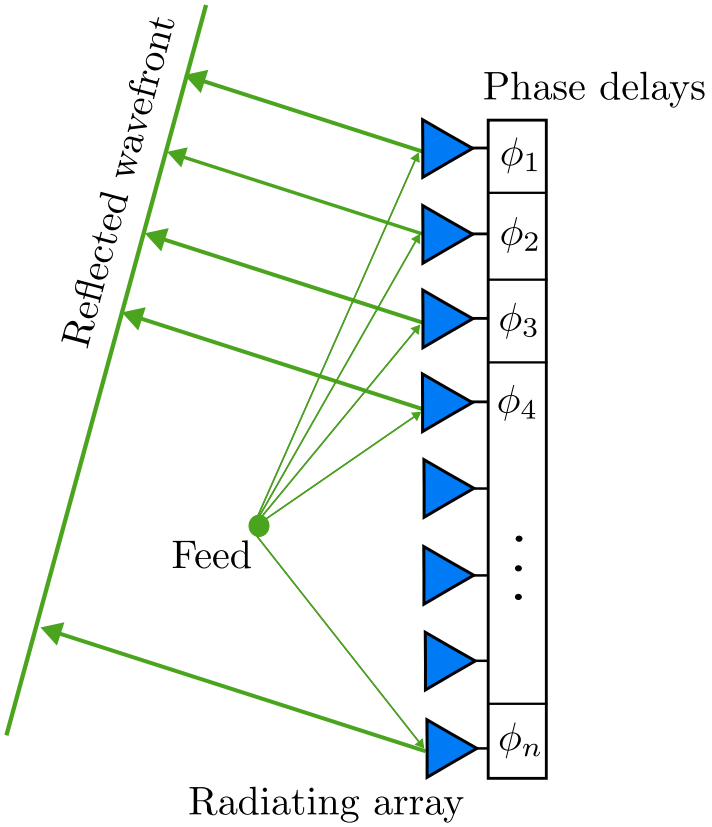

Figure 1.11 – Working principle of a generic RA.

Literature include indeed the designs and implementations of full-metal RAs [80]–[84] employing Phoenix cells [83], square waveguide [81] or metallic reflective posts [84], as showed in Fig. 1.12.
Notably, RAs are characterized by a relatively large physical footprint, including their radiating and feed arrays and necessary supporting structure, like for traditional reflectors. However, their key advantage is their cost-effectiveness, referable to the utilization of planar technology, which does provide some degree of flexibility in terms of integration. This distinct feature sets them apart also from phased arrays, which are intricate

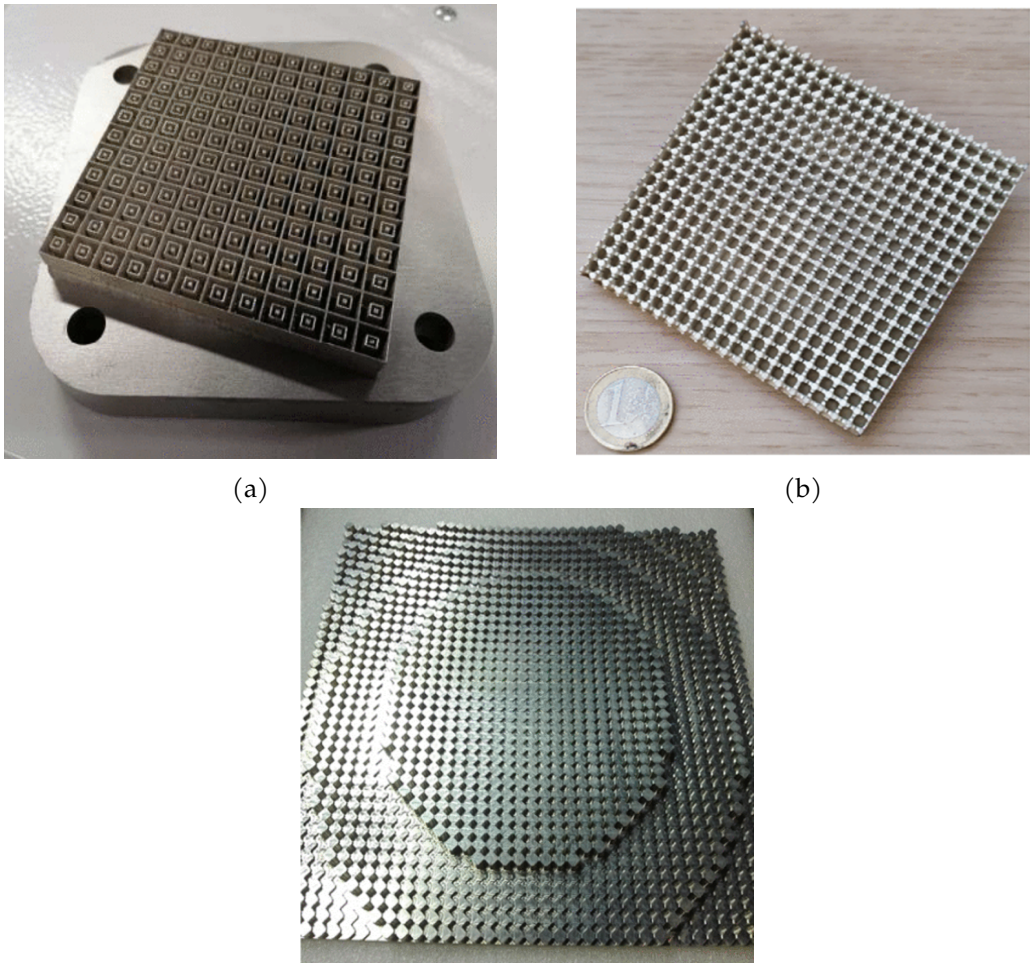

(a) (b)

(c)

Figure 1.12 – Examples of full-metal RAs employing as unit-cells: (a) 3D Phoenix cells (from [83]), (b) ridged-gap waveguides (from [81]), (c) metallic posts (from [84]).

systems demanding the implementation of complex BFNs to reach beam flexibility. On the other hand, they provide moderate frequency bandwidths, mainly because it is challenging to provide linear variation of phase delays across a broad frequency spectrum when employing unit-cells. Dual polarization is also possible for these systems [81]. In addition, to the best of the author's knowledge, no metallic RAs incorporating active controls are present in literature (it only occurs in the case of Printed Circuit Boards (PCB) technology [85], [86]).

On the other hand, transmitarrays (TAs) [87] offer an additional alternative solution that follows the same principle of RAs, this time operating in Tx. TAs (depicted in

Fig. 1.13) operate modifying the phase of the Tx electromagnetic waves from a generic feed source (in green) to each element of a back array (in red). This controlled phase manipulation allows for precise beam shaping and steering from the radiating front array (in blue) in the opposite direction of the feed.

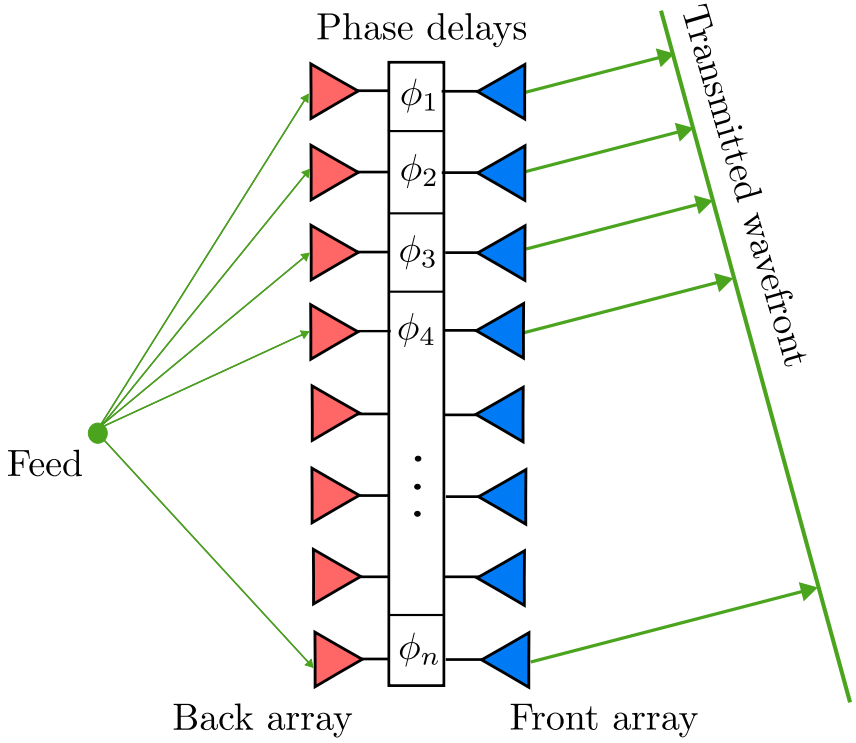

Figure 1.13 – Working principle of a generic TA.

Typically, these configurations consist of multiple unit-cells arranged in planar arrays with regular spatial periodicity. The unit-cells are usually characterized by microstrip patches, or inspired by meta-materials or by frequency selective surfaces, as reported in [87]. Full-metal TAs [88]–[93] are currently discussed in the literature as alternatives to replace dielectric substrates and to guarantee high power handling. These systems are obtained by the stacking of multiple layers of metallic sheets with carefully designed geometries as crossed electric dipole slot in Fig. 1.14a [88], quad-ridged waveguide in Fig. 1.14b [89] or C-shaped slot in Fig. 1.14c [92].

They mostly present some of the same strong and weak points of RAs such as reduced complexity due to their planar technology, but still employing the system accommodation to support the feed array. However, since they are working in Tx, they avoid feed blockage compared to reflectors and RAs. It is also impossible today to find in lit-

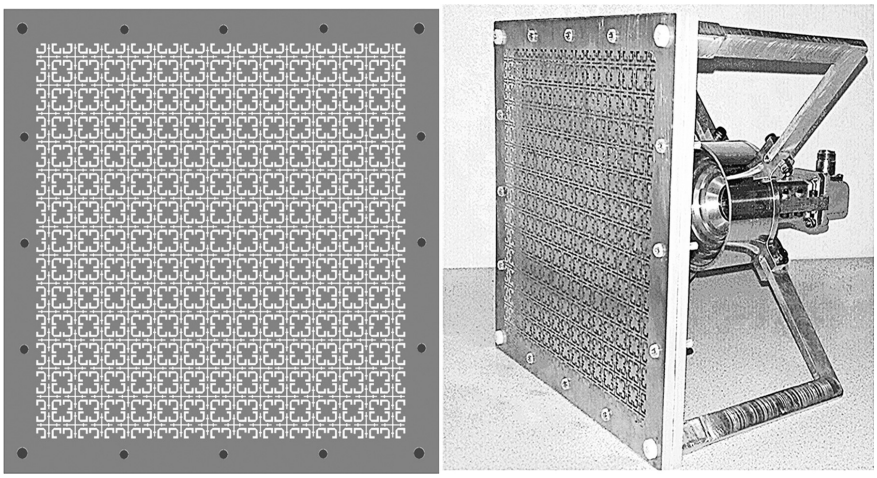

(a)

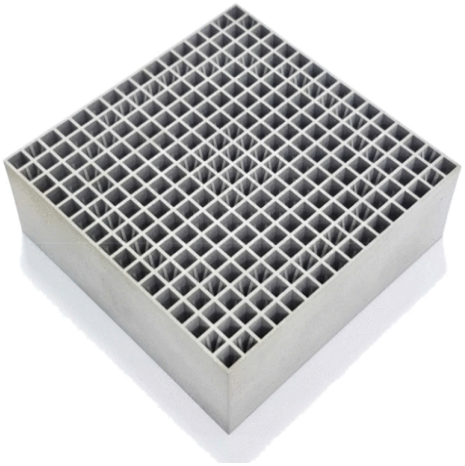

(b)

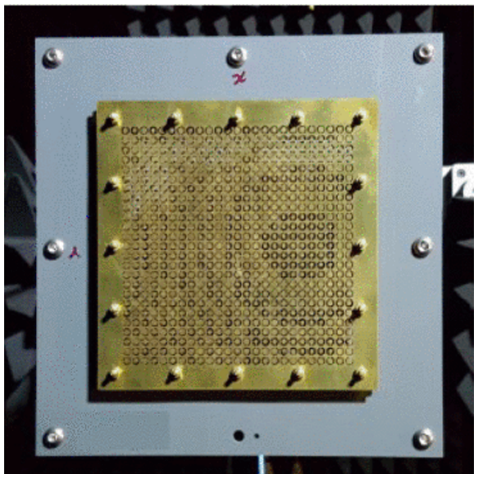

(c)

Figure 1.14 – Examples of full-metal TA employing as unit-cells: (a) crossed-electric dipole slots (from [88]), (b) quad-ridged waveguides (from [89]) and (c) C-shaped slot radiating elements (from [92]).

erature active full-metal TAs, as for RAs. They have the potential to enable dual polarization capabilities by designing the specific unit-cells and they offer a medium-sized bandwidth, comparable to RAs as well. TAs represent a simplified working scheme (usually with flat profiles) of discrete lenses [94], which will be examined in greater detail at the end of the next subsection.

1.1.3 Lens antennas

Microwave lenses offer an alternative solution for high-gain antennas able to provide multibeam coverages. These structures have the capacity to focus RF signals into a single point while traversing a material, following the focusing principles from optics [95]. The conventional dielectric lenses [96] employ a dielectric medium to ensure focalization in accordance with Snell's laws of refraction. In addition, these antennas offer high compactness and ease of manufacturing. However the presence of the dielectric leads to significant losses and cannot handle high power levels. Several examples exist today such as graded-index lenses [97], achieved by gradually modifying the refractive index within the lens (e.g. Gutman [98] or meta-material-based lenses [99]), but they are not considered in this state of the art.

Accordingly, to address the limitations associated with dielectric materials, researchers have implemented full-metal lenses from the 40's, as presented in [100]–[102]. One of the most consolidated type of such lenses is based on Parallel-Plate Waveguide (PPW), as documented in [103]. Instead of using dielectric materials, these lenses employ two metallic conducting plates to create a PPW beamforming cavity for the propagation of electromagnetic signals. In Fig. 1.15, the working principle of a PPW lens is showed.

Through these PPW or two-dimensional (2D) lenses, a cylindrical wave originating from a generic feed (in green) is converted into a planar wave that is emitted into free-space through a continuous radiating aperture (highlighted in blue). The feed is generally placed in a focal point, in order to guarantee zero phase aberrations on the wavefront. The PPW beamformer (displayed in grey) is designed to perform the steering towards a specific direction, when the focal point is defined [103]. Another solution employing the PPW beamformer consists on discretizing the radiating aperture, as showed in Fig. 1.16.

These lenses are also referred in literature as Rotman lenses or 2D discrete lenses [104]. In particular, they adhere to the same beamforming principles as those employed with PPW continuous radiating apertures. However, they introduce a front array (shown in blue) and employ phase delays (indicated by dashed lines) to establish a connection with the PPW beamformer. The focalization proprieties can be described as well by the formulas presented in [103]. The cylindrical waves generated from the feed propagate through the PPW beamformer, passing delay lines and discretized to the front array into a plane transmitted waves towards the desired direction. For both cases in Fig. 1.15 and Fig. 1.16, it is possible to reach scanning towards multiple direc-

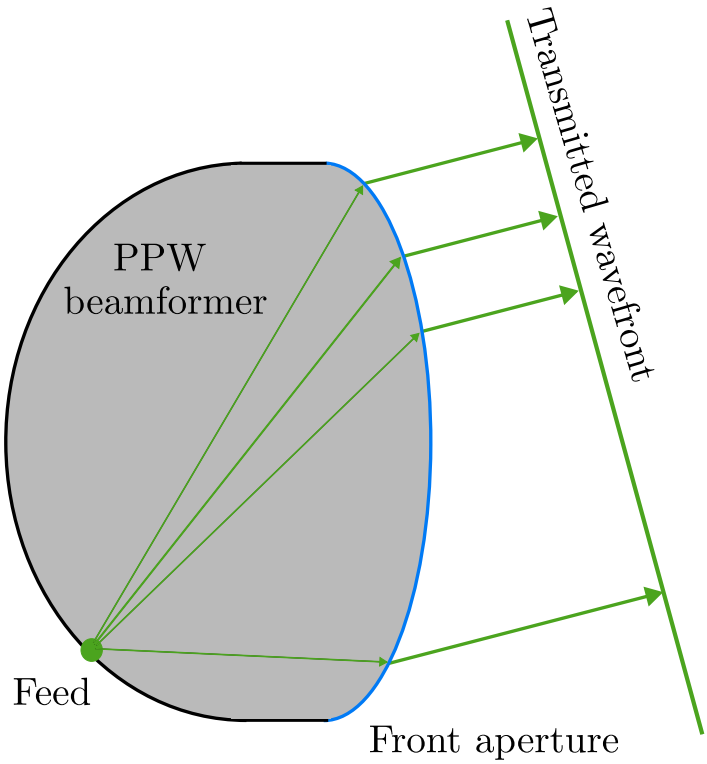

Figure 1.15 – Working principle of generic PPW lenses employing a continuous front radiating aperture.

tions, by employing multiple feeds.

One of the recent advancements on PPW lenses featuring continuous radiating apertures consists on the development of air-filled Luneburg lenses. These systems incorporate metallic posts of varying heights and holes with different depths, to control the phase delays within the PPW beamformer [105]–[107], as depicted in Fig. 1.17a. Additionally, full-metal PPW lenses based on Luneburg principles can be realized using geodesic surfaces [108], which offer highly compact folded designs, as demonstrated in [109] (see Fig. 1.17b), or through water-drop lens configurations [110], [111] (in Fig. 1.17c). One of the most well-known PPW lens employing front arrays is the Rotman lens, as described in [112]. Multiple implementations of the Rotman configuration in metal can be found in literature today [113]–[116], as the example in waveguide technology [114] displayed in Fig. 1.17d.

In general, PPW lenses can enhance their compactness by relying on folded designs, as showed in all the examples in Fig. 1.17. This design approach allows them to achieve minimal scanning losses by enabling the creation of rotationally symmetric conformal

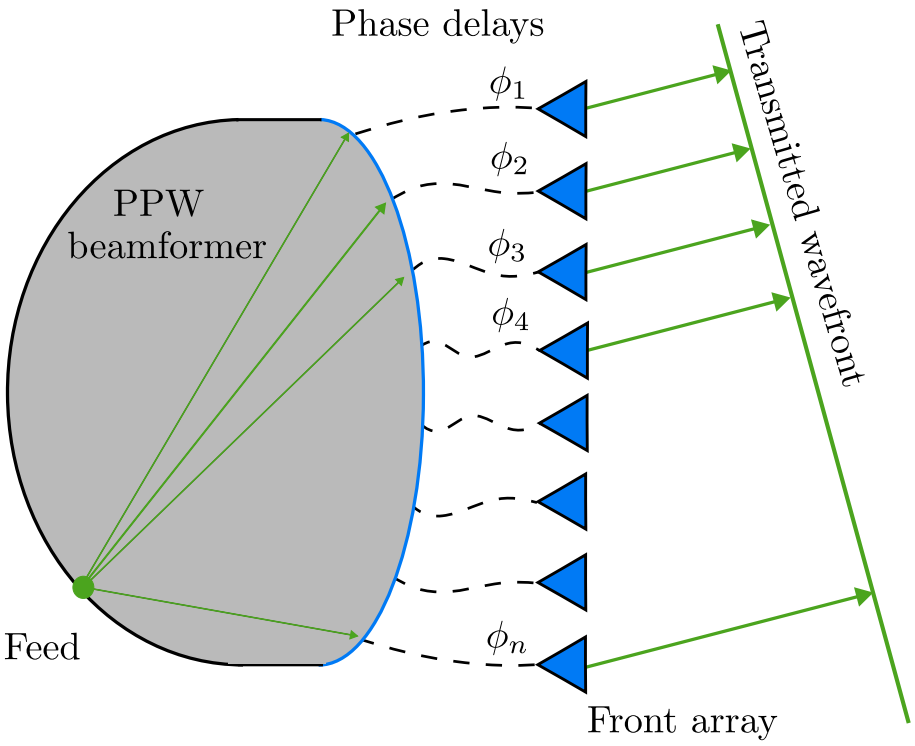

Figure 1.16 – Working principle of generic PPW lenses employing a discrete front array.

structures. The introduction of multiple feeds, as observed in the input ports of Fig. 1.17a, significantly enhances the multibeam scanning versatility of these setups, enabling the generation of a single radiated beam for each feed (SFPB configuration) employing only one aperture. Notably, they present strong scanning capabilities within the plane aligned with the lens but they lack the ability to scan beyond this specific plane. However, for both cases, the reconfigurability of the beam is complex, since they are characterized by a SFPB configuration and they need a switching network to provide an electronic steering. PPW lenses support the propagation of the Transverse Electro-Magnetic (TEM) mode, allowing for the achievement of broad frequency bandwidths. However, they typically handle a single polarization, thus needing to use a polarizer to support dual polarization features [117].

In order to expand the scanning capabilities of the conventional PPW lens solutions in other planes, new developments based on stacking are being explored [118]–[121], as in Fig. 1.18. This approach still presents some limitations of scanning in multiple directions due to manufacturing constraints. In particular, the minimum achievable height of the stacked layers, as illustrated in Fig. 1.18a (where $h = 0.7\lambda$), can impose

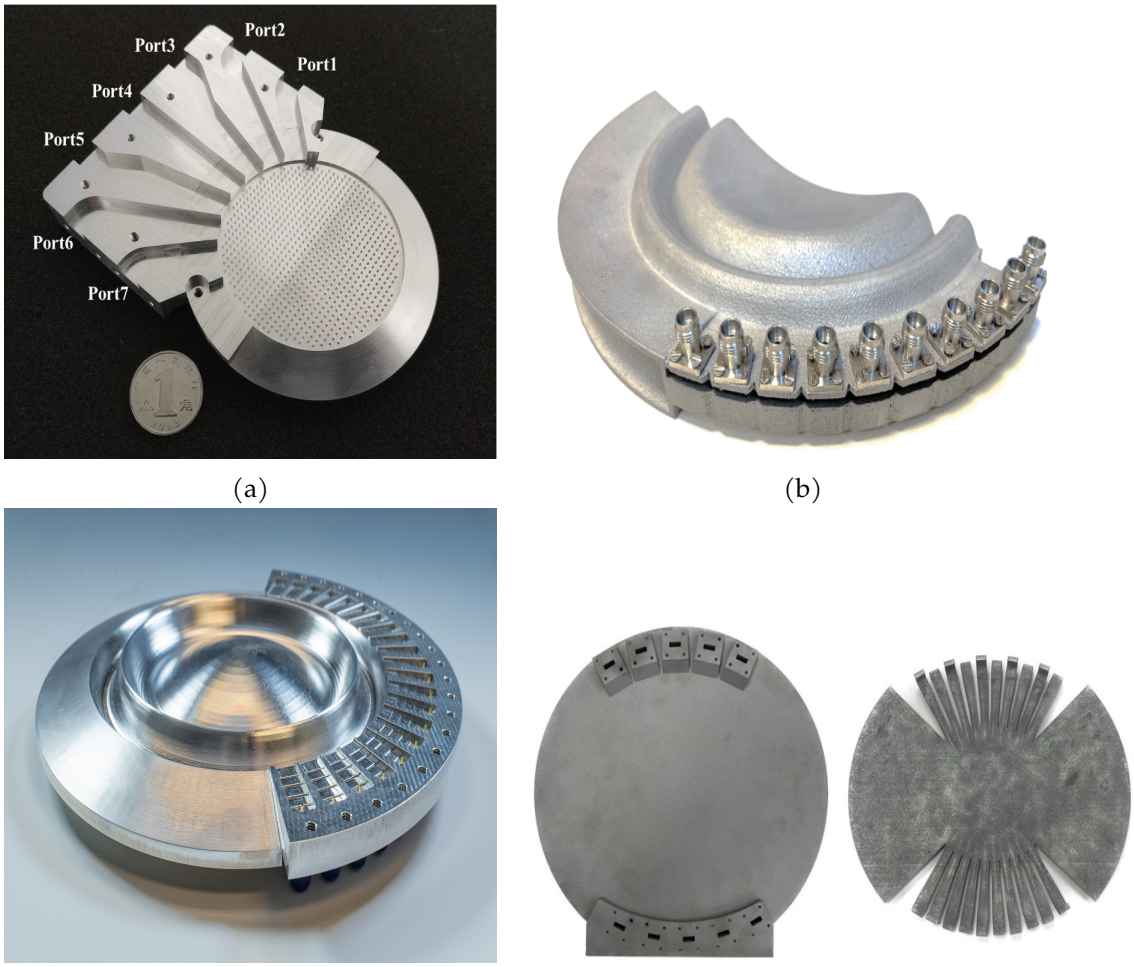

Figure 1.17 – Configuration of full-metal PPW lenses. (a) Air-filled Luneburg lens loaded with metallic posts (from [105]). (b) Geodesic modulated lens (from [109]) (c) Water-drop lens (from [111]). (d) Double-ridged waveguide Rotman lens (from [114]).

limitations on the scanning capabilities within certain planes. This is because the aperture in a given plane is discretized and not conformal, which may constrain the scanning options available. Additionally, these systems necessitate dedicated multiple BFNs to enable and control scanning in multiple directions. Concerning the remaining features, they maintain large frequency bandwidth and offer mainly single polarization capabilities, similar to the solution that has been already presented. It is obvious that stacked PPW lenses are more bulky that the single layer PPW lenses.

On the other side, 3D discrete lenses [122]–[124] represent today another solution to reach high-gain multibeam antennas for space applications. A generic discrete lens

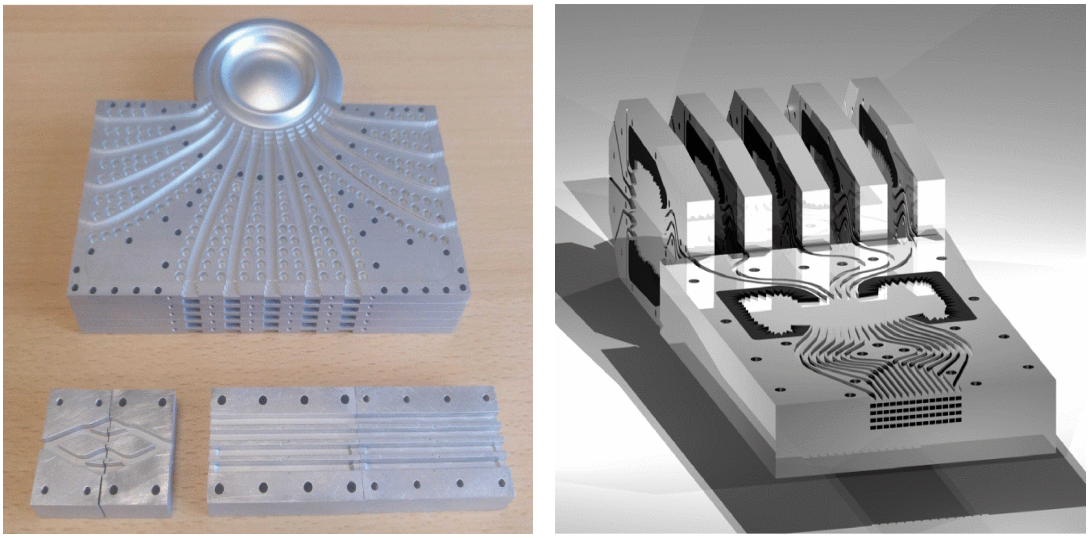

(a) (b)

Figure 1.18 – Configuration of stacked lens employing full-metal PPW lenses. (a) Four stacked modulated geodesic lenses, equi-spaced by an height of $h = 0.7\lambda$ at 60 GHz. Each of the geodesic lens has 13 feed waveguides as input port (from [118]). (b) Graphic view of a stacked lens made of five Rotman lenses (from [121]).

is depicted in one cut plane in Fig. 1.19 to show its working principle. These lenses are constrained to follow the delay lines paths. They do not necessarily respect the Snell's laws [95] because the designer can enforce specific delay lines: for this reason they are also called constrained lenses. The designer can constrain the lens to reach some requirements. Discrete lenses achieve discrete collimation and focusing by employing both back and front arrays, interconnected through delay lines. It is important to note that, they follow the same fundamental principles of TAs, as discussed in [94]. In fact, the incident wave originated from the feed (indicated by the green dot), first traverses the back array (highlighted in red). Subsequently, it follows multiple delay line paths (depicted as dashed lines) before being emitted by the front array (in blue) into free-space in the desired direction. To ensure minimal phase aberrations, the feed is strategically placed at a precise focal point. In Fig. 1.20 several examples of 3D discrete lens realized entirely in metal are shown.

These lenses are constructed using active discrete elements and they are designed to operate across various frequency bandwidths, being employed for multibeam coverage applications. Compared to PPW lenses, they offer improved scanning capabilities through multiple planes, while they are still limited in electronic reconfiguration

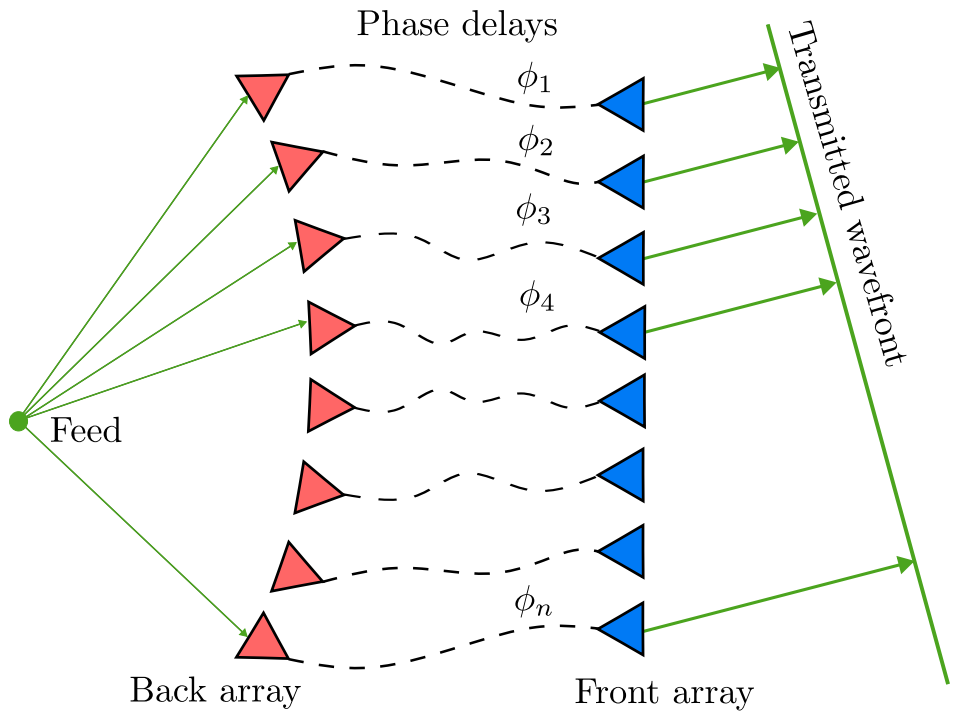

Figure 1.19 – Working principle of a generic discrete lens in one plane.

for their SFPB configuration. Notably, they have advantages over reflector solutions as they employ a single aperture instead of multiple ones and also they do not necessitate the incorporation of complex BFNs. This is because the formation of the main beam occurs in free-space, extending from the feed to the back array. Additionally, these lenses are able to achieve dual polarization features and large frequency bandwidth, as demonstrated in Fig. 1.20c [127]. This is made feasible by designing dedicated radiating antennas and corresponding delay lines (e.g. waveguides, coaxial cables solutions) to support them. As in phased arrays and PPW lenses with discrete arrays, these systems allow for the precise implementation of active controls within the front arrays, significantly enhancing the illumination of the system. However, it is important to emphasize that they have a tendency to be bulky and complex. This complexity arises from the need to accommodate several radiative components, including multiple feeds, the amplification blocks and thermal management systems.

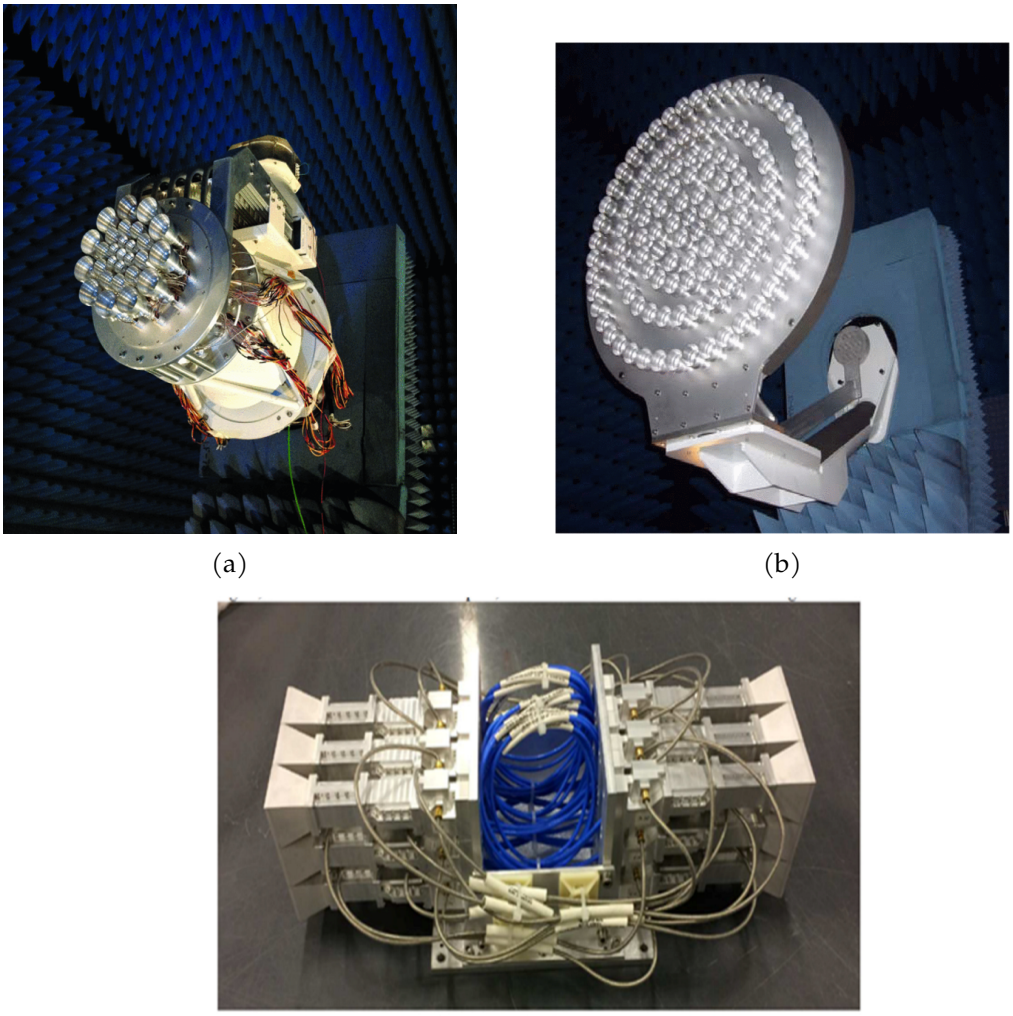

Figure 1.20 – Configuration of full-metal 3D active discrete lenses. (a) Tx active aperiodic lens including active and thermal controls working in Ka-band realized by Space Engineering/European Space Agency (from [125]). (b) Tx discrete lens working in Ka-band and constituted by 112 radiating elements (from [126]). (c) Tx/Rx active discrete lens working in Ku-band to be employed in a reflector system for multibeam coverage (from [127]).

1.1.4 Configurations comparison

This subsection reports a brief comparison of the presented solutions to face the high power handling and multibeam flexibility. A comparison between reflectors, phased arrays, RAs, TAs, stacked PPW lenses in both continuous and discrete radiating aperture configurations, along with 3D discrete lenses realized entirely in metal is hence carried out. The main characteristics can be summarized as follows:

- **Beam scanning capabilities:** This refers to the ability of the antenna to steer beams in multiple directions simultaneously in order to cover wide scanning angles. Phased arrays and 3D discrete lenses offer high multibeam flexibility enabled by respectively BFNs or multiple feeds to scan across various directions up to wide angles. Stacked PPW or 2D discrete lenses can still achieve high flexibility in multiple directions with some limitations. These limitations are associated to the manufacturing constraints of the stacked profiles, resulting with restricted features in those directions. RAs and TAs can have medium scanning capabilities when employing dual apertures. Reflectors represent the more limited solution in terms of scanning capabilities to reach wide angles, but this feature can be certainly improved with the system feeding the aperture.
- **Active controls:** The ease of integrating active controls varies across the presented antenna solutions. Phased arrays and discrete lenses allow for straightforward integration because their radiating front arrays are discrete. In contrast, reflectors and PPW (continuous) lens systems maintain a continuous radiating aperture, making impossible to apply amplification layers close to them for enhanced illumination efficiency. Notably, active RAs and TAs are not currently documented in the literature concerning full-metal solutions.
- **Beam repointing capabilities:** In general, multibeam antennas based on passive solutions (including reflectors, RAs or TAs or discrete lenses), are not able to electronically repoint the beams towards different directions since are characterized by a SFPB configuration. Active discrete lenses have similar limitations as compared to passive discrete lenses in terms of repointing flexibility for their SFPB configurations. While active phased arrays are the most performant in terms of repointing capabilities.
- **Dual polarization:** Reflectors (depending on the feed), 3D discrete lenses (implementing dual channel delay lines), RAs and TAs (depending on unit-cell geometry) are the primary solutions supporting dual polarization. Phased arrays can support dual polarization features, but at the expenses of the implementation of bulky BFNs, one for each polarization. On the other side, stacked PPW lenses, being characterized by parallel conducting plates, mostly do not support dual polarization features.
- **Frequency bandwidth:** Broad frequency bandwidth can be reached by a reflectors (employing ultra wide bandwidth feeds) and PPW lenses that use the prop-

agation of the TEM mode through parallel metallic plates. Discrete lenses can also support large bandwidth by employing technologies like (ridged) waveguides and coaxial cables to create true-time delay lines. Phased arrays bandwidths, depend on the performances of the implemented radiating elements and their BFNs and they can reach medium frequency bandwidth. Then, RAs and TAs offer intermediate frequency bandwidth features, contingent on the unit-cell geometry.

- **Cost and complexity:** Reflector antennas are relatively easy to manufacture, thanks to their basic metallic dish as the main radiating aperture. In contrast, RAs and TAs offer solutions with moderate levels of cost and complexity, mainly characterized by their planar arrays and the incorporation of delay lines for achieving the necessary phase delays to enable precise beam steering. On the opposite side, phased arrays are known for their huge cost and complexity. This is due to their complex BFNs and the additional considerations related to thermal management and cooling systems, which significantly contribute to their overall complexity and expense. Lens solutions are also characterized by high complex designs concerning their full-metal structures. On one hand, this complexity is associated with the huge assembly on stacked 2D PPW lenses, and on the other, it is due to the voluminous geometries of 3D discrete lenses to reach high flexibility.
- **Volume and accommodation:** Reflector-based systems are typically characterized by their bulkiness and the substantial volume they occupy, primarily due to the need to accommodate the feed system, the associated supporting structures and the multiple apertures. Phased arrays, stacked PPW and discrete lenses require a considerable volume due to the numerous metallic components they must incorporate. Phased arrays and stacked PPW lenses present complex and bulky multiple BFNs to achieve multibeam scanning flexibility. 3D discrete lenses utilize a common BFN but remain bulky due to the need to accommodate metallic arrays, delay lines between them and the feed elements. On the other hand, RAs and TAs offer more space-efficient solutions by employing planar metallic arrays as apertures, resulting in a slightly compact footprint compared to reflectors.

In summary, this subsection has involved a comparison of various full-metal multibeam high-gain antenna solutions, considering attributes such as beam scanning and

repointing capabilities, the ability to integrate active controls, support for dual polarization, frequency bandwidth, cost and system complexity, and volume accommodation. The selection of the appropriate antenna type is mainly based on the specific application case and the trade-offs associated with these features.

Through this comparative analysis of full-metal radiators designed for space applications, it becomes evident that 3D discrete lenses offer a promising solution to be investigated. These systems represent an innovative solution to achieve high-gain capabilities and robust power handling using metallic structures. Their key features lies in their ability of multibeam scanning in a flexible way by employing multiple feeds. However, as previously mentioned, they are bulky structures incorporating multiple metal radiating components. The complexity of accommodating these structures in more compact ones is examined in the following section. Specifically, a focus on optimizing the manufacturing processes to reduce both volume and weight is presented.

1.2 Metallic 3D printing for radio-frequency components and antennas

Today AM, often referred as 3D printing [23]–[25], represents a groundbreaking technology that has reshaped the landscape of design, prototyping innovative products, exploring a variety of situations and contexts. Unlike Traditional (subtractive) Manufacturing (TM) approaches [31]–[33] that involve cutting or shaping materials to create objects (e.g. laser cutting, milling, or electro-erosion), AM constructs 3D objects layer by layer, based on digital designs. This innovative AM approach is able to achieve unprecedented levels of flexibility and precision, allowing the design of complex and intricate shapes compared to the traditional one, which is well-suited for the fabrication of simpler shapes, as shown in Fig. 1.21. More exotic meanderings can be realized through AM technology, reaching high level of miniaturization compared to the traditional ones.

TM, being a more established technology, offers a cost-effective solution for large-scale production compared to AM, which tends to be less expensive for smaller batches. Additionally, TM provides a wider range of material options compared to AM. The main limitations of the AM are related on its novelty, but it is gradually gaining strength over the years. The production time, also known as lead time of AM can be shorter than

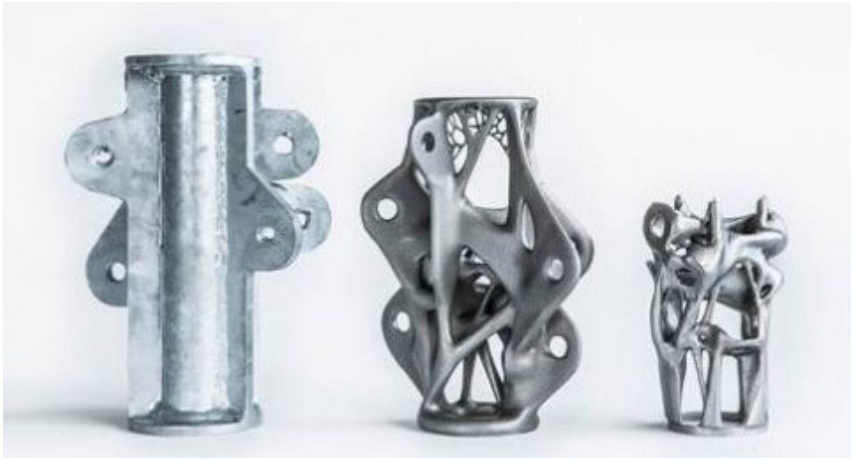

Figure 1.21 – Topology optimization achieved through AM. On the left, TM piece, while moving on the right, more complex products, increasing miniaturization through AM (from [25]).

TM. Despite the need for more post-processing steps in AM, it still offers quicker production compared to traditional one. In fact, a component can be designed, uploaded, and printed within an hour, depending on its complexity. Furthermore, AM presents itself as a more sustainable solution since it utilizes less material and generates less waste. It introduces the possibility of recycling materials during fabrication. For instance, the remaining material can be directly reused for a new fabrication, starting from powder rather than a solid block of material as in TM. Table 1.1 summarizes the comparison between TM and AM technologies, highlighting the key features discussed above.

	AM	**TM**
Process	Layer by layer	Removing material
Design	Complex geometries	Simple geometries
Cost	More expensive for large runs cost-effective for small batches	Cost-effective for large scale production
Materials	Limited in materials	Wide range of materials
Time	Faster production	Longer production
Waste	More sustainable	More waste

Table 1.1 – Comparative analysis between TM and AM.

In the past decade, huge advances in 3D printing have particularly influenced the space applications sector, as reported in [128], [129]. The development of AM technologies has impacted indeed the prototyping of fast, cost-effective and monolithic RF devices, as reported in [130]–[132]. Today, a variety of methods and materials can be

employed within AM processes to fabricate objects. As an example, plastic polymers can be implemented using technologies such as SLA [27], [28] or Fused Deposition Modeling (FDM) [133], followed by a successive metal plating of the fabricated piece. On the other hand, metal alloys such as aluminum (AlSi10Mg), titanium or stainless steel are also employed as 3D printing techniques using directly metal materials. The technologies that facilitate the direct 3D printing implementing these metal alloys include SLM [29] and DMLS [30].

In this thesis, the primary emphasis is focused on the use of full-metal 3D printing. More specifically, the research focuses on only manufacturing techniques utilizing the SLM method [29]. This choice is connected to the collaboration established within the framework of this thesis with SWISSto12, an industrial partner based in Switzerland. SWISSto12 has both developed and patented this particular fabrication process, as referenced in [134], [135]. Figure 1.22 showcases some of products fabricated through SLM techniques from SWISSto12, highlighting their innovative and compact solutions for fabricating filters, cluster of feeds, antenna arrays and curved waveguide solutions.

The main benefits achieved through full-metal AM are listed as following:

- **Excellent RF performances**: This technology allows for the fabrication of components with outstanding RF performances. These components exhibit low losses and consume minimal power, as they are constructed employing only metal. This eliminates the need for dielectric materials that can introduce losses.
- **Compatibility with high power handlings**: Full-metal 3D printing enables the design of high power systems. This is particularly advantageous for applications that require the handling of significant power levels such as in space scenarios.
- **High design flexibility**: The presented technology offers exceptional design flexibility. It can produce complex parts with intricate curvatures and geometries. Layer-by-layer printing ensures higher precision and accuracy in creating these intricate designs.
- **Lightweight and mass saving**: It is possible to fabricate monolithic systems in a single piece. This eliminates the need for assembling multiple components, which can introduce losses at the interfaces. As a result, it reduces weight and saves material compared to TM.
- **Reduced lead time and cost competitiveness**: Compared to other techniques, full-metal AM offer highly cost-competitive solutions. Reduced lead time can be achieved compared to TM, despite the various steps involved, such as design,

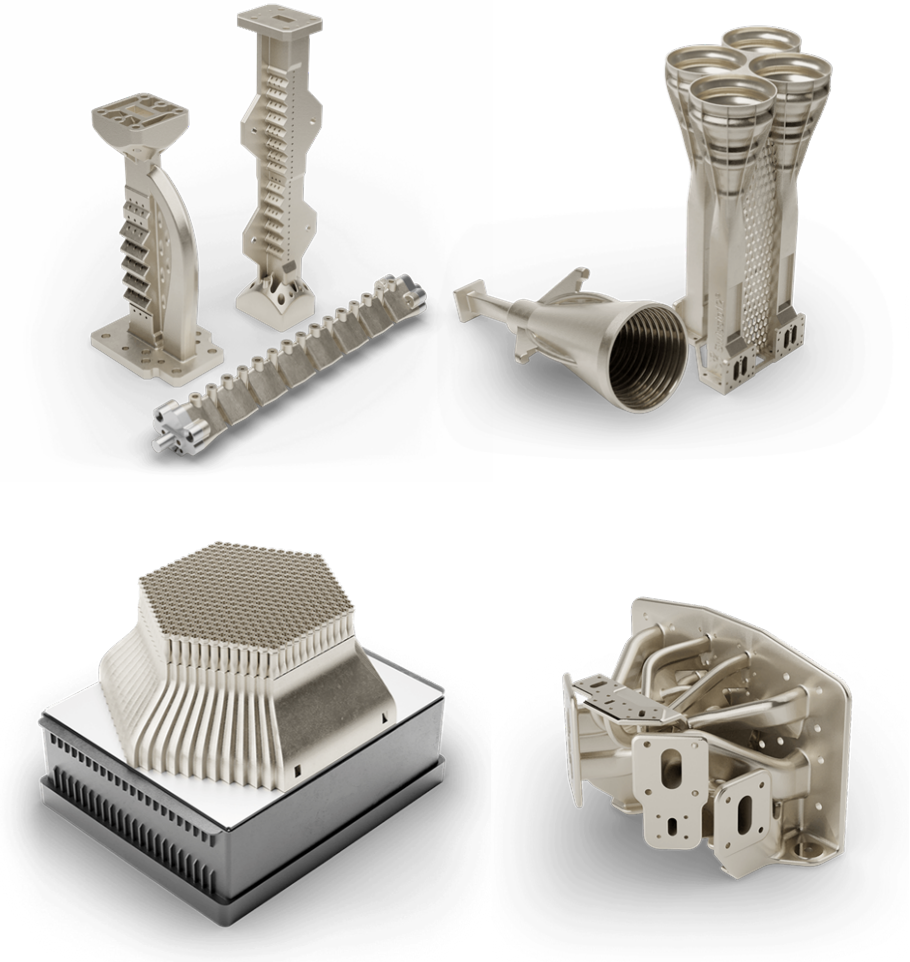

Figure 1.22 – Full-metal AM solutions developed by the industrial partner SWISSto12 using SLM techniques. Waveguide filter and diplexer (top left), monolithic cluster of antennas (top right), complex waveguide cluster (bottom left) and electronically steered antenna array (bottom right) for space-borne payloads (from SWISSto12 website).

manufacturing, machinery setup and the execution of production cycles.

These advantages make full-metal 3D printing a captivating choice for applications in which RF performance, power handling, design complexity, weight reduction and cost-efficiency are crucial considerations. The evolving scenario of these technologies presents today innovative opportunities and ongoing challenges for the New Space industry market. One notable challenge lies in the relatively recent emergence of this technology, which has led to certain limitations. For instance, the surface roughness of raw 3D printed metal components requires additional steps for refinement. Techniques like chemical polishing and metal plating methods become crucial for achieving the de-

sired levels of surface quality and conductivity [136]. Moreover, advancements in post-processing, including automatization of the fabrication, are being explored to enhance the manufacturing process. As this technology continues to evolve at a rapid speed, it is anticipated that future research efforts will observe substantial breakthroughs and innovations. These developments are expected to contribute to the continued maturation of the technology, enhancing its versatility and reliability across a broad spectrum of applications.

The use of full-metal AM technology to manufacture complex antenna systems can provide substantial advantages. For this reason, the development of 3D discrete lenses is entrust to the domain of metallic 3D printing, with the objective of reducing system complexity and enhancing performances for the development in a high power handling scenario. As a matter of fact, in the next section, the main features of 3D discrete lenses designed in waveguide technologies through AM are showed.

1.3 3D discrete lenses in waveguide technology

In the scientific literature, discrete lens antennas are alternatively known as bootlace or constrained lenses [22]. This nomenclature comes from the focalization of incoming waves in a constrained manner [95]. 3D discrete lens systems consist on one or multiple feeds positioned in the focal points, two radiating front and back arrays and delay lines to connect the profiles, as already displayed in Fig. 1.19. In particular, the determination of the number of focal points involves solving Geometrical Optics (GO) equations for focalization, which necessitates considerations regarding certain variables of the lens. A detailed explanation of these considerations is provided in the upcoming sections.

In general, 3D discrete lenses present the potential to facilitate scanning in all directions more effectively when compared to the previously presented solutions involving stacked 2D lenses. In literature, 3D discrete lenses are less considered compared to the 2D counterparts. Some seminal contributions are reported in the following as starting points. In [123] McGrath has introduced a 3D discrete lens presenting flat front and back arrays and two focal points located in the lens axis, with the homologous element radially aligned. Then, Sole and Smith [137] introduced an example of 3D discrete lens exhibiting flat front and back arrays with the shape of a saddle and four focal points. In [124] J.B.L. Rao investigated 3D discrete lenses having two, three, and four focal points located in a single plane containing the longitudinal axis of the lens. J.L. MacFarland

and J.S Ajoika [138] showed a solution based on bi-spherical lenses composed by a combination of half-spheres having two identical radii; while J.B.L. Rao [139] modified these lenses radii in a more generic way. In addition over the last 20 years, several developments on 3D discrete lenses have been improved including some industrial products [22], [122], [126]. Today the choice of the arrays shape and the number of focal points is primarily determined by the specific application and scenario. This includes considerations such as balancing accommodation and scanning capabilities across a wide FoV, among other factors.

In the next section, an overview on the properties of 3D discrete lenses is presented concerning their geometry analyzed into details as well as an examination of their primary strengths and weaknesses. Subsequently, the relation between degrees of freedom and number of focal points is introduced. Following this, a section dedicated to the magnification or zooming factor applied to 3D discrete lenses, defining several potential application scenarios corresponding to different values of this factor. Finally, the section concludes with the radiation pattern computation in order to reach multibeam scanning flexibility.

1.3.1 General features

A generic sketch of a 3D discrete lens is displayed in Fig. 1.23 to generate beams pointing in multiple directions such as: in broadside (beam $\#1$), in the horizontal plane (beam $\#2$) and in a generic oblique plane (beam $\#3$). In general, these focusing systems (already discussed in [22]) are mainly characterized by the cascade of multiple elements as described in the following:

- a front radiating array of diameter D_A (in blue) to perform the steering in the desired directions $(\theta_{out,k}, \phi_{out,k})$;
- a block of delay lines to connect the back and front arrays (dashed black lines within the grey box);
- a back array of diameter D_B (in red) illuminated by the selected feed from an angle $(\theta_{in,k}, \phi_{in,k})$;
- a feed array containing the feeds F_k placed in the focal points.

Essentially through these systems, as already discussed, the incident wave does not necessarily follow Snell's law when it passes through the lens arrays. Instead, it is constrained to follow the delay lines, as defined by the connected points through dashed black lines in Fig. 1.23.

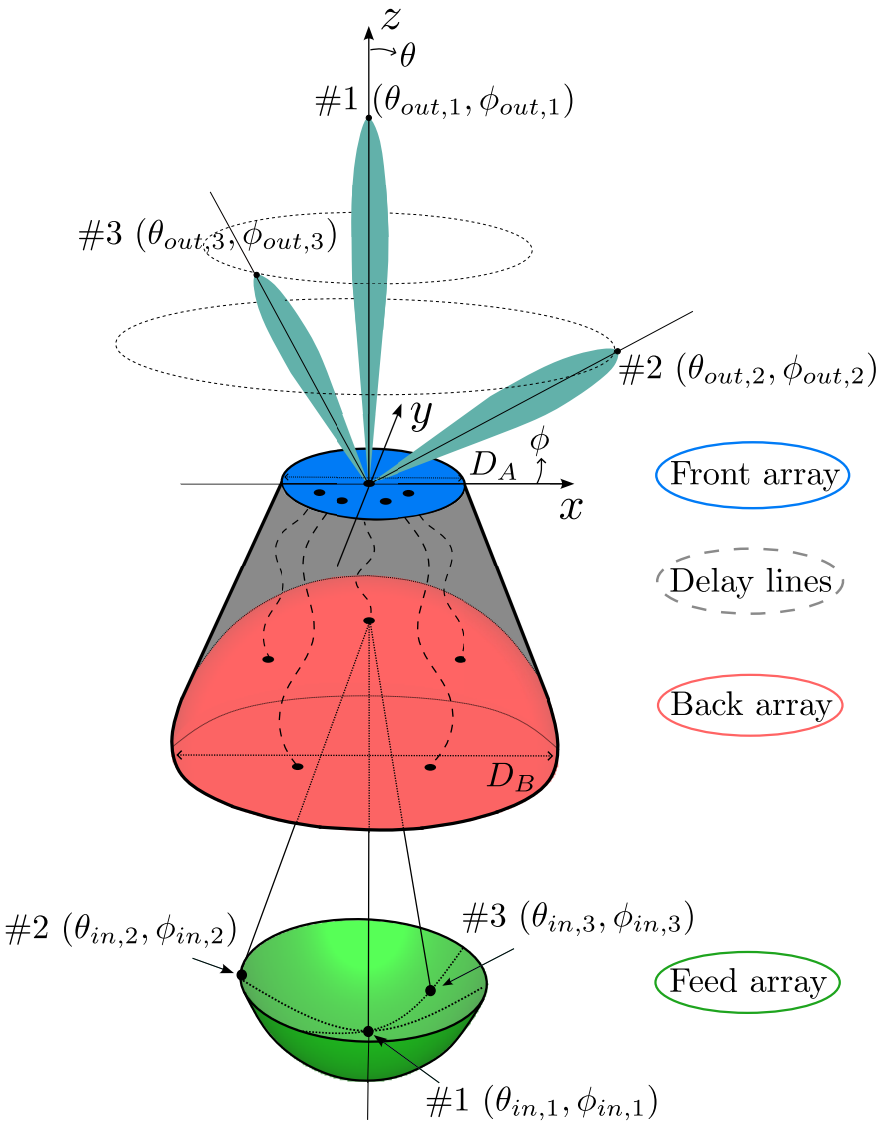

Figure 1.23 – Conceptual view of a 3D discrete lens, including a front array (in blue), back array (in red), block of delay lines (in grey) and feed array (in green). Three possible beams are visualized: beam #1 in broadside, beam #2 in ($\theta_{in,2} > 0°$,$\phi_{in,2} = 0°$) and beam #3 in a generic direction ($\theta_{in,3} > 0°$,$\phi_{in,3} > 0°$).

Various technologies can be employed to create such delay lines, including coaxial cables [126], metallic waveguides [140], and microstrip lines [123]. However, since one of the objective of this thesis is to propose a full-metal solution, the delay lines realized by waveguides are considered with a deeper focus on their design in Chapter 2. This choice is motivated by their capacity to exhibit low signal losses and effectively handle

high power levels, making them a pertinent choice for the thesis investigation.

Moreover, when the lens is fed in a focal point, it theoretically achieves perfect focalization of the energy without any phase aberrations, similar to what occurs in optics [95]. The number of these focal points is determined by the specific geometry of the employed 3D discrete lenses and the constraints applied to the variables defining their front and back arrays. This relationship will be explored in detail in the upcoming sections. In general, 3D discrete lenses are characterized by the following notable strengths:

1. **High 2D scanning capabilities:** These antennas present high flexibility in steering the beam among multiple directions due to their 3D geometry. This is in opposition with the scanning constraints observed in 2D lenses [104]. In addition, they exhibit minimal scanning losses thanks to their multiple feeds and the arbitrary front and back arrays configurations.
2. **Multibeam coverage:** These systems allow for the creation of multiple beams using a SFPB configuration employing one single aperture. Essentially, by feeding each feed, the corresponding beams are emitted in the far field from the front array. Additionally, active controls can be implemented to achieve continuous spot coverage, enhancing illumination efficiency of the profiles and mitigating crossover levels and spillover losses.
3. **True-time delay solution:** The implementation of delay lines, realized in this thesis through waveguides between the front and back arrays, significantly enhances broadband operations, especially when employing bandwidth-enhancing features like dual-ridged solutions.
4. **Quasi free-space beamforming solution:** The process of beam formation primarily occurs in the free-space. In fact, in the initial phase, the electromagnetic fields propagate in air, specifically from the feed to the back array. Subsequently, in the second phase, the back and front arrays are connected together using low losses delay lines.
5. **Dual polarization features:** Using dual channel waveguides, these radiating systems support dual polarization features, functionality not yet applicable for 2D lenses. Additionally, dual polarized radiating elements can be integrated quite easily including in their design septum polarizers to separate the two polarizations.

6. **Complexity scaling with number of beams:** The complexity of these systems slightly increases with the number of elements and beams. In fact, to increase the scanning capabilities (e.g. additional fixed beams in the SFPB optics), one simply needs to augment the corresponding feeds within the feed array, rather than having to expand the associated BFNs, as is typically required for phased arrays.

On the other hand, the main limitations consist mainly on their high volume and weight which pose challenges in terms of accommodation. These 3D discrete lens implemented employing only metal should also accommodate active controls, thermal and cooling blocks [126]. An approach for simplifying the full-metal system complexity, as outlined in this thesis, consists on employing AM technologies to fabricate the entire radiative system. This approach facilitates the integration of multiple components into a single monolithic piece and creating a cost-effective system capable of handling high power levels while facilitating manufacturing constraints. Experimental validation are presented in the next chapters.

1.3.2 Variables definition

Figure 1.24 shows a generic representation of a 3D discrete lens in all its building blocks and variables. The depicted lens presents a rotational symmetry and its geometry is the same for all the azimuth planes. However, this formulation can be applied for both rotationally and not rotationally symmetric lenses. In the case of not rotational symmetry, each plane of the lens possesses its own distinct architecture.

The i-th back array antenna B_i is defined by its Cartesian coordinates $\overrightarrow{O'B_i} = [X_{B_i}, Y_{B_i}, Z_{B_i}]$. While, the i-th front array antenna A_i is described by its front coordinates $\overrightarrow{OA_i} = [X_{A_i}, Y_{A_i}, Z_{A_i}]$. The total number of element for each array is identified as N_{tot}. To note that the relation between the two coordinate systems is just a translation in the z-axis as following $|\overrightarrow{O'O}| = \Delta_z$ The focal distance measured between the generic focal point and the center of the back array is defined by the variable F. The k-th focal point is denoted by $\overrightarrow{O'F_k}$ respect to the center of the back array coordinates. Their corresponding positions are determined by the azimuth and elevation input angles as follows:

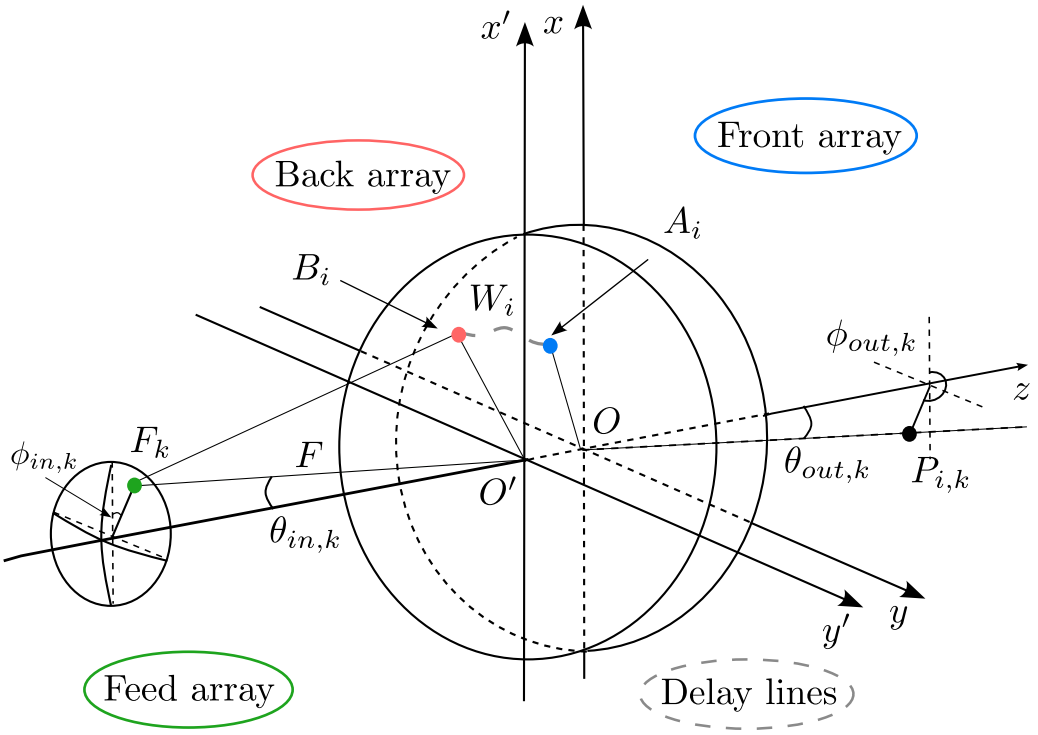

Figure 1.24 – Sketch of a 3D discrete lens with flat front and back arrays in all its variables.

$$\overrightarrow{O'F}_k = \begin{cases} F_{x_k} = F\sin(\theta_{in,k})\cos(\phi_{in,k}) \\ F_{y_k} = F\sin(\theta_{in,k})\sin(\phi_{in,k}) \\ F_{z_k} = -F\cos(\theta_{in,k}) \end{cases} \tag{1.1}$$

The feed array in Fig. 1.24 can be defined as the grouping of feeds containing the focal points, that guarantees minimum phase aberrations for the highest number of points of the lens [122]. The shape of the depicted feed array serves as a general representation. In many contributions in literature, spherical, elliptical, or parabolic feed array shapes have been introduced to perform multibeam scanning while minimizing phase aberrations [123], [137]. In [122], the analytic definition of the shape of the feed array is presented. This method is presented in Chapter 4, for the analysis of a rotationally symmetric lens.

The output pointing angle of the lens in Fig. 1.24 is expressed in terms of azimuth and elevation components $(\theta_{out,k}, \phi_{out,k})$. It is important to emphasize that when the azimuth input angle $\phi_{in,k}$ is defined, the corresponding output angle is uniquely determined by the following relationship: $\phi_{out,k} = \phi_{in,k} + 180°$, as in optics. The relation

between the output and input angles, as well as the sizes of back and front arrays, are described in Section 1.3.4. The physical length of the i-th delay line is denoted by the variable W_i. This variable has a crucial role in providing the desired phase delay between the back and front arrays for focalization, as elaborated in the next subsection.

1.3.3 Focal points and degrees of freedom

The focal points represent the solutions derived from the system of GO equations employed for the focalization of the lens. In the context of a 3D discrete lens, the focalization originating from an arbitrary focal point F_k is visually displayed in Fig. 1.25. Specifically, a focal point, defined by its coordinates $(\theta_{in,k}, \phi_{in,k})$, is expected to generate a plane wavefront with zero phase aberrations, referred to as Γ_k, in the correspondent directions $(\theta_{out,k}, \phi_{out,k})$. The collection of GO equations to be verified considering the focalization from the focal point F_k can be summarized as follows:

$$k_0|\overrightarrow{F_k B_i}| + k_g W_i + k_0|\overrightarrow{A_i P_{i,k}}| = \text{constant} \tag{1.2}$$

Being each term described afterwards:

- $k_0|\overrightarrow{F_k B_i}| = k_0\sqrt{(F_{x,k} - X_{B_i})^2 + (F_{y,k} - Y_{B_i})^2 + (F_{z,k} - Z_{B_i})^2}$, the phase delay in air between the generic focal point and each point of the back array;
- $k_g W_i$, the phase delays connecting the elements in the back and front arrays using waveguides having W_i as physical length and k_g the corresponding guided propagation constant;
- $k_0|\overrightarrow{A_i P_{i,k}}| = k_0[X_{A_i}\sin(\theta_{out,k})\cos(\phi_{out,k}) + Y_{A_i}\sin(\theta_{out,k})\sin(\phi_{out,k}) + Z_{A_i}\cos(\theta_{out,k})] + c_k$, the phase delay between each point of the radiating front array and the constant phase front considering its arbitrary constant term c_k to scan in the direction $(\theta_{out,k}, \phi_{out,k})$ in the point $P_{i,k}$.

The above GO focusing equation can be employed with any lens to examine the focusing from the focal points and guarantee zero aberrations. Now, let's focus on the general methodology (introduced in [122]) used to calculate the number of Degree of Freedoms (DoF)s or focal points of a 3D discrete lens, taking into account the constraints imposed by the shapes of the arrays.

The number of variables required to define a 3D discrete lens are 7 (as discussed in [122]) as following: the coordinates of the back array $\overrightarrow{O'B_i}$ (defining 3 variables), the delay lines between the two arrays W_i (defining 1 variable) and the coordinates of

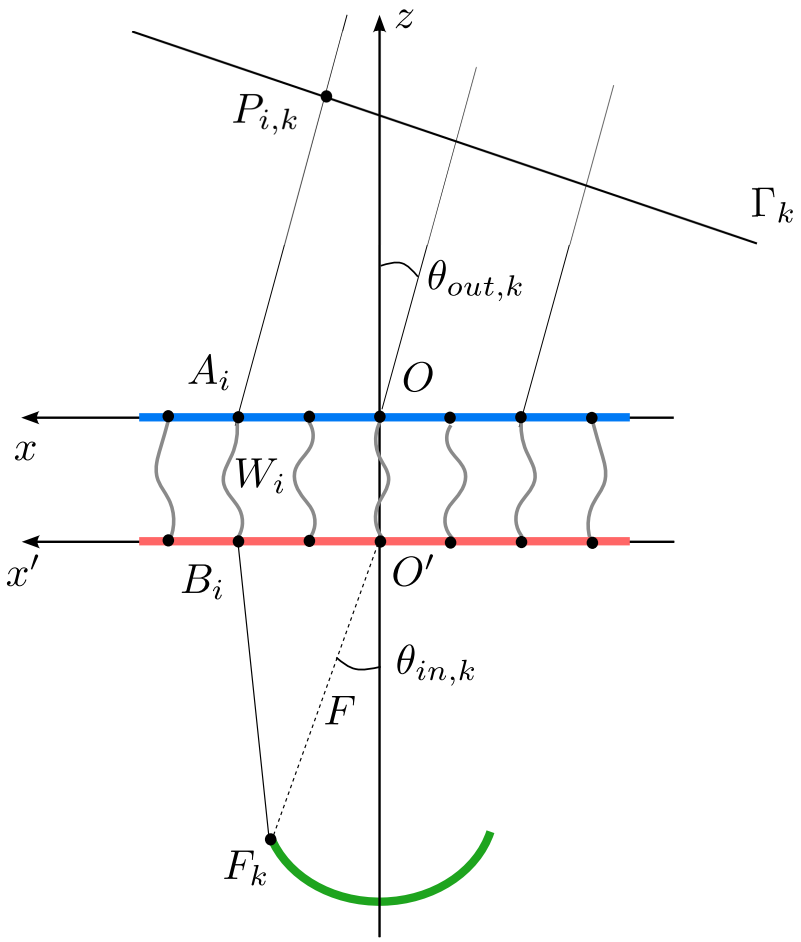

Figure 1.25 – Variables defining GO focalization of a 3D discrete lens from an arbitrary focal point F_k to generate a constant Γ_k plane wavefront in $(\theta_{out,k}, \phi_{out,k})$ in the xOz-plane.

the front array $\overrightarrow{OA}_i$ (defining 3 variables). When sizing the lens, it is usually necessary to fix either the size of the back or front array (therefore X_{B_i}, Y_{B_i} or X_{A_i}, Y_{A_i}) as independent variables, reducing the number of DoFs to 5 (here: $7-2=5$ DoFs). For this reason, 3D discrete lenses can exhibit up to 5 focal points [122]. Indeed, as more design variables are constrained for manufacturing limitations or to meet specific performance criteria, the number of DoFs or focal points reduces. Several examples illustrating these scenarios are provided analytically in [122].

An example to illustrate the concept of how the imposition of specific constraints can determine the number of focal points in a lens system is proposed. In McGrath's work, detailed in [123], a 3D discrete lens was constructed. This lens featured both flat back and front arrays, where $Z_{B_i} = Z_{A_i} = 0$, as a consequence exhibiting $7-2=5$ DoFs.

Additionally, the design involved fixing the elements in both arrays to be aligned in the same radial directions, exploiting a rotational symmetry (fixing their azimuth angle). As a result of these constraints, the lens achieved two focal points (in this case, $5-3=2$ DoFs). This example serves just as a practical application case demonstrating how the imposition of specific constraints can determine the number of focal points in a lens system. Taking a closer look, it is clear that a 2D discrete lens ordinarily exhibits a maximum of 4 focal points (in this instance, $5-1=4$ DoFs) as detailed in [104].

1.3.4 Magnification or zooming factor

In 1967, an additional parameter known as the zooming factor was introduced for bootlace lenses at Raytheon [112], [141]. This parameter allowed the manipulation of the ratio between the angle of incidence and the pointing angle in output of discrete lenses, which is directly related to the ratio of the front and back arrays. This zooming factor, which can also be referred today as the magnification factor (as mentioned in [22]), plays a crucial role in adjusting the magnifying effects of these radiative systems. It is worth mentioning that this type of zooming capability or magnification effect has already been employed in the context of reflector-based antennas [142], [143] to enlarge the dimensions of the focal feed array as well as in 2D discrete lenses [104].

In the context of this analysis, it is essential to establish a single fixed maximum pointing angle, denoted as θ_{out}^{max}, as well as to define the corresponding input or incident angle originating from the feed within the focal array, referred as θ_{in}^{max}. The formula that connects these input and output angles while incorporating the magnification or zooming factor M (as outlined in [104], [122]) can be expressed as follows:

$$\sin(\theta_{out}^{max}) = M \sin(\theta_{in}^{max}) \tag{1.3}$$

In Fig. 1.26 three different discrete lens scenarios varying the magnification factor M are compared for a generic lens with flat front and back arrays. In particular, the size of the front array D_A, the incident angle θ_{in}^{max} and the ratio F/D_B are fixed while the dimension of the back array D_B and the focal distance F vary considering the cases as following: (a) $M<1$, (b) $M=1$ and (c) $M>1$.

As illustrated in Fig. 1.26a, when $M<1$, the resulting output pointing angle is reduced compared to the incident input one (as $\theta_{out}^{max}<\theta_{in}^{max}$). In this case, the back array is reduced compared to the front one, achieving indeed a more compact and easily

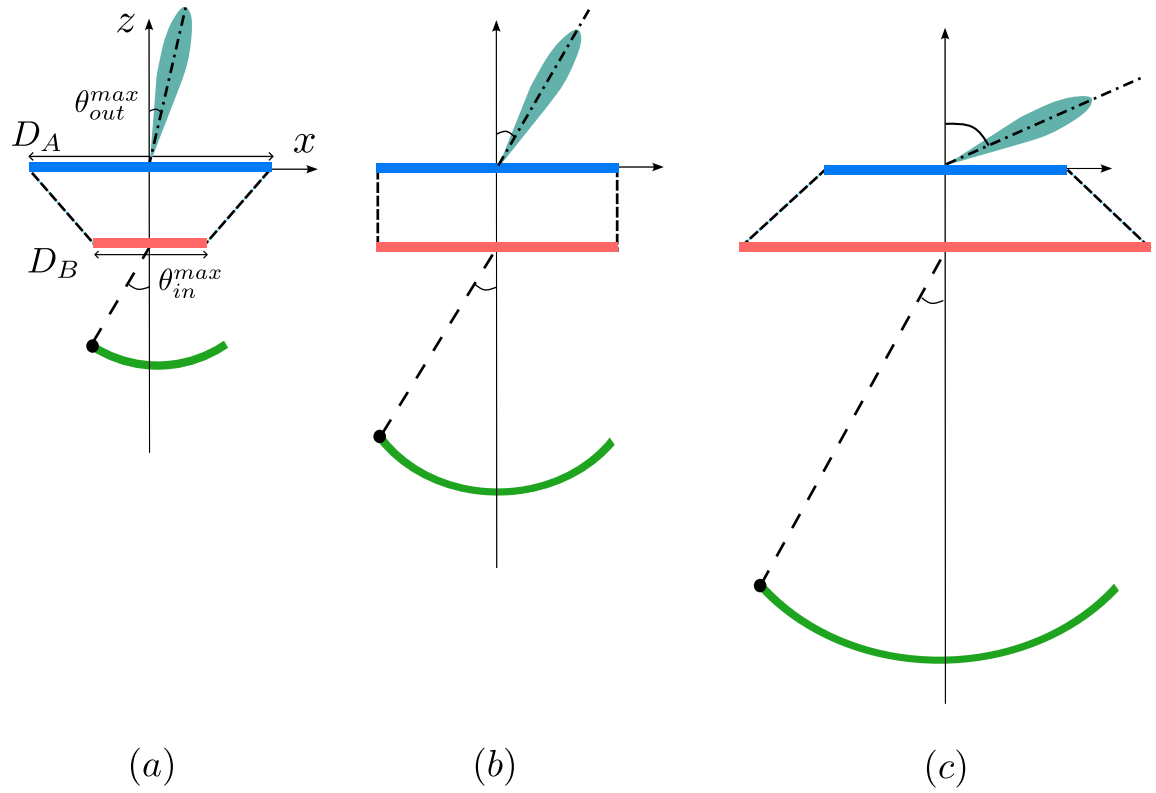

Figure 1.26 – 2D representation of a 3D discrete lens with flat front and back array. Cases: (a) $M < 1$, (b): $M = 1$, (c): $M > 1$.

implementable solution. It is relevant to note that reducing the linear dimensions by a factor of M results in a volume reduction of a factor M^3. This configuration is commonly selected when planning for scanning with a small FoV in order to achieve substantial reductions in the overall system volume. This specific condition is particularly suitable for applications such as on-board systems orbiting in GEO. In GEO payloads, the primary characteristic is a limited FoV and since these systems are positioned at a considerable distance from Earth, there is a need to minimize both their physical size and weight to mitigate power consumption.

In Fig. 1.26b, when $M = 1$, the incident and output pointing angles are exactly the same (as $\theta_{out}^{max} = \theta_{in}^{max}$). Correspondingly, the front and back arrays have the same sizes. For this reason, any overall system size reduction is achieved, as compared to the previous configuration. In addition, for this particular scenario, it is impossible to achieve large output pointing angles. This is due to the necessity of extremely high input angles illuminating the back array, as previously discussed in [122]. By increasing

θ_{out}^{max} and consequently θ_{in}^{max}, the size of the feed array becomes substantially larger than the back array, resulting in very poor illumination for angles exceeding approximately $\theta_{in}^{max} \sim 45°$, as discussed in [122]. Hence, when considering the use of these lenses in practical applications, it is important to take into account a larger overall volume compared to the previous case. This is particularly relevant for scanning scenarios that may involve angles of up to approximately $45°$, such as those encountered in ground stations, gateway antennas or when dealing with payloads in Medium Earth Orbit (MEO).

In the case of $M > 1$ (depicted in Fig. 1.26c), an increment of the size of the back array compared to the front one is obtained, guaranteeing good illumination. This time, the accommodation is increased, with an increment of the overall volume of about M^3. The limitation related to the increment of the volume can be tolerated for ground-based or gateway antennas, in particular considering extended scanning FoV applications. However, it is important to note that this time, when increasing the size of the back array relative to the front one, there is an additional advantage in terms of the output pointing angle (as $\theta_{out}^{max} > \theta_{in}^{max}$). It becomes indeed possible to scan angles that are larger than the input angles by applying a magnification factor greater than one.

Accordingly, when designing a 3D discrete lens, various options on the magnification factor can be chosen based on the particular application scenario. This choice takes into account factors such as scanning within the FoV and the volume accommodation of the entire system. For this reason in the next chapters, a detailed examination of the two extreme cases is carried out: a scenario with a narrow FoV and another with a wide FoV (respectively Chapter 3 and Chapter 4) employing different values of magnification factor.

1.3.5 Radiation pattern analysis

The simplified scalar formula employed to define the radiation pattern R_k of a 3D discrete lens considering the k-th generic feed in input is expressed in terms of electric field as following:

$$R_k(\theta,\phi) = \sum_{i=1}^{N_{tot}} \frac{a_{i,k}}{a_{1,k}} e^{-jk_g W_i} EF_i(\theta,\phi) e^{-jk_0[X_{A_i}\sin(\theta)\cos(\phi)+Y_{A_i}\sin(\theta)\sin(\phi)+Z_{A_i}\cos(\theta)]} \tag{1.4}$$

When the lens is rotational symmetric the ϕ-dependence could be omitted, while

for the other cases it should be considered. The first term $\frac{a_{i,k}}{a_{1,k}}$ of Eq. 1.4 describes the amplitude and phase taperings within the back array where:

- the amplitude tapering $|a_{i,k}|$ mainly depends on the spherical free-space propagation from the feed to the back array as $\frac{1}{|\overrightarrow{F_k B_i}|}$ and the product of the element patterns associated with them (depending on the chosen antenna). It is important to highlight that to improve the amplitude tapering can be possible by means of an active control of the lens.
- the phase tapering $\angle a_{i,k} = -k_0|\overrightarrow{F_k B_i}|$ is determined by the distance in air between the generic feed position and the elements of the back array, with k_0 representing the propagation constant in air.

The second term $e^{-jk_g W_i}$ represents the phase delays between the back and front arrays considering waveguides as delay lines. In particular, the W_i represents the physical waveguide length and k_g the corresponding guided propagation constant. The third term $EF_i(\theta, \phi)$ characterizes the embedded pattern of the i-th element of the front array and it is better analyzed in the next chapters. The last term represents the phase delays related to the positions of the front array elements and the considered directions.

By utilizing the formula in Eq. 1.4, it becomes possible to examine the radiation features of a 3D discrete lens system, regardless of its geometry, which may include other profiles of the back and front lens, varying the number or the position of the feed and whether or not it is rotational symmetric.

1.4 Conclusion

This chapter has provided an introduction to high-gain antennas to reach 3D flexibility in multibeam scanning. These antennas are crucial for current and future space applications, whether on-ground or on-board various platforms.

The comparison between different radiating solutions that employ metallic materials has been carried out. These solutions aim to provide a good balance between extreme flexibility on one hand and high power handling with minimal losses on the other. Within this examination, a comparison on reflector-based, array of antennas and lens systems has been carried out, showing their principal benefits and limitations.

This analysis highlights that 3D discrete lenses emerge as an excellent choice for achieving highly flexible scanning capabilities among multiple directions. Notably, the ratio between the sizes of the back and front arrays called also magnification factor

plays a significant role in influencing both the input and output FoVs, allowing them to achieve flexible coverage. Additionally, they offer quasi free-space beamforming capabilities since beam formation occurs almost in an air-like environment and without the need for multiple BFNs. Furthermore, the integration of active controls along their chain enhances their performance in terms of illumination, crossover levels for contiguous multi spot coverages and minimizes spillover losses. Moreover, they have the capacity to support dual polarization features for their 3D geometry. However, it is important to note that these advantageous features necessitate the use of bulky systems, especially when considering their full-metal implementations.

Today, significant developments in 3D printing technology enable design of very cost-effective complex systems. Specifically, full-metal AM simplifies the production of exotic geometries compared to TM methods. The use of full-metal AM technologies also allows the construction of monolithic components, eliminating the interfaces between interconnected parts. This not only reduces weight but also enhances mass savings while minimizing losses associated with interconnections.

The development of 3D discrete lenses through full-metal AM is taken into account in this thesis. These lenses are deployed to work in different application scenarios spanning from narrow to wide FoVs, as extensively discussed in Chapter 3 and Chapter 4. Another noteworthy innovation involves also the capability to design curved waveguides to be employed within 3D discrete lenses to reach the desired phase delays for focusing. In particular, such novel waveguides referred to as MWs are conceived and analyzed in the next chapter.

CHAPTER 2

Meandered waveguides

2.1 Introduction

Controlling phase delays of guided waves is essential in the design of RF systems requiring signal distribution, recombination or beamforming. Such functionality is implemented in a wide range of devices, spanning from simple components such as turnstile ortho-mode transducers or mode extractors [144], to more complex distribution systems such as multiport amplifiers [145] or antenna BFNs [146], [147]. The control of the phase delay combined with spatial routing of the signals can become an important challenge. The typical accommodation constraints are related to the two profiles to be interconnected. These profiles, incorporating elements such as radiators linked to thermal blocks or amplification controls, are principally separated by a vertical distance separating them. Additionally, they may each feature different periodicity and lattice structures to accommodate different blocks. In this context, routing mechanisms providing high flexibility are typically desired [148]–[150]. This is the reason for their investigation in this thesis.

The most frequent solution for the RF signals spatial routing is based on the use of transmission lines implemented in a PCB layout (microstrip and stripline, among others), as in [151], [152]. This configuration is chosen for its low cost and high suitability for integration of active electronic components. Still, this solution is very limited for spatial routing, it has significant insertion losses and is only applicable in low power systems. Coaxial cables are an alternative to PCB routing since they allow the intercon-

nections with complex 3D trajectories [127], [153] with medium insertion losses. However, their high power handling is still an issue since they employ dielectric materials. Conventional waveguides allow for signal routing with very low insertion losses and high power handling [154]–[157]. Yet, their fabrication is very cumbersome, since it involves the assembly of discrete waveguide parts (including bends, twists, etc), which might lead to practical performance issues due to imperfect assembly. Substrate Integrated Waveguide (SIW) and the recent air-filled version (AFSIW), appear as a compromise between waveguides and PCB technology products, offering medium loss and low cost devices, [158], [159]. High power handling and 3D routing are still an issue in these two technologies.

In this context, AM appears as an enabling solution to conceive routing networks that combine low insertion losses, high power handling, extreme flexibility and low cost [160]–[162]. For this reason, in this thesis we have devoted the first efforts to characterize MWs. The concept of MW was firstly proposed for 3D routing in [149]. Such a preliminary result represents one of the main motivations of this thesis. MWs permits to synthesize desired phase delays by tuning the curvature between two assigned points. The resulting complex curvatures can only be fabricated in AM technology. Indeed, such technology enables monolithic pieces or even monolithic clusters, thus simplifying problems associated to assembly. RMWs represent a step further in the conception of MWs, since they also entail an enhancement of the bandwidth. In fact, they present an interesting middle point between the non-dispersive TEM propagation of coaxial cables and the limited bandwidth of conventional waveguides.

To highlight the performance of AM waveguides, Fig. 2.1 offers a comparison of transmission losses across various technologies previously discussed. These technologies encompass a possible type of coaxial cable (labeled as reference number C32SZ(3Q) [163]), a 50 Ohms microstrip line constructed using copper for the conductive component and Rogers 6002 for the substrate, an AFSIW utilizing Rogers 6002, as detailed in the paper [164] on page 1230, and measurements acquired from SWISSto12 for an AM process employing plating to build a conventional rectangular waveguide. It is clear that the AM waveguide technology allows for significant reduction in transmission losses compared to the other technologies, which is the primary reason for selecting it in this thesis.

The chapter is organized as follows: the first part presents the analytic description of the MW trajectory connecting two points allowing the building of the path through a

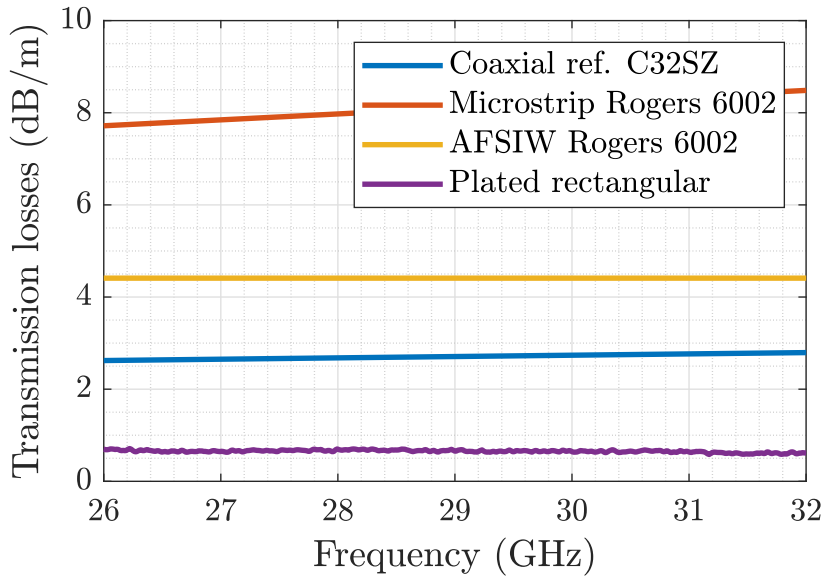

Figure 2.1 – Comparison of transmission losses between coaxial cables, microstrip lines, AFSIW technology and AM waveguide implementing chemical plating.

modulated function and the dual-ridge cross-section evolution along it. Consequently, the phase delay synthesis methodology is presented and some numerical examples and simulations are provided. Finally, the analysis and design of RMW clusters to be employed in several space scenarios is proposed.

2.2 Building guidelines

MWs can be defined as waveguides with a modulated trajectory along the propagation axis. The goal is to design MW able to connect two assigned points (indicated as starting and ending points P_s and P_e) through a tailored trajectory that guarantees a desired phase delay. To design a MW, two waveguide ports placed in the starting and ending points should be connected. The following hypothesis are here considered (as displayed in Fig. 2.2):

- the two waveguide ports have the same cross-section, which is maintained throughout the trajectory;
- the waveguide ports centered in the starting and ending points are parallel to the xy-plane;

- the profile followed by the MW should be characterized by a continuous function and with a continuous first derivative to ensure smoothness.

The problem consists on: the design of the MW centerline or trajectory connecting the two points, the definition of the modulation function, the design of the waveguide along the modulated trajectory and the correspondent phase delay synthesis.

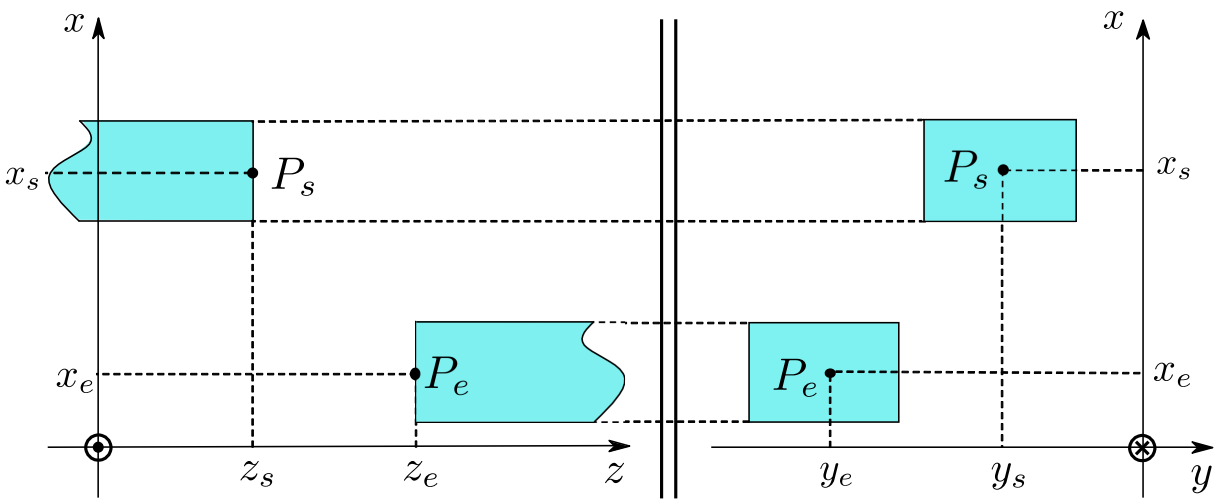

Figure 2.2 – Waveguide connection specifications from the starting point P_s of coordinates $[x_s, y_s, z_s]$ to the ending point P_e of coordinates $[x_e, y_e, z_e]$. On the left side: xOz-plane view (lateral view), on the right side: xOy-plane view (cross-section view).

2.2.1 Trajectory baseline

To build the modulated trajectory, an auxiliary axis t that connects the points P_s (where $t = 0$) and P_e (where $t = 1$) is considered as centerline (see Fig. 2.3).

The 3D trajectory path curve described by $P(t)$ starts at P_s and ends at P_e following the conditions:

$$\begin{cases} P(0) = P_s \\ P(1) = P_e \end{cases} \tag{2.1}$$

and it is built in such way to enable an arbitrary modulation of the phase delay. The curve should be perpendicular to the xy-plane at $t = 0$ and $t = 1$ to ensure differentiability at the connection points.

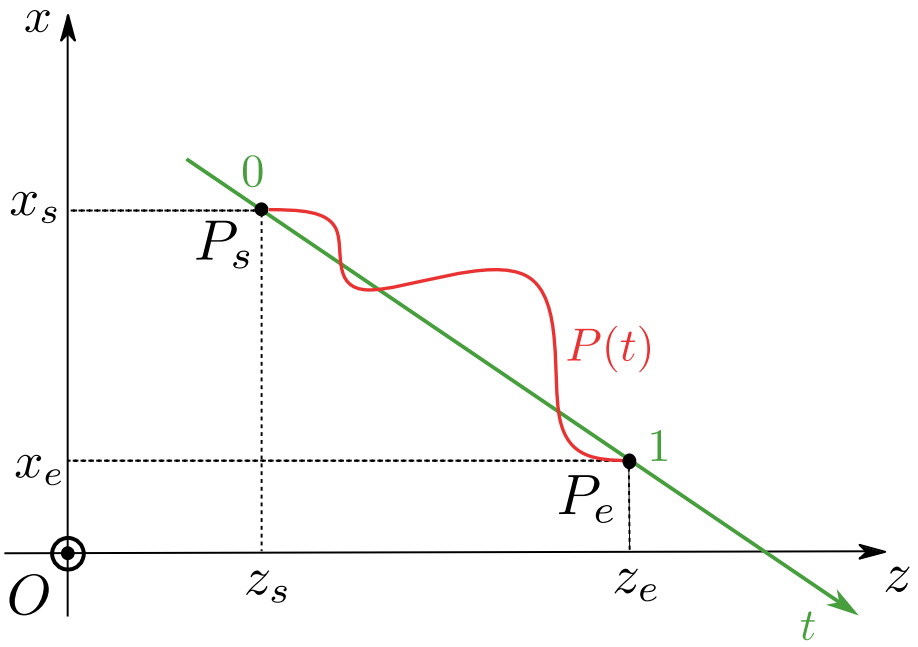

Figure 2.3 – xz-plane projection of the trajectory path curve $P(t)$ (in red) between the starting and ending points defined in t coordinate system (in green).

To reach these goals, the MW trajectory $P(t)$ is defined as follows:

$$\overrightarrow{OP}(t) = \overrightarrow{OP_s}(t) + \vec{b}(t) + \vec{m}(t) \tag{2.2}$$

where O is the coordinate system origin, $\vec{b}(t)$ a baseline function to properly connect P_s and P_e and $\vec{m}(t)$ a modulating function to synthesize the phase delay. To satisfy Eq. 2.1, the following relations are verified:

$$\begin{cases} \vec{b}(0) &= \vec{0} \\ \vec{b}(1) &= \overrightarrow{P_sP_e} \\ \vec{m}(0) &= \vec{0} \\ \vec{m}(1) &= \vec{0} \end{cases} \tag{2.3}$$

While, in order to ensure differentiability in the connection points, conditions on the derivative functions are included:

$$\begin{cases} \frac{d\vec{b}}{dt}(0) \text{ and } \frac{d\vec{b}}{dt}(1) \text{ both oriented along } \hat{z} \\ \\ \frac{d\vec{m}}{dt}(0) \text{ and } \frac{d\vec{m}}{dt}(1) = \vec{0} \end{cases} \tag{2.4}$$

Thus, the baseline is defined as follows:

$$\vec{b}(t) = (x_e - x_s)s(t)\hat{x} + (y_e - y_s)s(t)\hat{y} + (z_e - z_s)t\hat{z} \tag{2.5}$$

being $s(t)$ the step function defined employing the formulation proposed in [165]:

$$s(t) = \frac{1}{\beta w}\ln\left(\frac{1 + e^{\beta(t-t_0+w/2)}}{1 + e^{\beta(t-t_0-w/2)}}\right), \quad t \in [0, 1] \tag{2.6}$$

where t_0 defines the inflection point of the step function while w and β are the slope parameters (Fig 2.4). These parameters can be used as degrees of freedom, giving flexibility in the design of MW. To verify the conditions of continuity and derivability in Eq. 2.3 and Eq. 2.4, the following conditions are determined experimentally: $\beta w \geq 11$ for $t_0 = 0.5$, while $\beta w \geq 22$ for $t_0 = 0.4$ or 0.6, as shown in Fig 2.4.

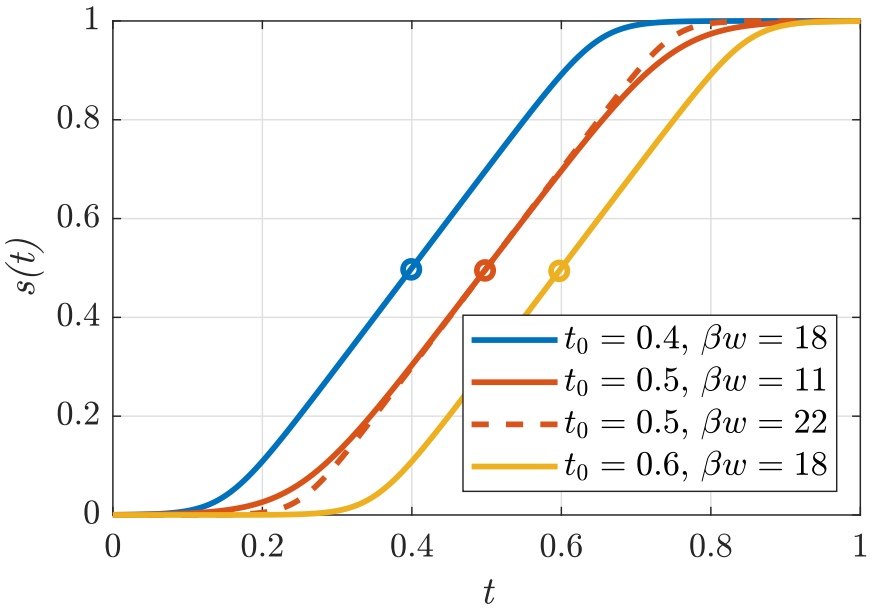

Figure 2.4 – Examples of step functions $s(t)$ varying the inflection point t_0 and the product βw to verify the conditions of continuity and derivability (Eq. 2.3 and Eq. 2.4).

2.2.2 Modulation function

To synthesize different phase delays while still verifying the conditions on the continuity and derivability, the modulating function is added:

$$\vec{m}(t) = m(t)\vec{e}_m \tag{2.7}$$

where $\vec{e}_m = \delta\hat{x} + \gamma\hat{y}$ is a unit vector defining in which plane the modulation is applied. This plane can be freely chosen. The modulation $m(t)$ is given by the trigonometric function:

$$m(t) = A\sin(\pi P t)\sin^2(\pi t) \tag{2.8}$$

being A the amplitude and P the semi-periods. Such parameters represent the degrees of freedom that allow to control the trajectory baseline modulation and thus the phase delay to be synthesized, as discussed in [149]. The second quadratic term in Eq. 2.8 guarantees that the bend in the edges of the path are smaller than the one in the center acting as a spatial window, to facilitate the manufacturing process. Some examples are depicted in Fig. 2.5 displaying multiple combinations of amplitude and semiperiod within the modulation functions. Note, that the phase delay of a MW could be reached by multiple combination of such parameters, as better analyzed in the next section.

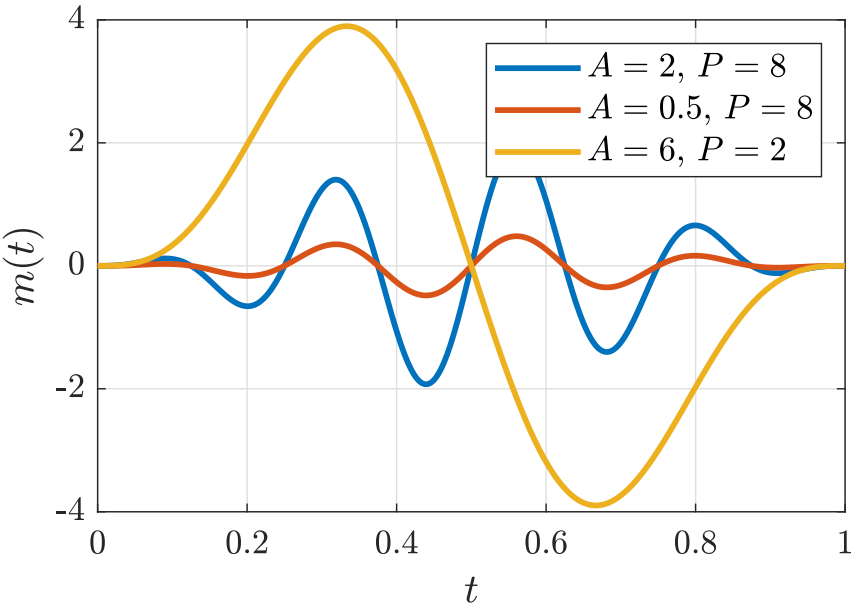

Figure 2.5 – Modulation function $m(t)$ with different modulation parameters.

2.2.3 Parallel transport approach

In order to build accurately a MW, a smooth evolution of the cross-section along the trajectory $\overrightarrow{OP}(t)$, based on the parallel transport approach [166]–[168], is implemented. Through this algorithm, an orthonormal basis of vectors $(\vec{n}, \vec{u}, \vec{v})$ is built along the modulated centerline from the starting to the ending points maintaining the same orientation, as displayed in Fig. 2.6 for a simple rectangular waveguide.

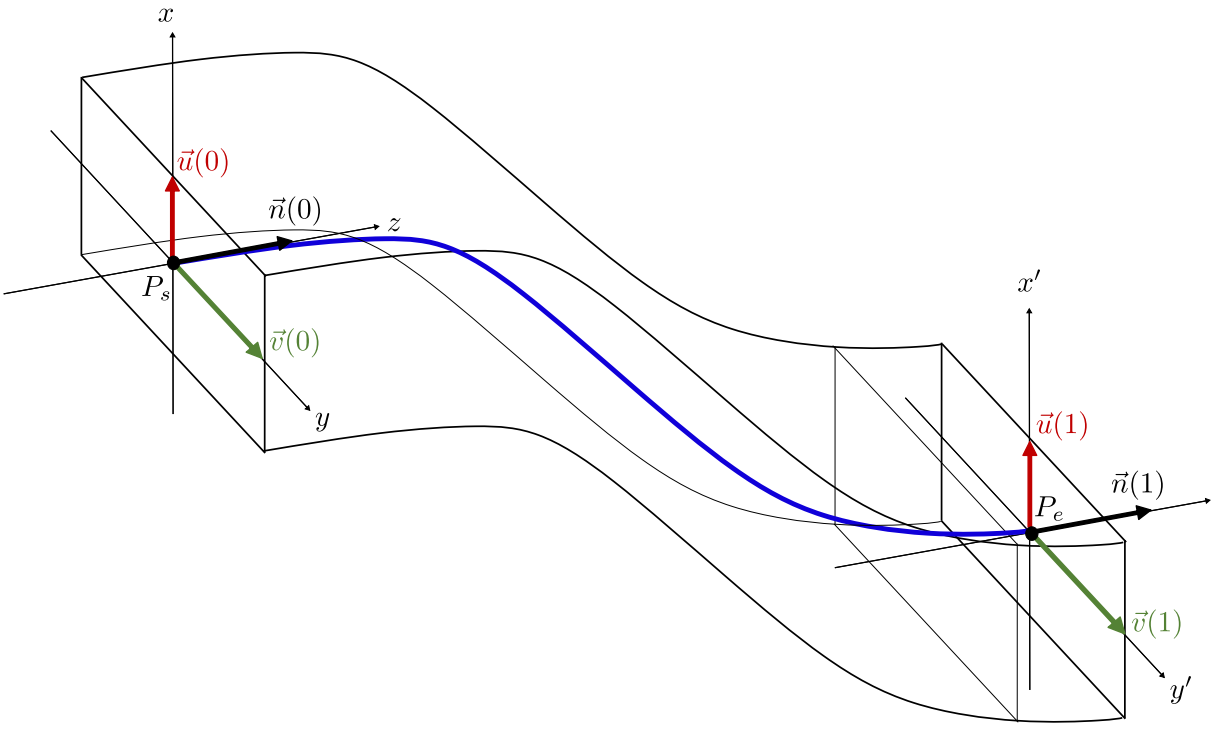

Figure 2.6 – Orthonormal basis $(\vec{n}(t), \vec{u}(t), \vec{v}(t))$ along a centerline $\overrightarrow{OP}(t)$ (in blue) connecting starting and ending points and considering a rectangular waveguide cross-section.

As explained in [166], such approach has been chosen since it avoids the issue of orientation inversion in non-convex or vanishing curves, which is happening for the Frenet frame approach. Figure 2.7 displays the comparison between the two approaches considering: (a) a convex curve which is the same for both Frenet and parallel approaches, (b) a non-convex curve for the Frenet frame with the inversion of direction within the curve at each inflection point and (c) the non-convex curve considering the parallel transport approach without any inversion.

The implemented basic steps of the parallel transport algorithm for piece-wise linear curves are here defined step by step, depicted in a schematic way in Fig. 2.8.

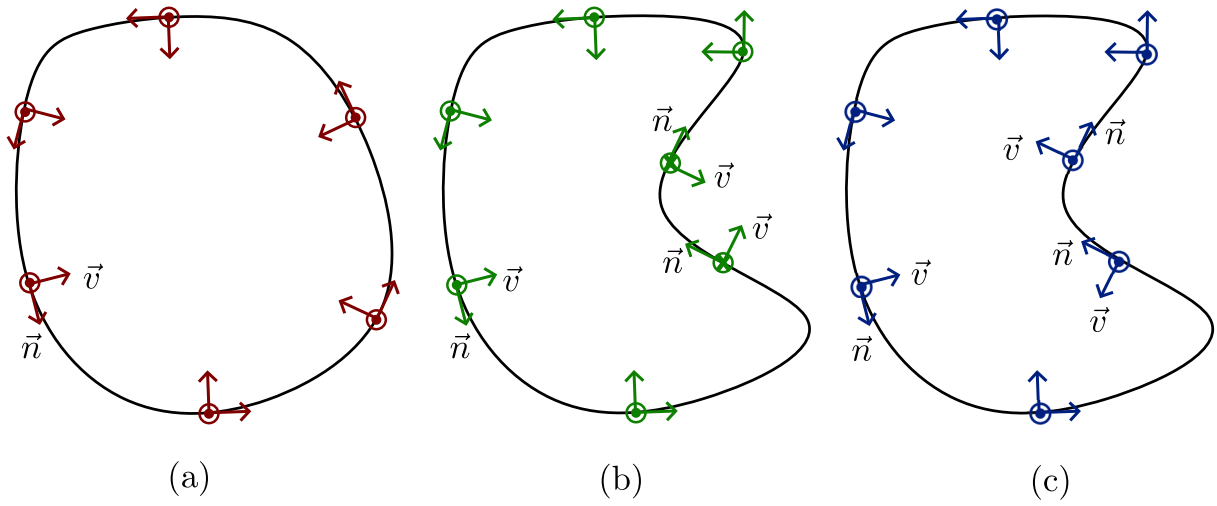

Figure 2.7 – Comparison of the Frenet frame and parallel transport approaches on plane curves considering the basis $(\vec{n}, \vec{u}, \vec{v})$ where $\vec{u}$ is pointing out of the paper. (a) Convex curve. (b) Non-convex curve: Frenet frame approach. (c) Non-convex curve: parallel transport approach.

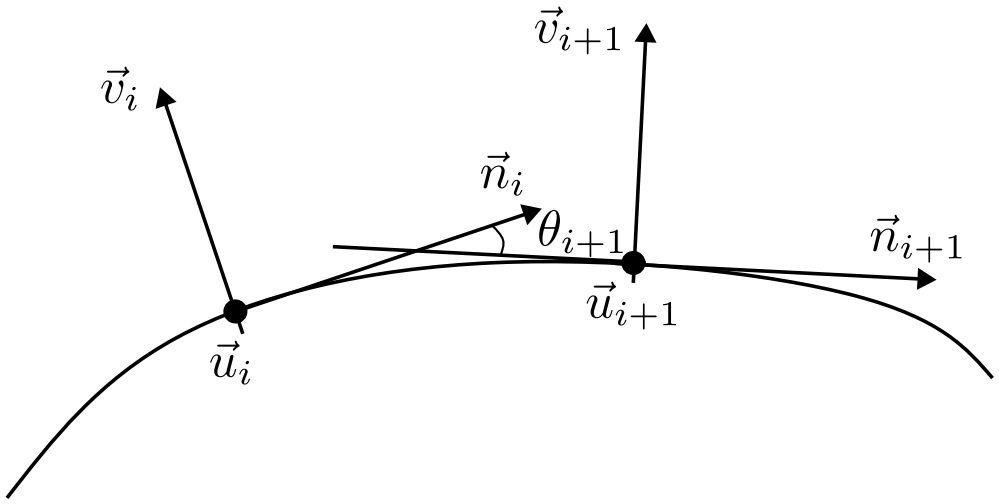

Figure 2.8 – Schematic of the orthonormal basis implemented along the trajectory curve between the steps t_i and t_{i+1} using the parallel transport approach algorithm.

The unit vector perpendicular to the arbitrary cross-section (and tangential to the trajectory) is described by:

$$\vec{n}_{i+1} = \frac{\overrightarrow{P_i P}_{i+1}}{||\overrightarrow{P_i P}_{i+1}||}, \quad i = 0, .., N-2 \tag{2.9}$$

where the variable are simplified as: $P(i) = P(t_i)$, $\vec{n}_i = \vec{n}(t_i)$ and evaluated in the set of points $t_i = i/N$ (where N is sufficiently high for a good approximation). At the extreme

points of the trajectory, the tangential vector must be parallel to the z-axis: $\vec{n}_o = \vec{n}_N = \hat{z}$, as anticipated at the beginning of Section 2.2. The vector $\vec{u}$, perpendicular to the modulated centerline, is implemented starting from the choice of the initial orientation $\vec{u_0}$ (vector that defines the orientation of the waveguide cross-section at the starting point) as follows:

$$\vec{u}_{i+1} = R(\theta_{i+1}, \vec{B}_{i+1})\vec{u}_i, \quad i = 0, .., N-1 \tag{2.10}$$

where the vector $\vec{B}_{i+1}$ is evaluated as:

$$\vec{B}_{i+1} = \frac{\vec{n}_i \times \vec{n}_{i+1}}{||\vec{n}_i \times \vec{n}_{i+1}||} \tag{2.11}$$

The evaluated angle between each step $\theta_{i+1} = \arccos(\vec{n}_i \cdot \vec{n}_{i+1})$. The rotation matrix $R(\theta, \vec{B})$ of the vector $\vec{B}$ about the angle θ is implemented from [166] as:

$$R(\theta, \vec{B}) = \begin{bmatrix} c + {B_x}^2(1-c) & B_xB_y(1-c) - sB_z & B_xB_z(1-c) + sB_y \\ B_xB_y(1-c) + sB_z & c + B_y^2(1-c) & B_yB_z(1-c) - sB_x \\ B_zB_x(1-c) - sB_y & B_zB_y(1-c) + sB_x & c + B_z^2(1-c) \end{bmatrix} \tag{2.12}$$

where $c = \cos(\theta)$ and $s = \sin(\theta)$. The third vector is expressed by the cross-product of the defined vectors: $\vec{v}_i = \vec{n}_i \times \vec{u}_i$. Such vectors form an orthonormal basis in each point of the discretized trajectory to define the cross-section evolution along it.

The implementation of MWs involves a process of replicating a cross-sectional configuration along the modulated curve. This replication follows the orthonormal basis established through the parallel transport approach in evaluation points denoted as t_i. An illustrative example can be seen in Fig. 2.9, which depicts the utilization of the parallel transport approach basis to build a MW centerline with parameters $A = 2$ and $P = 8$, presenting three different perspectives.

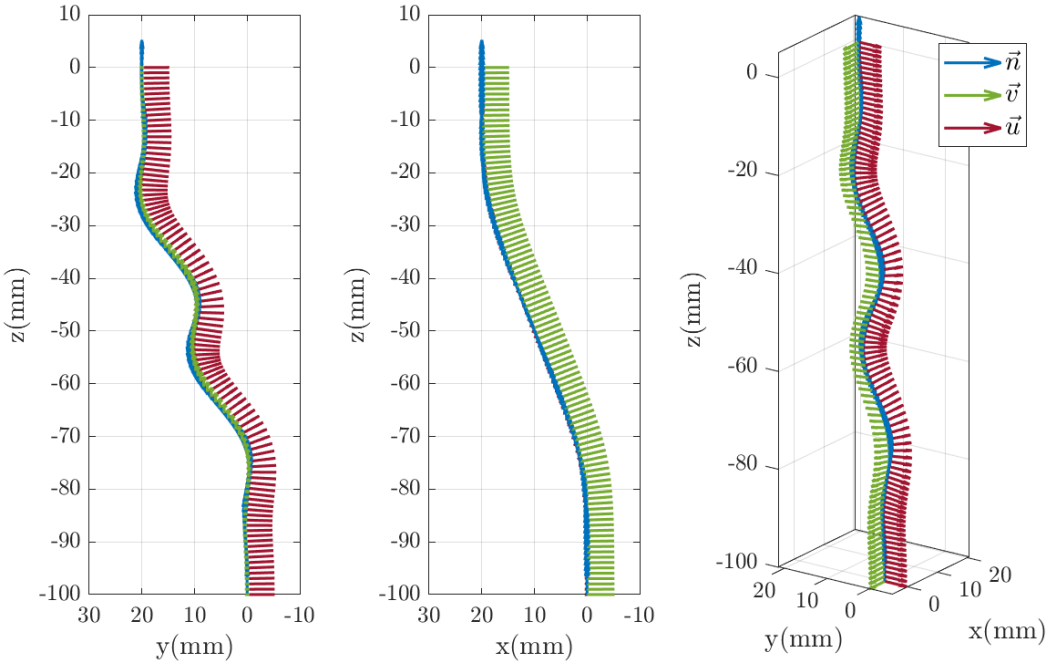

Figure 2.9 – Parallel transport basis along a modulated centerline with modulation parameters $A = 2$ and $P = 8$ connecting two defined points.

2.2.4 RMW cross-section

The parallel transport approach can be applied to any type of waveguide cross-section to build a MW. In this thesis, the waveguides are mainly implemented considering a dual-ridged inset, as showed in Fig. 2.10. In addition, to facilitate the fabrication through AM techniques, rounded corners can be also considered.

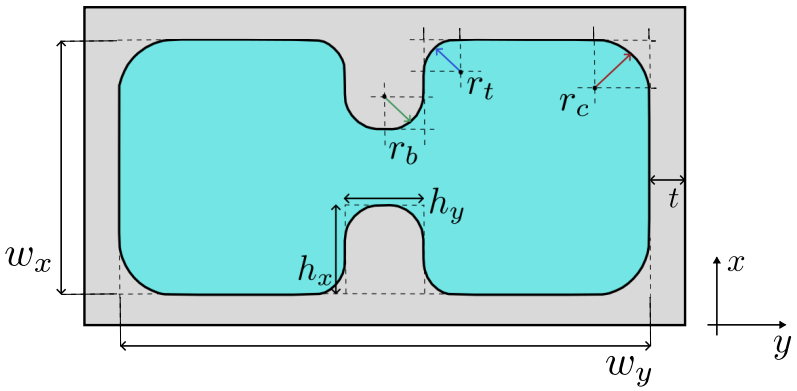

Figure 2.10 – RMW cross-section with rounded corners.

The ridges allow to increase the single-mode bandwidth of the waveguide since they lower the cut-off frequency of the fundamental mode. In Fig. 2.11, four waveguides with different cross-sections are considered and the corresponding dispersion curves are compared (k_g and k_0 are respectively the waveguide and the free-space propagation constants). When decreasing the cut-off frequency of the fundamental mode, the propagation constant vs frequency becomes more linear around the selected operation frequency $f_0 = 28.5$ GHz. In fact, achieving a flatter curve corresponds to an optimal true-time delay and broadband operation. It is interesting to notice the difference between the black curve (conventional rectangular waveguide) and the blue curve (dual-ridged waveguide) and how the ridge waveguide enables wave guiding with reduced influence of the dispersion inherent to waveguides.

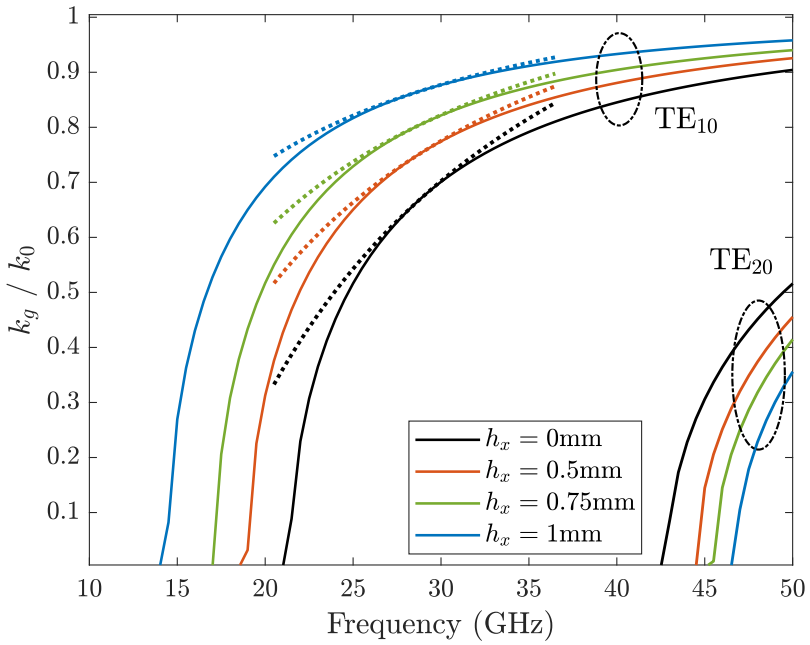

Figure 2.11 – Dispersion curves of rectangular and dual-ridge waveguides for the two first propagating modes (TE$_{10}$, TE$_{20}$) with $w_x = 3$ mm, $w_y = 7$ mm, $r_t = 0$ mm, $r_b = 0$ mm, $r_c = 0$ mm and $t = 0.25$ mm.

2.2.5 Numerical examples

To build a MW of arbitrary cross-section in CST Microwave Studio (CST), an interface code is implemented in order to read the parameters related to the modulated curve

and the orthonormal basis along the curve in all the set points determined in MATLAB. In CST, the user can build the MW to simulate, being able to define arbitrarily:

- the cross-section (rectangular, single or dual-ridge with corner roundings or not, etc.) of the waveguide;
- the possibility to create automatically two waveguides (one parallel to the other), in order to support dual polarized signals through a dual channel structure;
- the parameters defining the step function connecting two points and the modulation parameters;
- the plane of modulation, as outlined in the context of Eq. 2.7. E-plane modulation corresponds to $\delta = 1$, $\gamma = 0$, while H-plane modulation corresponds to $\delta = 0$, $\gamma = 1$. Additionally, arbitrary intermediate cases are possible.

In Fig. 2.12 some examples of RMWs employing a dual-ridged waveguide cross-section with rounded corners (as in Fig. 2.10) are depicted. The example in Fig. 2.12a shows a simple step function with a displacement in the y and z coordinates, while from Fig. 2.12b to Fig. 2.12d RMWs with exotic meanderings and displacements in all the coordinates that can be achieved are showed.

Figure 2.13 provides additional examples of RMWs without employing rounded corners, illustrating the potential for implementing different cross-section shapes and implementing also the dual channel option. In Fig. 2.13a a waveguide with a step centerline without any modulations is shown. In contrast, Fig. 2.13b showcase RMWs with a modulation function applied in the E-plane and Fig. 2.13c shows two modulated waveguides in the H-plane with dual channel option activated typically employed for dual polarized routing. These waveguides are extremely versatile and can be easily adapted for a huge range of specifications.

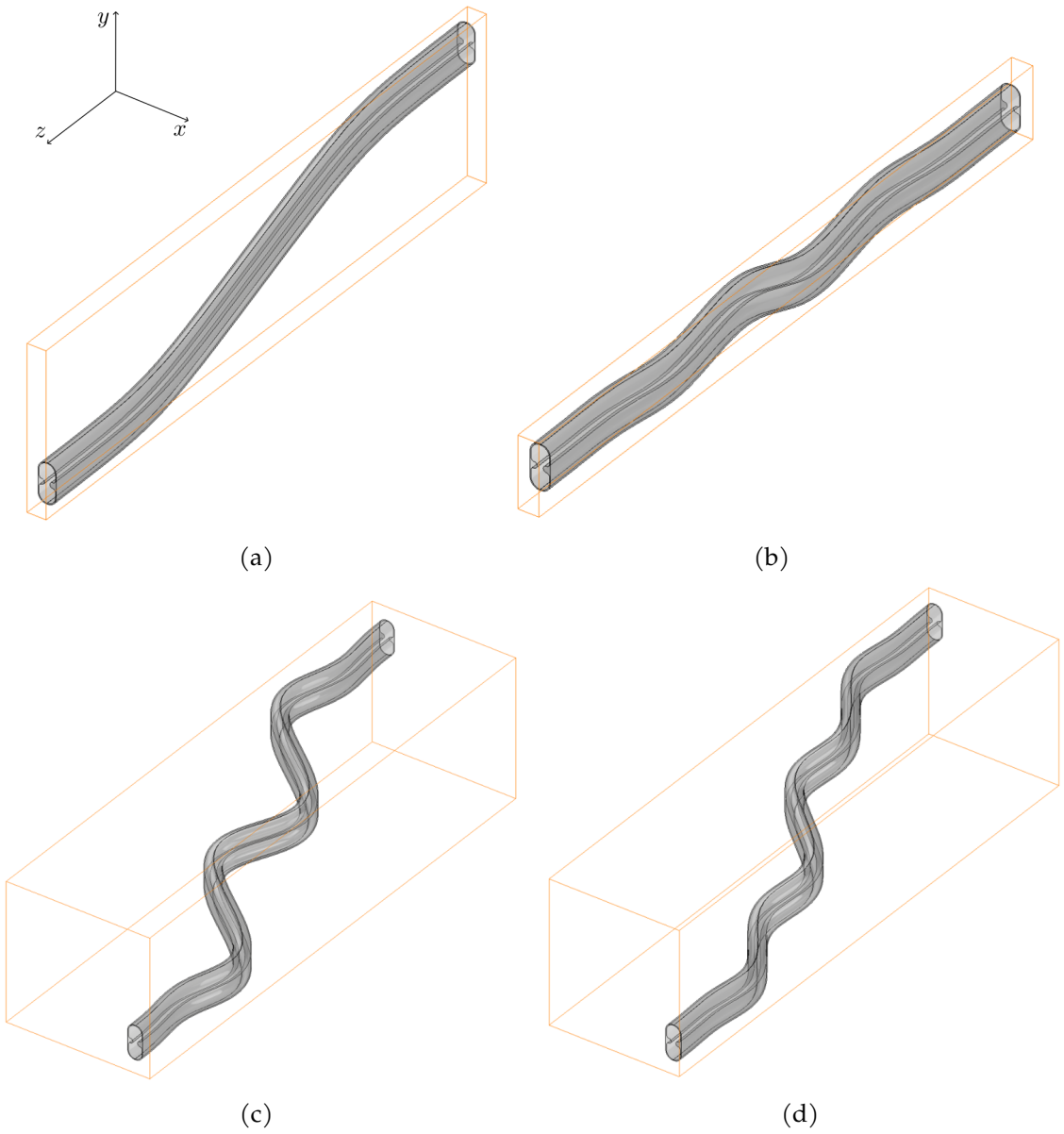

Figure 2.12 – Examples of RMWs with rounded corners with different curvatures between two points $P_s(x_s, y_s, z_s)$ and $P_e(x_s+\Delta_x, y_s+\Delta_y, z_s+\Delta_z)$: (a) step function with displacement $\Delta_x = 0, \Delta_y = 2\lambda_0, \Delta_z = 10\lambda_0$, (b) meandering in the H-plane with $A = 2$, $P = 4$ and displacement $\Delta_x = 0, \Delta_y = 0, \Delta_z = 10\lambda_0$, (c) meandering in the E-plane with $A = 8$, $P = 6$ and displacement $\Delta_x = 4\lambda_0, \Delta_y = 2\lambda_0, \Delta_z = 10\lambda_0$, (d) meandering in the E-plane with $A = 4$, $P = 8$ and displacement $\Delta_x = 2\lambda_0, \Delta_y = 2\lambda_0, \Delta_z = 10\lambda_0$.

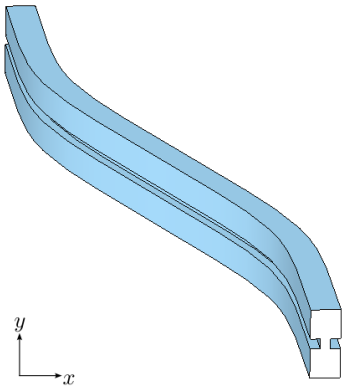

(a)

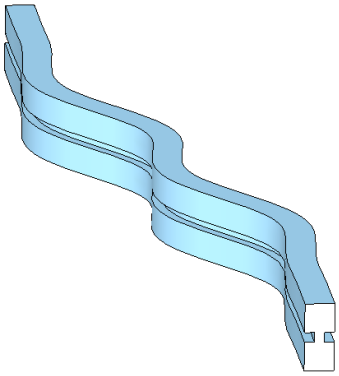

(b)

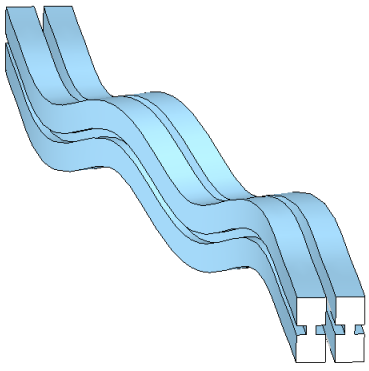

(c)

Figure 2.13 – Examples of RMWs without rounded corners different curvatures between two points $P_s(x_s, y_s, z_s)$ and $P_e(x_s+\Delta_x, y_s+\Delta_y, z_s+\Delta_z)$ with the same displacements $\Delta_x = 0, \Delta_y = 2\lambda_0, \Delta_z = 10\lambda_0$: (a) step function ($A = 0$) with centerline length $L_a = 108.60$ mm, (b) meandering in the E-plane with $A = 3$, $P = 6$ centerline length $L_b = 111.46$ mm, and (c) dual channel meandering in the H-plane with $A = 3$, $P = 6$ centerline length $L_c = 111.28$ mm.

2.3 RMW synthesis

The flexibility of the proposed method to build RMWs consists in connecting two arbitrary points and playing on the modulation parameters (A and P), to properly match the specifications on phase of the RF signals. In this section, the synthesis of phase delays in RMWs is presented and involves the comparison between the desired and obtained phase delays through full-wave simulations in CST. Considerations regarding the manufacturing guidelines for RMWs, aimed at minimizing potential reactive effects that could influence the synthesis of the phase delays are also introduced.

2.3.1 Phase delay optimization

The RMW design process starts by defining the step function connecting two arbitrary points. In this case, in order to avoid discontinuities at the connection points and sharp slopes, the inflection point is fixed in the center $t_0 = 0.5$ and the inclination parameters are $\beta w = 11$ with $\beta = 22$ and $w = 0.5$, as anticipated in Section 2.2.1.

The phase delay of a RMW can be approximately computed as following: $\Phi_g = k_g W$, being $k_g = k_0\sqrt{1-(\frac{f_c}{f})^2}$ the propagation constant of a conventional waveguide with f_c the cut-off frequency, f the central frequency, k_0 the free-space propagation constant and W the correspondent centerline length. To synthesize a given phase delay Φ_{des}, the designer can adjust both the centerline length W (through A and P) and k_g (through the cut-off frequency of the fundamental mode in the RMW, by adjusting the cross-section dimensions). The optimization process involves minimizing the difference between the desired phase delay and the simulated one.

Initially, the process involves specifying the desired phase delay using MATLAB. Subsequently, the simulated phase delay is refined in CST. This optimization process becomes more accurate by considering the actual propagation constant and accounting for reactive effects associated with curvatures, ultimately providing a more accurate result. When connecting two points through an arbitrary MW, a desired delay line can be obtained with several design parameter combinations. As an example, Fig. 2.14a shows the semi-period P as a function of the amplitude modulation A that leads to a specific modulated centerline length ($L = 200$ mm).

Obviously, strong curvatures induce reactive effects that affect the RMW centerline length synthesis and should be avoided (these cases correspond to extreme values of A and P). For this reason, if possible, intermediate values of A and P are recommended

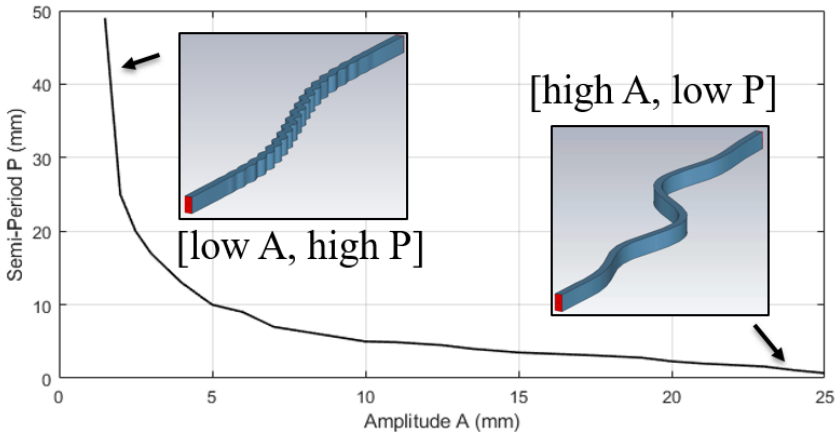

Figure 2.14 – Semi-periods vs amplitude modulation parameters synthesizing the same modulated centerline length.

to bypass the mismatching between simulated and desired RMW phase delays. It is important to note that it is not possible to derive with a single analytic equation the couple of perfect values for A and P, since reactive effects could not be easily predicted. The choice of A and P is also made by considering the available space to accommodate the RMW and its physical manufacturability, in particular when they are implemented in groups. A design recommendation is to use a separation between the two points such that the bends that appear along the centerline exhibit a bending radius larger than the height of the waveguide cross-section to avoid overlappings. This design recommendation produces bends in the centerline that are smooth and does not cause strong reactive effects that affect the insertion phase.

2.3.2 Validation

To demonstrate the effectiveness of the implemented tool for constructing, simulating and synthesizing RMWs, some examples are analyzed. The initial example involves a RMW characterized by a step function synthesizing a centerline length of $L_1 = 108.60$ mm, as depicted in Fig. 2.13a. Subsequently, two additional RMWs with the same cross-section are presented, featuring identical centerline lengths ($L_{2,3} = 110$ mm). In these examples, modulation functions are applied in the E-plane and H-plane, respectively. The modulation parameters are adjusted to achieve the same centerline length: $A_1 = 2.5$, $P_1 = 5.61$ for the E-plane, and $A_2 = 2.42$, $P_2 = 5.29$ for the H-plane.

In Fig. 2.15, a comparison is made between the simulated phase delays denoted

as Φ_g (colored curves) and the corresponding desired ones Φ_{des} (black curves) for the three RMWs. It is crucial to note that the desired phase is consistent for examples 2 and 3, whereas it differs for the first one due to its distinct centerline length. A strong agreement between the desired (depicted as a black dotted line) and the simulated phase delays are reached for the three examples, presenting phase errors below $2°$ within the considered bandwidth.

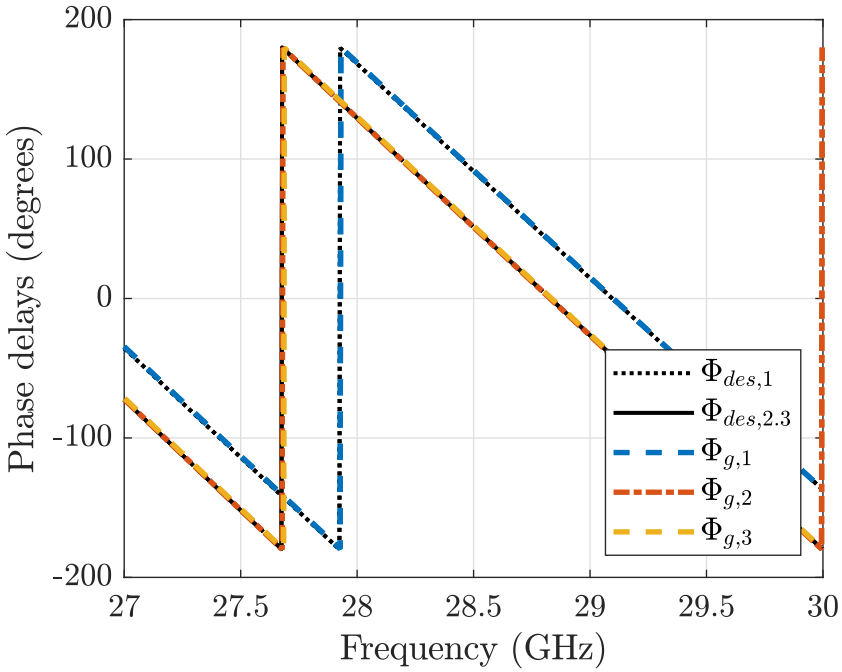

Figure 2.15 – Comparison of the phase delays of three RMWs.

In Fig. 2.16, the corresponding performances in terms of reflection coefficients are compared, demonstrating that all values remain above -60 dB across the entire bandwidth. These simulations serve indeed as an evidence of the efficiency of the tool implemented for modeling and analyzing MWs in MATLAB and CST.

The impact of reactive effects in simulation can potentially compromise the alignment between the simulated and desired phase delays in a first analysis. Specifically, as the modulation and curvatures increase, this discrepancy tends to grow. To illustrate this scenario, a simulation is presented in which the same RMW cross-section and modulation in the E-plane (as in Fig. 2.13a) are maintained. In this instance, two cases are considered: one with the modulation parameters $A_4 = 3$ and $P_4 = 10$, resulting in

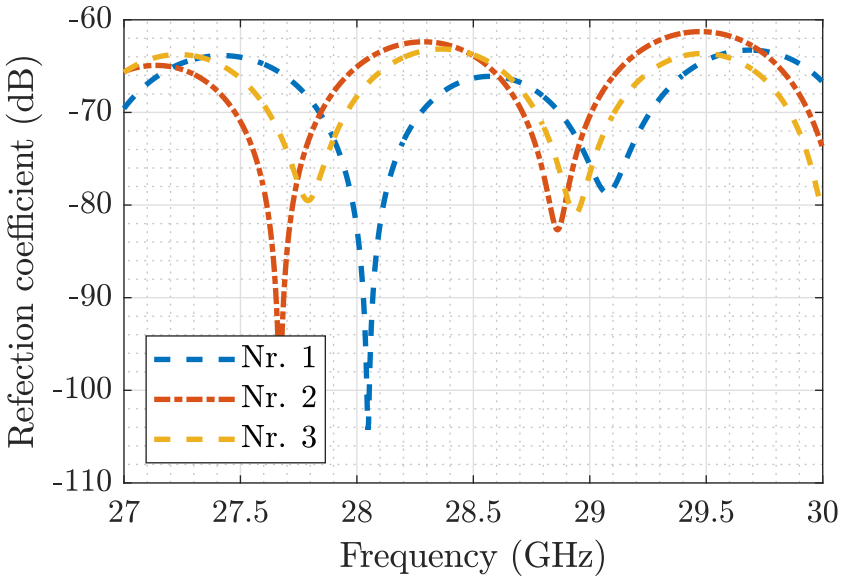

Figure 2.16 – Comparison of the reflection coefficients of three RMWs.

a centerline length of $L_4 = 115.64$ mm, and another with a more curved profile with $A_5 = 8$ and $P_5 = 10$, providing a centerline length of $L_5 = 146.54$ mm. The corresponding results, taking into account simulated phased delays and reflection coefficients, are depicted in Fig. 2.17.

As anticipated, there is a degradation in the performance for both phase and reflection when comparing case 4 with case 5, the latter exhibiting more pronounced reactive effects. The phase errors are degraded from about 2° to almost 8° and the reflection coefficients are increased to about -25 dB. For this reason, when reactive effects are identified, a fine tuning to the modulation parameters in CST is necessary to reach a perfect matching with the desired phase delays.

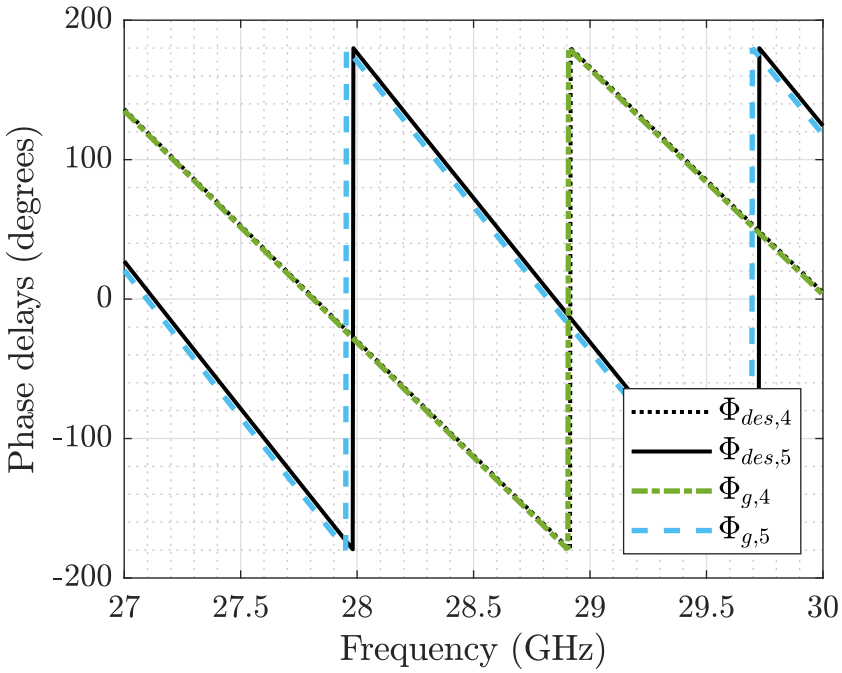

(a)

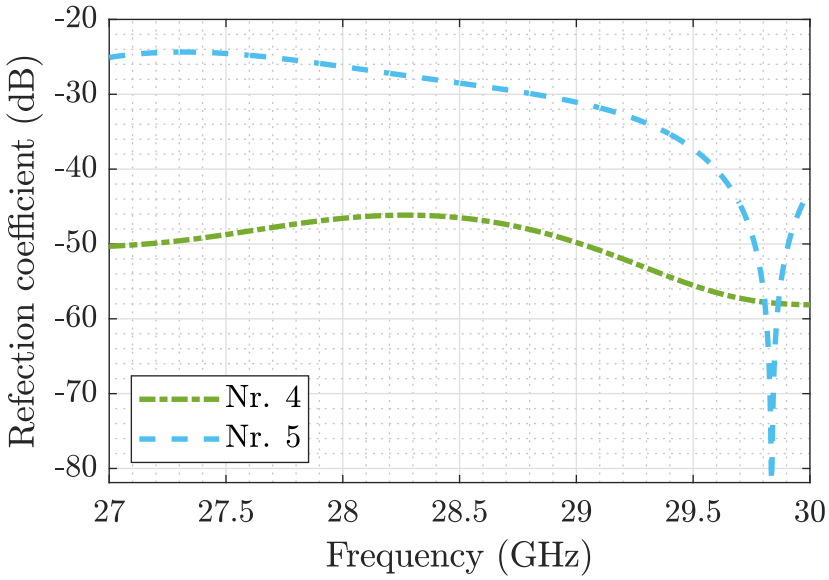

(b)

Figure 2.17 – Simulated performances of (a) phase delays and (b) reflection coefficients considering the increment of reactive effects.

2.4 Implementation of RMW cluster

As already anticipated, the implementation of a group of waveguides, named in the following cluster, permits the interconnections between different lattices providing spatial routing for a wide range of applications (e.g. array of antennas connected to amplifiers or thermal management with different periodicities between the profiles). To design a RMW cluster, one must consider additional factors to ensure the physical feasibility of the system, compared to a single RMW synthesis. This involves working with a matrix or vector of desired phase delays, denoted as Φ_{des_i}. To achieve these phase delays using a cluster of RMWs, it is necessary to optimize pairs of A_i and P_i values. Furthermore, to avoid collisions between neighboring RMWs within a given set of lattices, careful considerations of distance between profiles, modulation planes, step and modulation parameters are essential. The definition of all these parameters serves a dual purpose: ensuring the desired phase delays while also preventing collisions to accommodate them.

The first stage involves the determination of a reference centerline length, connecting two points within the front and back lattices. This reference length, denoted as W_{ref}, is a reference parameter for the entire cluster. In order to design a cluster which presents the centerline of the waveguide in the center with higher modulation than an arbitrary one more towards the edges of the cluster, the reference waveguide is derived by evaluating the step centerline (as defined in Eq. 2.6) for all the elements connecting the profiles and choosing its maximum, this will be the reference one. Consequently, the reference phase delay is defined as $\Phi_{ref} = k_g W_{ref}$, while the phase delays for other waveguides are given by $\Phi_{g_i} = \Phi_{ref} + k_g \Delta W_i$, where ΔW_i represents the additional lengths associated to modulation for the i-th waveguide, facilitating precise control over phase delays.

Subsequently, once the RMW cross-sections are established, the process of constructing the cluster in CST and synthesizing the phase delays is carried out, similarly to the procedure used for the single RMW as previously described. To note that, when dealing with a large number of RMWs within the cluster, users are advised to implement certain strategies to speed-up the full-wave simulations. These strategies may include creating symmetric clusters using planes of symmetry and simulating samples of RMWs to speed up the simulation.

2.4.1 Validation

The above presented methodology permits to build RMWs cluster employed in systems such as active full-metal arrays of antennas, discrete lenses, to name a few. In this subsection the design and validation of an iso-phase RMWs cluster (part of HummingSat flexible payload development activities [14]) is described showing the correspondent simulation performances as an example. This system is designed to operate in the [17.7-20.2] GHz range with central frequency $f_0 = 18.95$ GHz. The cluster should connect a matrix of amplifiers presenting a periodicity of about $3\lambda_0$ and an antenna array with $1.5\lambda_0$ periodicity and a triangular lattice, as showed in Fig. 2.18.

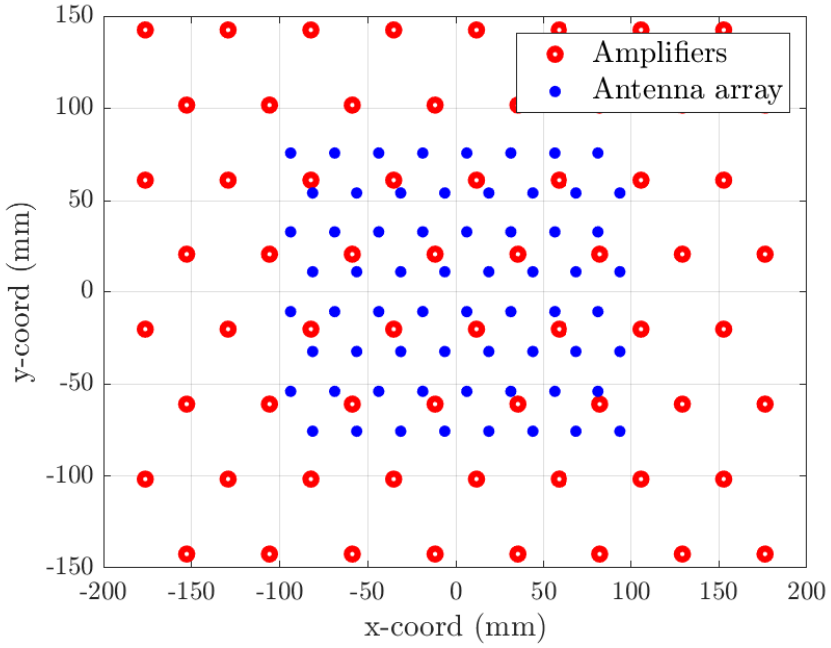

Figure 2.18 – Front and back array to be connected (red: amplifiers; blue: antenna array elements).

The distance between the profiles (Δ_z) is defined to be $7\lambda_0$, in order to avoid high curvatures and overlappings between waveguides. The parameters defining the step function are maintained the same as the previous example, while the following parameters defining the dual-ridges cross-section are defined as following: $w_x = 4$ mm, $w_y = 9$ mm, $h_x = 1.2$ mm, $h_y = 4$ mm, $r_t = 0$ mm, $r_b = 0$ mm, $r_c = 0$ mm and $t = 0.25$ mm. The selection of these dimensions aims to achieve optimal linearity within the specified working frequency range, as illustrated in Fig. 2.19.

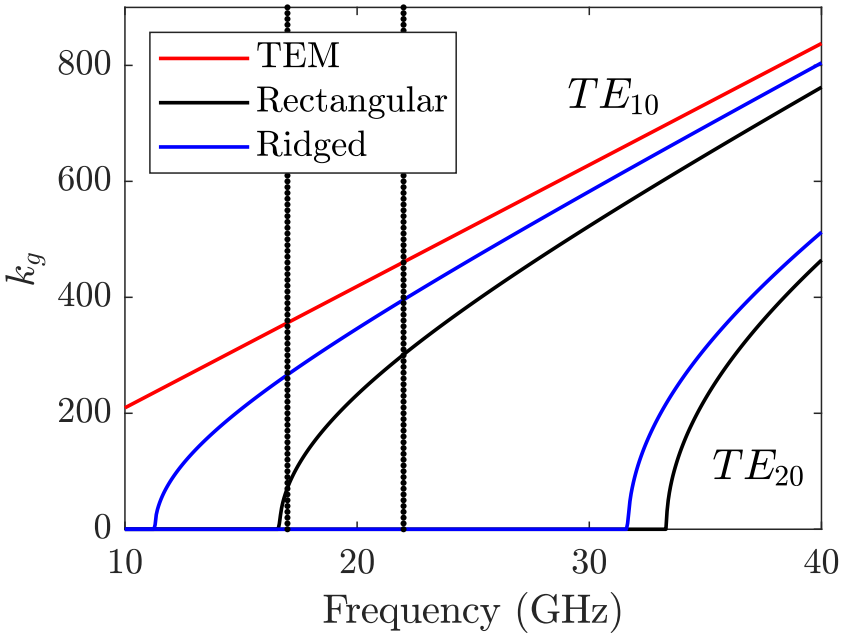

Figure 2.19 – Dispersion curves of rectangular and dual-ridged waveguides for the two first propagating modes (TE_{10}, TE_{20}) in the working frequency bandwidth (black lines).

The RMW cluster connecting the two defined arrays is built in CST, as showed in Fig. 2.20. In Fig. 2.20b, a set of representative waveguides highlighted in red have their corresponding design parameters listed in Tab. 2.1.

WG nr.	**57**	**60**	**44**	**36**	**35**	**33**
A	0	20.4	23	24.5	23.7	17.8
P	0	4	4	4	4	4

Table 2.1 – Modulation parameters A and P of the 6 RMWs among the iso-phase cluster.

It should be observed that waveguide nr. 57, located on the top left corner of the cluster in Fig. 2.20b, is the reference waveguide. As a matter of fact, this waveguide is characterized by a step function and a modulation is applied to it to design the other waveguides. As one moves closer to the center, specifically waveguide nr. 36, the modulation increases. This increased modulation is required to compensate for the smaller physical distance in the center compared to the corners, in order to maintain a constant phase delay, as already discussed. Figure 2.21 presents the full-wave simulations of the selected waveguides (in red in Fig. 2.20b) within the RMW cluster.

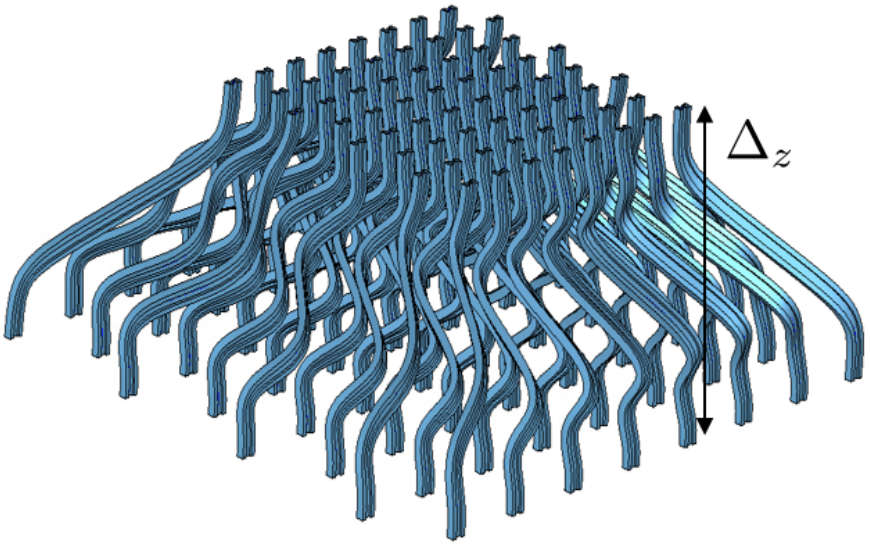

(a)

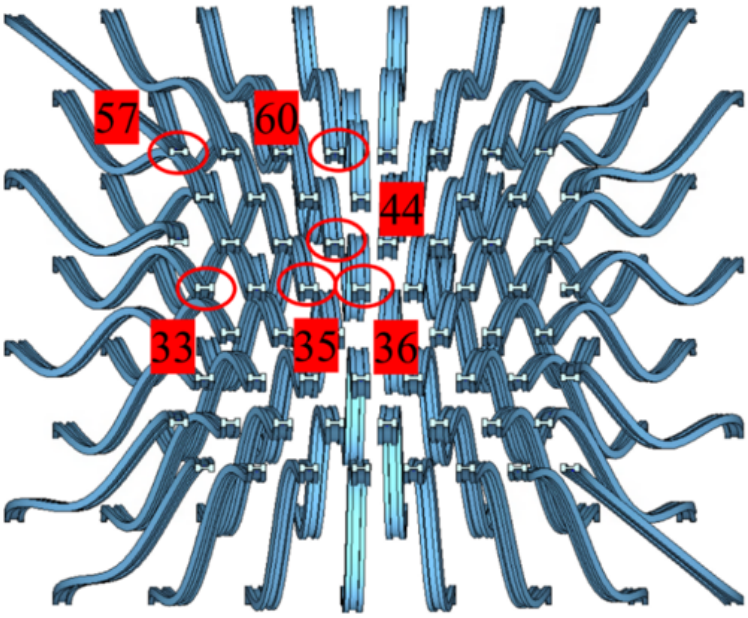

(b)

Figure 2.20 – (a) Perspective view of air-volume of RMW isophase cluster from CST. (b) Front view of air-volume of RMW isophase cluster from CST with the selected waveguides for simulation in red.

As it can be seen, the simulated reflection coefficients are always below -30 dB as well as the phase delays are almost overlapped with a phase error above 3° as expected. The simulated insertion losses (using conductivity of $2.5\text{x}10^7$ S/m, typical from plated AM

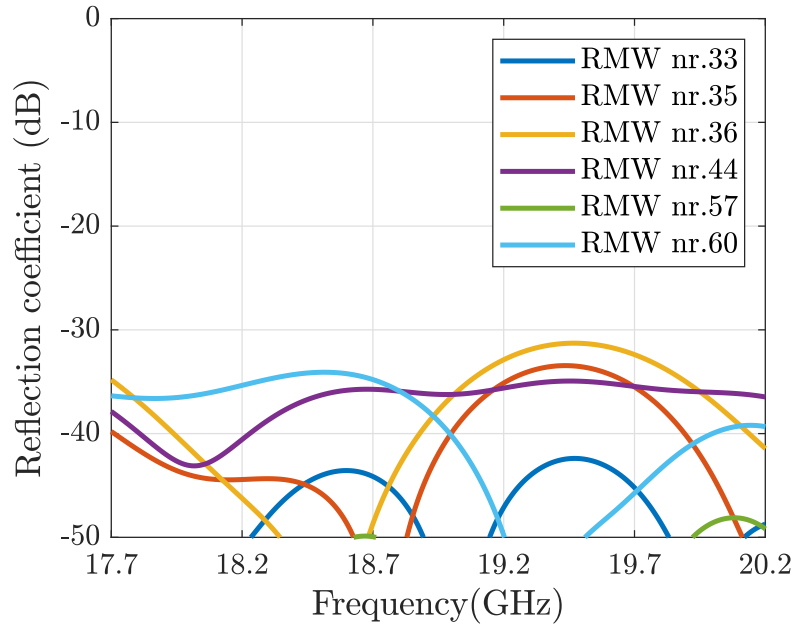

(a)

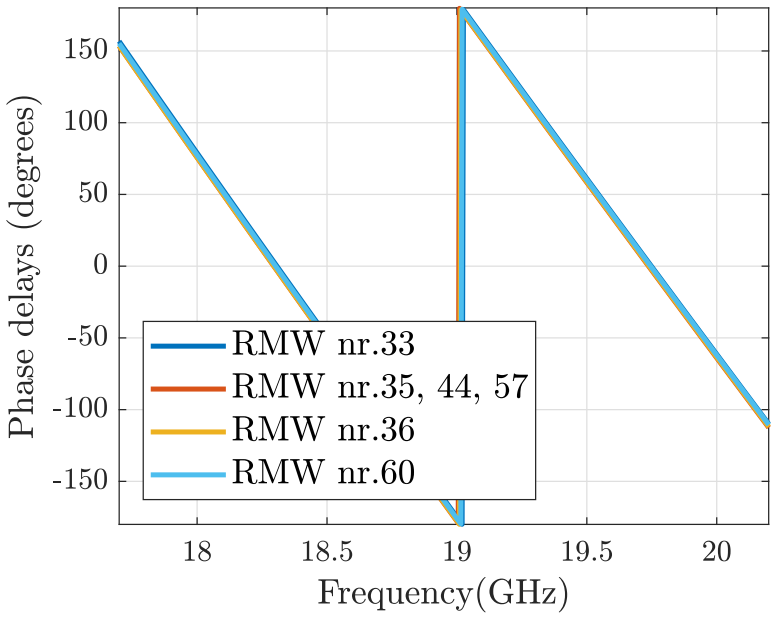

(b)

Figure 2.21 – Simulated results of six RMWs selected in the cluster. (a) Reflection coefficients. (b) Phase delays.

process) are about -0.18 dB. One very interesting feature is the robustness in bandwidth,

which is enabled by the presence of the dual-ridges. In fact, the ridges lower the cut-off frequency of the waveguide, which allows for operation in a range of frequencies where the dispersion is low but without entering in the region where higher-order modes appear.

2.5 Conclusion

To conclude, RMWs enable the synthesis of arbitrary phase delays while maintaining high flexibility in routing signals within a 3D space. This flexibility is achieved by tailoring their curvature through a modulation function along the direction of propagation.

Within this chapter, a comprehensive analytic approach for building and controlling phase delays using RMWs has been developed and detailed. This approach involves characterizing the trajectory of the waveguide between two arbitrary points, defining the modulation function and customizing their cross-section along the path to attain the desired phase delays. Several examples have been presented to demonstrate the remarkable performances of such components. In addition, a section is dedicated to the synthesis of phase delays in meandered waveguides. This section illustrates the main principles concerning potential reactive effects that can impact the simulated response and the main guidelines to avoid them. Furthermore, the chapter concludes by describing the design of a cluster of RMWs that could be employed in the conception of very low loss antenna arryas. This final section introduces the subsequent chapter, which propose the practical implementation of RMWs clusters to precisely control phase delays, facilitating the focusing within 3D discrete lenses.

CHAPTER 3

Design of 3D discrete lenses for narrow field of view scenarios

3.1 Introduction

Nowadays, space applications employing antennas with a restricted FoV are mainly found in GEO satellites. Indeed, GEO payloads are positioned at considerable distances from Earth (nearly 36000 kilometers), resulting in narrower FoV when compared to those of MEO or LEO satellites, as illustrated in Fig. 3.1.

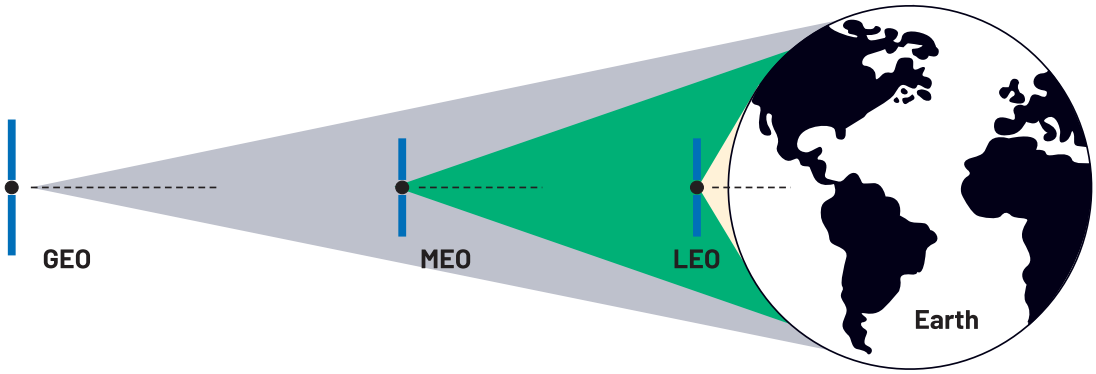

Figure 3.1 – Earth coverages from GEO, MEO, and LEO satellites (from [169]).

Given their considerable distance from Earth, these radiating systems need to maximize the power transfer in order to face the growing demand for communication capac-

ity and speed in modern communications [1], [2]. To address this challenges, various solutions are being investigated.

Significant efforts are being devoted these days to the development of full-metal directive radiators. This has been mainly boosted by the innovation of the patents related to 3D printing techniques [134], [135]. The development of full-metal 3D printing techniques [26] permits to face the needs of maximization of power transfer, reducing losses, while lowering at the same time their volume and complexity. Literature offers numerous solutions where efforts have been made to enhance the efficiency of GEO platforms with restricted FoV. These efforts include high-efficiency horns in both direct radiating phased arrays and reflector-based systems, as demonstrated in [170]–[172].

In situations where a restricted FoV is essential, the implementation of 3D discrete lenses [122] through full-metal AM offers an extremely valuable solution. By adjusting their magnification factor to values smaller than one, it is possible to decrease the overall size and weight of the system. This adjustment allows for scanning within narrow angles while avoiding the unwanted presence of grating lobes (GLs), effectively turning this concept into a practical reality. Additionally, employing cluster of RMWs for connecting the two radiating arrays offers the potential to achieve valuable results in terms of power, flexibility, large frequency bandwidth and dual polarization capabilities. For this reason, the main goal of this chapter is focused on the conception and manufacturing of innovative RMW-based full-metal 3D discrete lenses for GEO scenarios characterized by narrow FoV.

This chapter is organized as following: first, the 3D discrete lens architecture for narrow FoV scanning scenario is described in all its choices. Once, the main specifications and common variables to define the design of the 3D discrete lens are assigned, a first 7×7 lens is proposed, designed and analyzed through full-wave simulations. While at the end, a smaller 3×3 prototype is fabricated through AM technology and measured, in order to validate the innovative proposed solution.

3.2 Lens architecture

In this section, the main features of a 3D discrete lens for narrow FoV scanning scenarios are described. Firstly, the choices on the magnification factor and the sizes for both front and back arrays, are presented. Some considerations on the array periodicities in order to mitigate GLs within the specified FoV are also introduced. Subsequently,

the analysis of focal points and the DoFs are taken into account to guarantee perfect lens focalization. Finally, the array profiles coordinates defining the chosen 3D discrete lens are determined.

3.2.1 Field of view, magnification factor and array periodicities

To attain the narrow FoV in GEO satellites, the choice of a 3D discrete lens with magnification factor smaller than one is the most suitable solution. It should be noted that the application scenario can be also extended to on-ground gateways antennas where the limited FoV and high power handling are still the main objectives.

As already introduced in Section 1.3.4, a magnification factor smaller than one ($M < 1$) permits to reduce the output angle compared to the input one ($\theta_{out,k} < \theta_{in,k}$) from the generic feed F_k, as depicted in Fig. 3.2. A substantial reduction of the overall weight and volume can be reached for these systems, being the back array (in red) M times smaller than the front one (in blue).

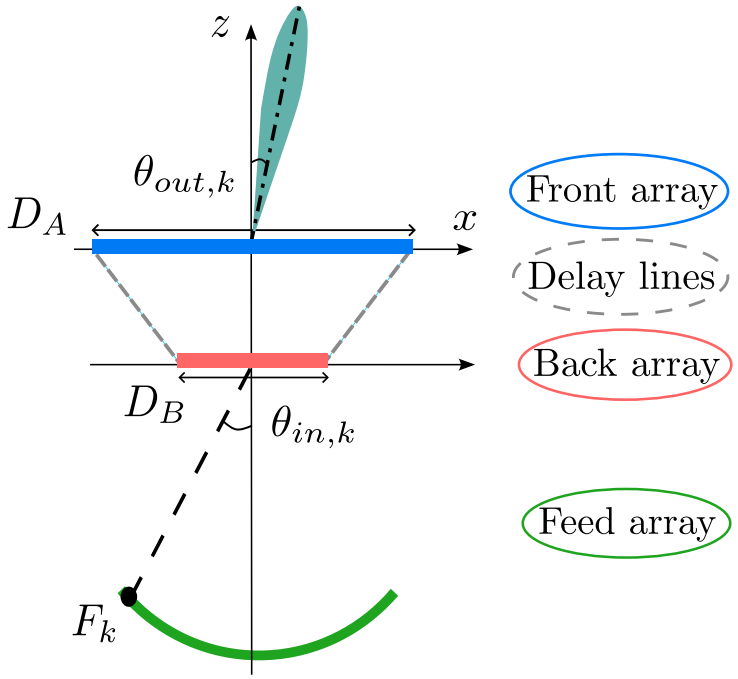

Figure 3.2 – Representation of a 3D discrete lens employing flat front and back arrays with $M < 1$ in the xOz-plane.

GEO antennas possess a restricted FoV spanning approximately between $\pm 8.7°$. This means that the presence of GLs at angles falling outside of this specific range

should be considered acceptable [173]. This affirmation is particularly valid for antennas working in Rx [173]. However, when dealing with Tx antennas, careful considerations regarding GLs are necessary to avoid unnecessary power waste. For this reason, Rx antenna are examined in this chapter.

For the design of the 3D discrete lens antenna for GEO scenario, a maximum output angle of $\theta_{out}^{max} = 8°$ is considered as practical case. By setting the magnification factor to $M = 0.5$, the corresponding input angle can be expanded to $\theta_{in}^{max} = 16.2°$ (computed from $\sin(\theta_{in}^{max}) = \sin(\theta_{out}^{max})/M$) [122]). Notably, accommodating the feed array becomes in this case more convenient when considering the expansion of the input angles, in contrast to the scenario for $M = 1$ where the input angles are equal to the output ones.

Achieving the desired output FoV necessitates specific periodicity for the front array, as detailed in [174] for phased arrays. In this context, to avoid GLs in the FoV, the typical front array periodicity typically falls within the range of $[2.3-3]\lambda_0$, calculated at the central frequency to reach the defined FoV of $\pm 8°$, as referenced in [171], [173]. The periodicity of the back array, which is connected to the front array by the magnification factor $M = 0.5$, is almost half of the value selected for the latter. A more comprehensive examination of these selected array geometries and their defining parameters are provided in upcoming sections.

3.2.2 Array profiles and focal points

An overview on the choice of the front and back array profiles and the number of focal points is presented here. As previously discussed in Section 1.3.3, the choices made regarding these arrays enable the direct definition of the number of focal points of the lens system.

This chapter proposes to implement a lens with flat front and back arrays, in order to facilitate the AM manufacturing process. The number of focal points is evaluated in the following, recalling Section 1.3.3. From seven variables ($X_{A_i}, Y_{A_i}, Z_{A_i}$ for the front array; $X_{B_i}, Y_{B_i}, Z_{B_i}$ for the back array and W_i for the delay lines length) defining a 3D discrete lens, two (either X_{A_i}, Y_{A_i} front or X_{B_i}, Y_{B_i} back) are apriori fixed to be independent. Two more variables are also fixed for this case to guarantee the corresponding flat profiles, respectively $Z_{A_i} = 0$ and $Z_{B_i} = -\Delta_z$, as shown in Fig. 3.3.

For this reason, the remaining variables are 3 ($7-4 = 3$ DoFs), corresponding to the number of focal points guaranteeing zero phase aberrations. These three focal points, denoted as F_1, F_2, and F_3, are strategically positioned in a circular arrangement per-

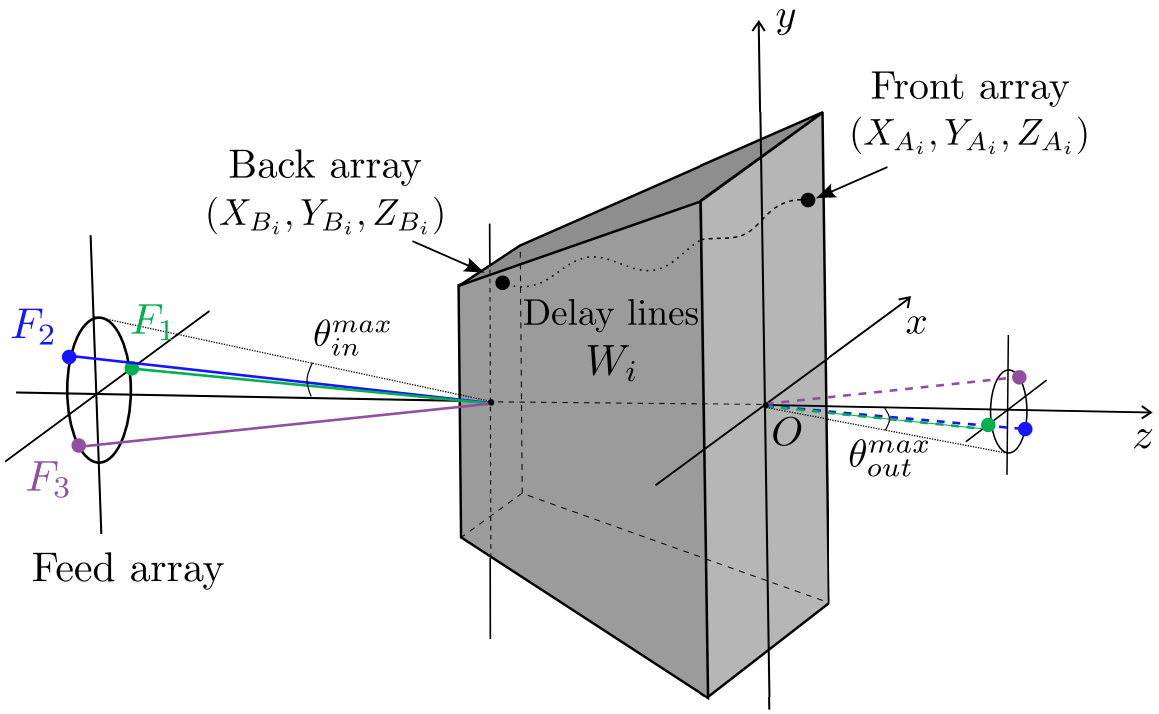

Figure 3.3 – Sketch of a 3D discrete lens with flat front and back arrays ($Z_{A_i} = 0$ and $Z_{B_i} = -\Delta_z$). The considered configuration has three focal points (F_1, F_2, F_3) and implements a zooming factor $M < 1$. The grey box represents the core of the 3D lens, where the phase delay lines of length W_i between the front and back arrays are implemented.

pendicular to the lens axis. Their azimuth angles are designated as $\phi_{in} = [0, 120, 240]°$, while sharing a common elevation angle. The latter is assigned from specifications ($\theta_{out}^{max} = 8°$), which together with the chosen magnification factor $M = 0.5$ gives the input angle $\theta_{in}^{max} = 16.2°$. While concerning the coordinates of both arrays and delay line lengths, a detailed examination and description of the GO equations is presented in the subsequent part.

3.2.3 Arrays coordinates and delay lines length

The coordinates of both arrays and delay line lengths are obtained here, solving the GO equations for the 3 focal points depicted in Fig. 3.3. The focalization problem is defined by a set of 3 equations with 3 variables that need to be solved. The general Eq. 1.2 introduced in Section 1.3.3 can be written for each focal point as:

$$\begin{cases} k_0|\overrightarrow{F_1B_i}| + k_gW_i + k_0|\overrightarrow{A_iP_{i,1}}| = \text{constant}_1 \\ k_0|\overrightarrow{F_2B_i}| + k_gW_i + k_0|\overrightarrow{A_iP_{i,2}}| = \text{constant}_2 \\ k_0|\overrightarrow{F_3B_i}| + k_gW_i + k_0|\overrightarrow{A_iP_{i,3}}| = \text{constant}_3 \end{cases} \tag{3.1}$$

being $\overrightarrow{OA}_i = [X_{A_i}, Y_{A_i}, Z_{A_i}]$ and $\overrightarrow{O'B}_i = [X_{B_i}, Y_{B_i}, Z_{B_i}]$, the coordinates of the i-th element of the front and back arrays and W_i is the length of the delay lines connecting them. At this stage, to solve the GO system of Eq. 3.1, one of the two array should be fixed to be independent. Two different methods can be employed to solve the problem. One approach uses the coordinates X_{A_i} and Y_{A_i} of the front array A_i, as the independent variables, while the other method employs the coordinates X_{B_i} and Y_{B_i} of the back array B_i, as the independent ones.

In this chapter, the coordinates of the back array are considered as independent variables. This decision is primarily motivated by the relatively smaller size of the back array because $M < 1$ (as previously discussed, the back array periodicity is smaller than that of the front one), which imposes more limitations in terms of accommodating the antenna elements. It is important to note that this chapter does not explore the problem when the coordinates of the front array are treated as independent variables. For a detailed exploration of that approach, the correspondent expression can be found in [122] on page 9.

Therefore by assigning the following coordinates (X_{B_i}, Y_{B_i}, $Z_{B_i} = 0$ and $Z_{A_i} = -\Delta_z$), the transverse coordinates of the front array (X_{A_i}, Y_{A_i}) and the delay lines lengths W_i are derived from Eq. 3.1 as following:

$$\begin{aligned} X_{A_i} = \Big[& 1/3\sqrt{X_{B_i}^2 + X_{B_i}\sin(\theta_{in}^{max})F + Y_{B_i}^2 + F^2 - \sqrt{3}Y_{B_i}\sin(\theta_{in}^{max})F} \\ & -2/3\sqrt{X_{B_i}^2 + 2X_{B_i}\sin(\theta_{in}^{max})F + Y_{B_i}^2 + F^2} \\ & +1/3\sqrt{X_{B_i}^2 + X_{B_i}\sin(\theta_{in}^{max})F + Y_{B_i}^2 + F^2 + \sqrt{3}Y_{B_i}\sin(\theta_{in}^{max})F}\Big] \\ & /(M\sin(\theta_{in}^{max}))) \end{aligned} \tag{3.2}$$

$$\begin{aligned} Y_{A_i} = \Big[& \sqrt{3}/3\sqrt{X_{B_i}^2 + X_{B_i}\sin(\theta_{in}^{max})F + Y_{B_i}^2 + F^2 + \sqrt{3}Y_{B_i}\sin(\theta_{in}^{max})F} \\ & -\sqrt{3}/3\sqrt{X_{B_i}^2 + X_{B_i}\sin(\theta_{in}^{max})F + Y_{B_i}^2 + F^2 - \sqrt{3}Y_{B_i}\sin(\theta_{in}^{max})F}\Big] \\ & /(M\sin(\theta_{in}^{max}))) \end{aligned} \tag{3.3}$$

$$
\begin{aligned}
W_i = F - 1/3\sqrt{X_{B_i}^2 - 2X_{B_i}\sin(\theta_{in}^{max})F + Y_{B_i}^2 + F^2} \\
-1/3\sqrt{X_{B_i}^2 + X_{B_i}\sin(\theta_{in}^{max})F + Y_{B_i}^2 + F^2 - \sqrt{3}Y_{B_i}\sin(\theta_{in}^{max})F} \\
-1/3\sqrt{X_{B_i}^2 + X_{B_i}\sin(\theta_{in}^{max})F + Y_{B_i}^2 + F^2 + \sqrt{3}Y_{B_i}\sin(\theta_{in}^{max})F}
\end{aligned}
\tag{3.4}
$$

The definition of such variables permit to obtain zero phase aberrations when considering the 3 focal points in (θ_{in}^{max}, ϕ_{in}) with a magnification factor M. Through the presented formulation, when the back array is characterized by a periodic lattice, the corresponding front one is not periodic (see Eq. 3.2 and Eq. 3.3). Same considerations are applied to the back array when considering the front one the assigned periodic one.

The selection of the focal distance (through the definition of the focal ratio F/D_B) is another crucial point when determining the characteristics of the front array. This ratio can significantly impact the positions of the front array elements, as outlined in Eq. 3.2 and Eq. 3.3. In the design of this lens, a ratio of approximately $F/D_B = 2$ has been chosen in order to obtain a more periodic distribution of the front array. After having established all the parameters for each constitutive element of the 3D discrete lens, the subsequent phase involves sizing the lens system and verifying its performance through simulations and measurements, as detailed further.

3.3 Design of a 7 x 7 discrete lens

In this section, the full-design of a 3D discrete lens in waveguide technology for GEO satellite scenarios is presented. The section is structured as follows: firstly, the lens geometry is defined in terms of its variables to fit with the desired specifications, including a detailed explanation of the RMW cluster used to connect the front and back arrays. Subsequently, the complete implementation of the waveguide lens in CST is described in all its parts. To conclude, some validation results are presented, obtained through a comparison of the simulations with the radiation pattern computed using MATLAB.

3.3.1 Lens geometry

For this application example, a Ka-band Rx antenna is selected, whose center frequency is $f_0 = 28.5$ GHz. The reason is mainly related to the fabrication of the entire system, which is more compact at higher frequencies in Rx than in Tx. Additionally, this

choice aligns with the considerations discussed in the last section, taking into account the power wasted outside the FoV considering a Tx antenna.

The chosen lens presents flat front and back arrays with 3 focal points following a magnification factor of $M = 0.5$ to reach scanning within a FoV of $\pm 8°$. Despite a final antenna would have a larger number of radiating elements to fit the requirements of power, this first example is restricted to $N_e = 49$ elements (7×7 elements per side of the lens with squared periodic lattice over the back array) in order to reduce the computational effort of the full-wave simulations. The transversal cross-sections of the front and back arrays of the considered 7×7 lens are presented in Fig. 3.4 showing the 3 focal points defined in the previous section.

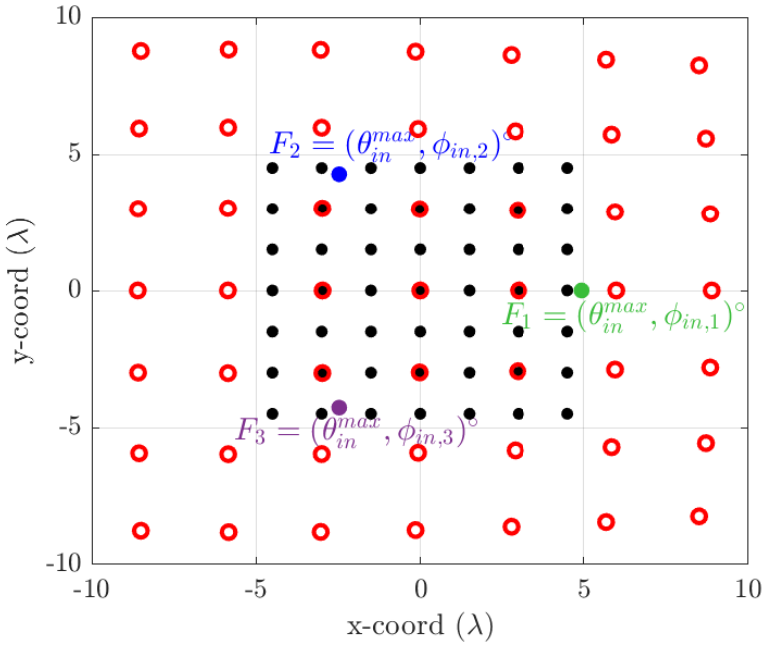

Figure 3.4 – 2D projection of 7×7 square 3D discrete lens antenna with assigned back array (black dots), front array (red circles) and 3 focal points F_1, F_2 and F_3 characterized by the common elevation plane $\theta_{in}^{max} = 16.2°$ in the azimuth planes $\phi_{in} = [0, 120, 240]°$ (with $M = 0.5$ and $F/D_B = 2$).

The assigned back array with periodicity $d_B = 1.5\lambda_0$ is characterized by black dots, while the front one by red circles with a distance between elements that is approximately $d_A \sim 2.8\lambda_0$. It can be noticed again that the elements in the back array follow a regular squared lattice because this one is the independent array that is a priori fixed, whereas the elements in the front array are distributed in an irregular lattice. Moreover,

the 3 focal points are also shown in their elevation and azimuth components, being distributed with equi-angular azimuth distance of $\Delta\phi_{in} = 120°$ and the common elevation $\theta_{in}^{max} = 16.2°$. In this configuration a symmetry with respect to the yOz-plane can be noticed, that will be useful for the further design of the full-metal lens.

3.3.2 Synthesis of RMW cluster

It is necessary to establish a connection between the front and back arrays to enable the generation of the desired phase delays, essential for achieving the desired lens focalization. For this reason, the concept introduced in Section 2.4 for the RMW cluster design is applied here. In particular, a dual channel RMWs option is considered to support both wide frequency bandwidths and dual polarization features.

For this example case, the adopted design choices are related to E-plane modulated waveguides (with the correspondent parameters $\delta = 0, \gamma = 1$ in Eq. 2.7 in Section 2.2.2) and a RMW cluster height of $\Delta_z = 13\lambda_0$ (136.84 mm at 28.5 GHz), to assure smooth trajectories between the two connected arrays. As already anticipated in Section 2.2.1, to avoid discontinuities at the connection points and sharp slopes using the step function, the inflection point is fixed in the center $t_0 = 0.5$ while for inclination parameters is $\beta w = 11$ with $\beta = 22$ and $w = 0.5$.

In order to design the lens antenna, a RMW cluster that produces the phase delays Φ_{wg_i} that are as close as possible to the desired ones $\Phi_{des_i} = k_g W_i$ is derived from the delay line length of Eq. 3.4. The optimized RMW cluster of curved centerlines providing the desired phase delays is displayed in Fig. 3.5.

The optimized amplitudes A_i and semi-periods P_i to produce the required phase delays through the RMW cluster are presented in Tab. 3.1 and Tab. 3.2 respectively.

0.00	11.31	10.38	10.18	10.02	9.32	4.30
−8.54	11.06	12.59	12.85	12.99	11.16	−8.54
10.62	13.28	13.98	13.68	13.51	13.07	10.12
11.83	14.05	14.54	14.56	14.16	12.02	9.21
10.62	13.28	13.98	13.68	13.51	13.07	10.12
−8.54	11.06	12.59	12.85	12.99	11.16	−8.54
0.00	11.31	10.38	10.18	10.02	9.32	4.30

Table 3.1 – Matrix of amplitude parameters A_i for the 7×7 RMWs cluster.

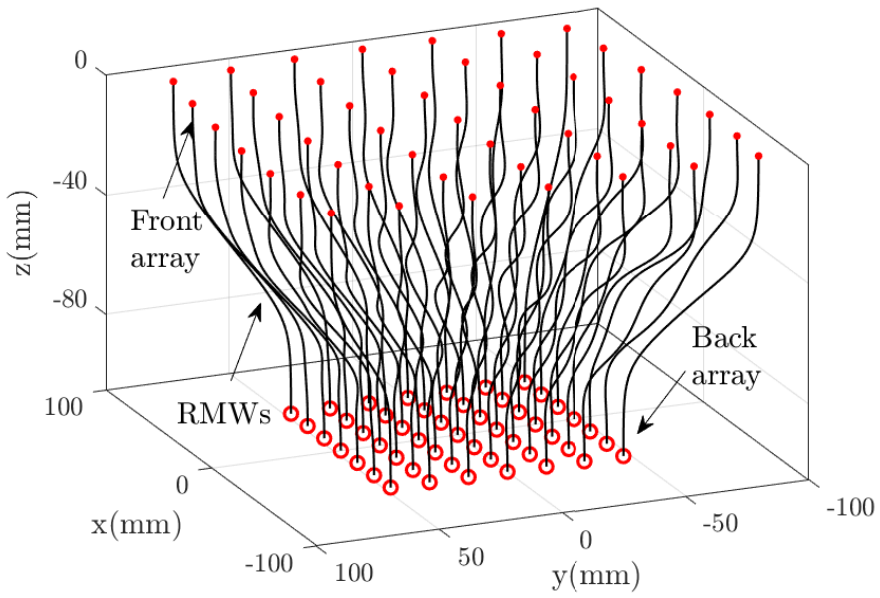

Figure 3.5 – Cluster of RMW trajectories (black curves with curvature for each element) connecting back (red circles) and front arrays (red dots) with $\Delta_z = 13\lambda_0$.

0.00	3.90	5.00	5.52	5.40	4.94	3.90
−5.46	5.62	5.29	5.57	5.32	5.51	−5.38
5.71	5.38	5.61	5.87	5.73	5.38	5.52
5.30	5.30	5.60	5.70	5.66	6.01	6.30
5.71	5.38	5.61	5.87	5.73	5.38	5.52
−5.46	5.62	5.29	5.57	5.32	5.51	−5.38
0.00	3.90	5.00	5.52	5.40	4.94	3.90

Table 3.2 – Matrix of semi-periods parameters P_i for the 7×7 RMWs cluster.

In this case, a symmetry respect to the yOz-plane is taken into account in this case, with the aim of speeding up the optimization of variables (A_i, P_i). Specifically, in the context of the RMW cluster building, half of the variables are optimized.

As explained in the section dedicated to RMW cluster design in Section 2.4, the reference centerline corresponds to the simple step function without any modulation, wherein both A_{ref} and P_{ref} are set to zero. In this particular scenario, the reference element is characterized by a centerline length of $W_{ref} = 159.03$ mm and is positioned at one of the vertices of the array.

3.3.3 CST model

The corresponding CST model of the 7×7 discrete lens in waveguide technology is depicted in Fig. 3.6. It consists on the following parts:

- the front array, which is formed by 7×7 square horns (each horn is backed by a septum polarizer and connected to a pair of RMWs);
- the cluster of dual channel RMWs, which connects the back array to the front one and supports dual polarization;
- the back array, which is formed by 7×7 square horns (each horn is backed by a septum polarizer and connected to a pair of RMWs);
- the feed array with dual circular polarized horns, where each one is backed by a septum polarizer to produce the circular polarization.

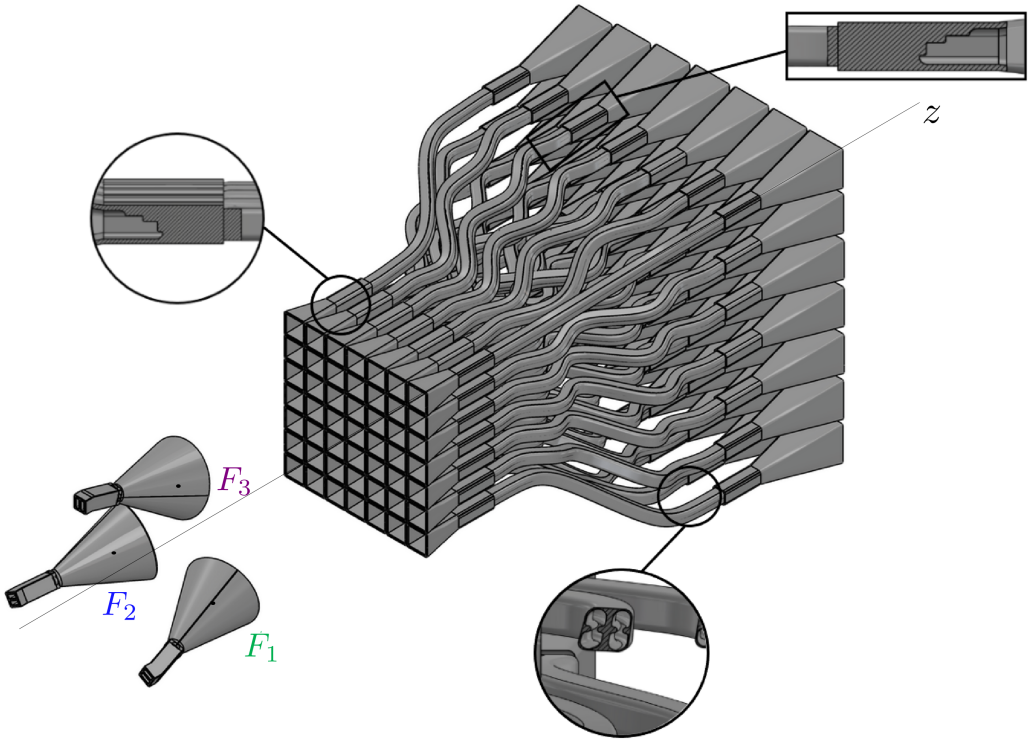

Figure 3.6 – 7×7 CST model of the 3D discrete lens antenna design with $M = 0.5$ including the RMW cluster with 3 feeds placed in the focal points characterized by $\theta_{in}^{max} = 16.2°$ and $\phi_{in} = [0, 120, 240]°$.

Each element in the lens has two side-by-side RMWs, one per polarization. Indeed, in real Rx operation, a signal is received by all the horns in the front array, each one

receiving a portion of the complete circularly polarized signal. The signals received by each front-side horn is transformed from circular to linear by the septum polarizer and, depending on the polarization, they travel through the right-handed or through the left-handed RMW channels. After the RMWs, the septum polarizers in the back-side horns transforms again the linear polarization into a circular one. The signals then travel through the free-space between the back array and the feed array, where circularly-polarized feeds connected to rest of the payload finally receive the signal. Dual polarization can be perfectly supported by this type of lenses.

The dimensions of the front and back horns are established based on considerations detailed in the previous section. The back array horns present an edge length of $1.5\lambda_0$, while the front horns are designed with a $2.5\lambda_0$ edge length to accommodate the non-periodic array configuration. Both front and back array horns incorporate a 1 mm wall thickness. It must be highlighted that the front array horns do not fully fill the available space, but the selected size permits to have horns that have some space in between, required later for assembly using a screwdriver. The simulated patterns of the horns are displayed in Fig. 3.7 presenting respectively a peak directivity of 17.45 dBi and 11.5 dBi for the front and back horns.

The feed horns are placed in the focal points and are optimized to provide a peak directivity of about 20 dBi, as illustrated in Fig. 3.8. The size of such horns $(4.2\lambda_0)$ is chosen to provide an edge-tapering illumination of about -10 dB in the back array respect to the center value, considering a focal ratio of $F/D_B = 2$, as analyzed in [175]. Nevertheless, the user has the flexibility to replace the feed horn to achieve the desired performances.

3.3.4 Validation

This subsection presents the numerical results of the 7×7 discrete lens antenna displayed in Fig. 3.6. The antenna system is analyzed using the routine implemented in MATLAB and described in Eq. 1.4 in Section 1.3.5 to compute the radiation pattern. In addition, the full-wave simulations are provided using CST for a comparison.

The initial MATLAB analysis focuses on the preliminary validation of the pointing direction by considering the phase distribution along the lens system and incorporating the element factor of the front array. At this stage and as an initial approximation, the back horn patterns and the feed horn one are omitted in the lens radiation pattern evaluation. But taking them into account to include a more realistic amplitude apodization

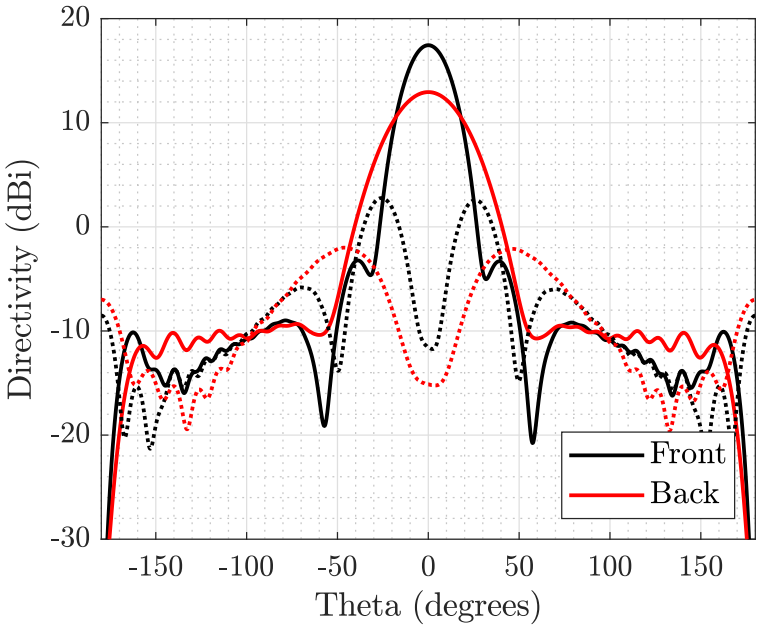

Figure 3.7 – Co-polar (solid lines) and cross-polar (dotted lines) directivity patterns in $\phi = 0°$ of the front (in black) and back (in red) horns backed by the septum polarizer optimized in CST at $f_0 = 28.5$ GHz.

is identified as a further improvement to perform a more precise approximation. The phase tapering of the lens consider the free-space distances between the k-th feed and the i-th elements in the back array ($\angle a_{i,k} = -k_0|\overrightarrow{F_k B_i}|$) and the delay line lengths obtained from Eq. 3.4 considering the waveguide propagation constant k_g. While, the exponential used to model the cosine pattern of the front element (i.e. $\cos^{q_A}(\theta)$) is defined as $q_A = 13.2$ to reproduce the corresponding directivity of 17.5 dBi. The normalized patterns computed with MATLAB considering the feed placed in the three focal points are displayed in Fig. 3.9 with respect to the conventional uv-coordinates ($u = \sin\theta\cos(\phi)$ and $v = \sin\theta\sin(\phi)$).

As expected, the three beams point at $\theta_{out}^{max} = 8°$ and the three azimuthal angles correspond with the ones coming from the focal points (respectively $\phi_{out} = [180, 300, 60]°$ for F_1, F_2, F_3). The GLs are outside of the FoV (defined by the red circle in Fig. 3.9), as required from the specifications.

For the sake of completeness, Fig. 3.10 and Fig. 3.11 show some numerical results obtained comparing MATLAB and CST. It is important to note that in the figures, the cross-polar patterns in MATLAB are not showed, since a scalar analysis has been im-

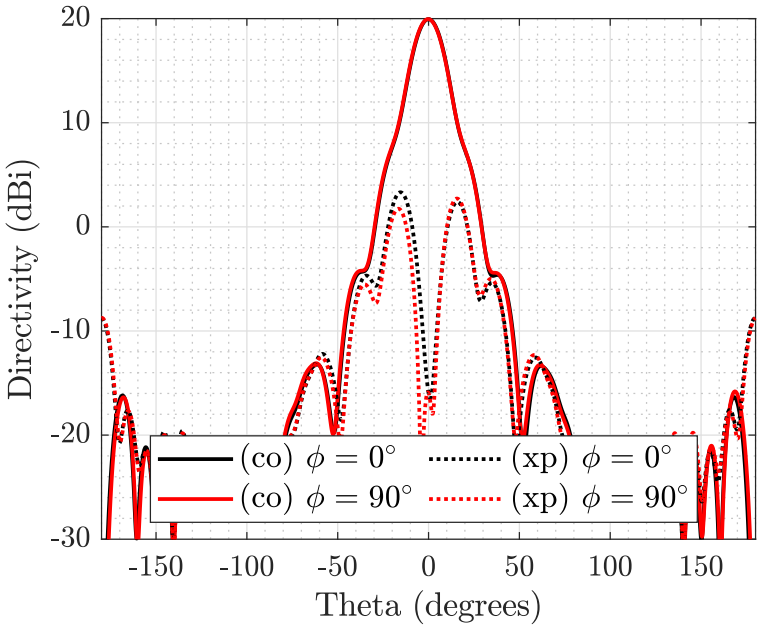

Figure 3.8 – Co-polar (solid lines) and cross-polar (dotted lines) directivity patterns in $\phi = [0, 90]°$ of the feed horns backed by the septum polarizer optimized in CST at $f_0 = 28.5$ GHz.

plemented, as presented in Eq. 1.4 in Section 1.3.5. The extension to a vectorial analysis is proposed as a follow on at the end of the thesis.

Figure 3.10 illustrates the feed placed in one focal point F_1 characterized by the elevation and azimuth angles $\theta_{in}^{max} = 16.2°$ and $\phi_{in} = 0°$. The resulting beam is pointing at $\theta_{out}^{max} = 8°$ and $\phi_{out} = 180°$, as expected. Both analysis methods exhibit strong agreement in terms of the pointing angle, validating the analyses conducted using both MATLAB and CST simulations. The simulated XPD is maintained above 17 dB in the main beam.

Another case of validation is illustrated in Fig. 3.11, exciting a feed placed in the center of the lens axis (i.e. $\theta_{in} = 0°$). The results displayed highlight a good agreement though the co-polar patterns of MATLAB and CST analysis, maintaining the XPD in the main beam in broadside above 23 dB. The beams at $\pm 20°$ represent the GLs maintained outside the FoV, as desired from specifications. The differences in side-lobe levels between the CST and MATLAB results can be mainly attributed to the amplitude tapering in the back lens which is not considered for the GO pattern in MATLAB (back horn and feed patterns are omitted). This aspect, representing a significant advancement is explored in the next chapter.

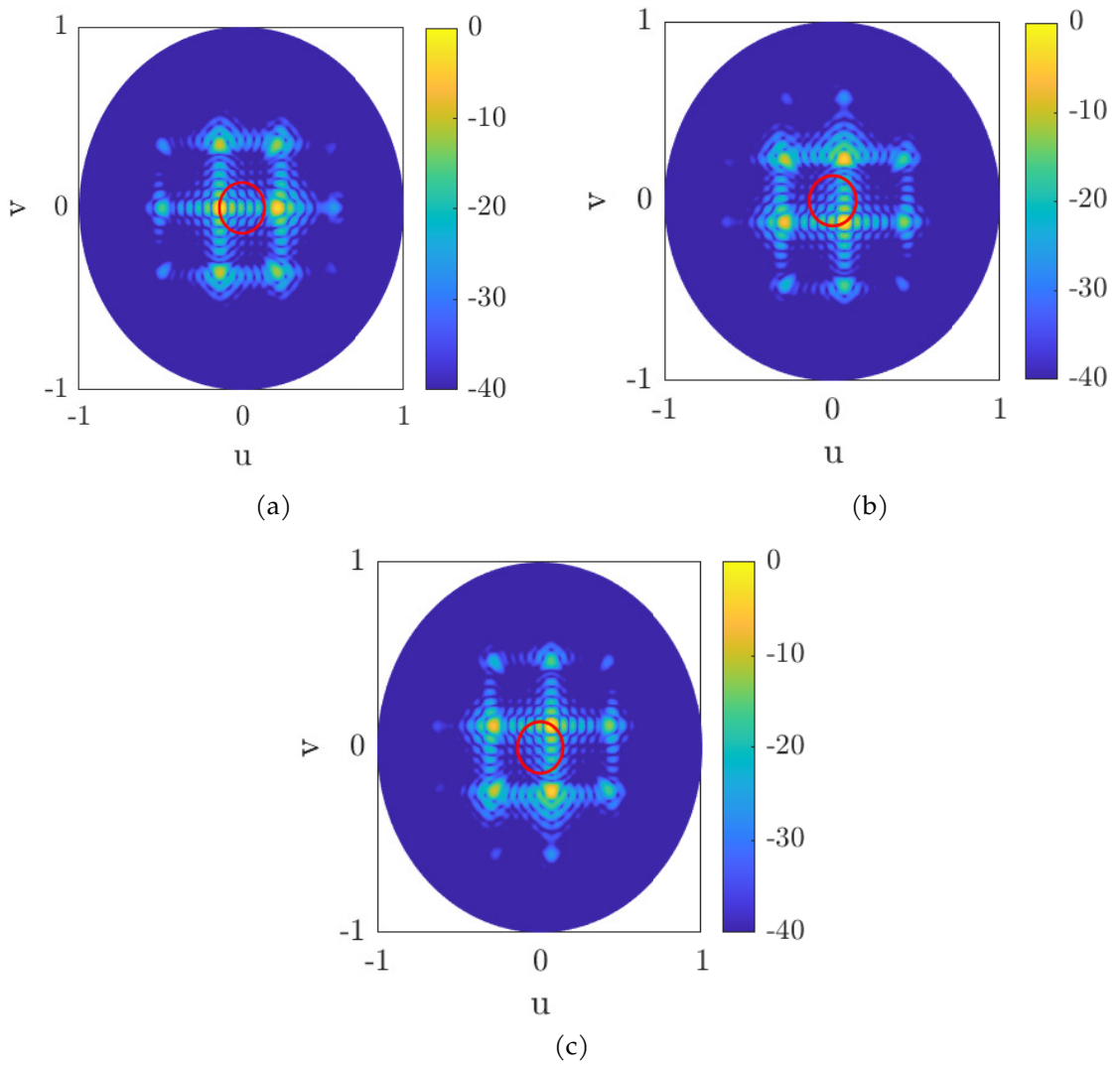

Figure 3.9 – Normalized directivity patterns in uv-coordinates of the 7×7 lens antenna with feed placed in the three focal points ($\theta_{in}^{max} = 16.2°, \phi_{in} = [0, 120, 240]°$), with FoV $\pm 8°$ (red circle).

The results for the remaining two focal points (F_2 and F_3) are not provided. This decision is related to the computational complexity of the full-wave simulations, which has already been rigorously validated for the preceding cases.

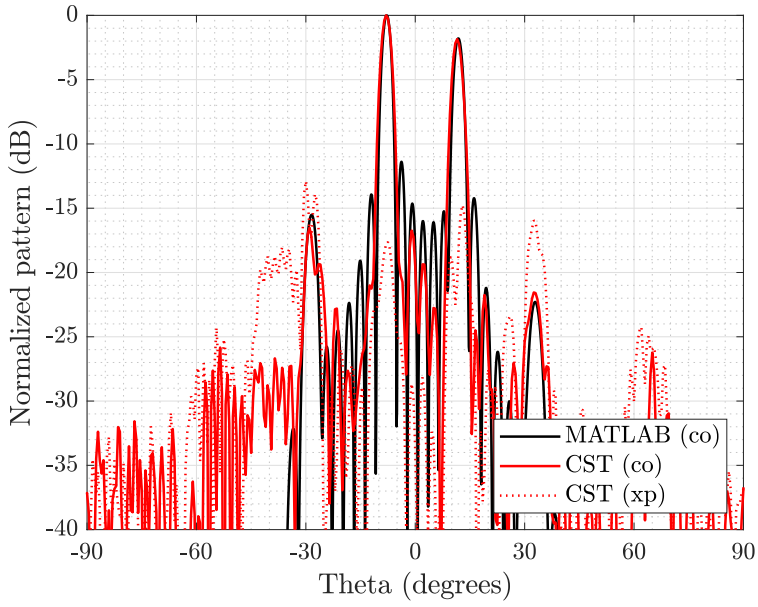

Figure 3.10 – Theoretical and simulated co-polar (co) and cross-polar (xp) patterns for the cut-plane $\phi = 0°$ of the 7×7 discrete lens with the feed placed in the focal point F_1 with ($\theta_{in}^{max} = 16.2°$, $\phi_{in} = 0°$).

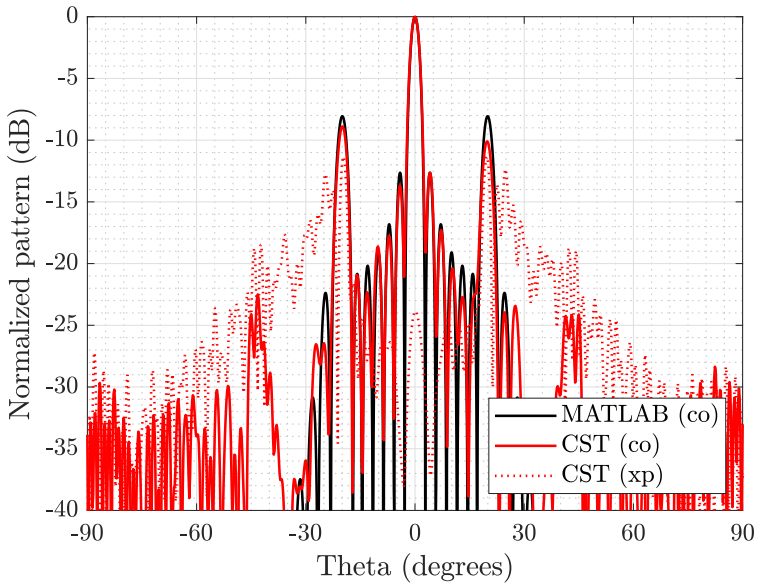

Figure 3.11 – Theoretical and simulated co-polar (co) and cross-polar (xp) patterns for the cut-plane $\phi = 0°$ of the 7×7 discrete lens with the feed placed in the center ($\theta_{in} = 0°$).

3.4 Experimental validation

For the experimental validation, a representative but reduced 3×3 prototype of a 3D discrete lens is designed. This prototype is developed first with MATLAB and subsequently with CST before the final phase of manufacturing. The goal of this section is to validate the 3D discrete lens system employing the cluster of RMWs through a comparison between numerical and measured results. The numerical results computed in MATLAB employ the same approach adopted in the previous section. In the computation of the radiation patterns, the exponential factor for the cosine pattern for the front elements is maintained the same (i.e. $q_A = 13.2$), without considering any amplitude tapering linked to the element factor of the feed and the back array elements. The phase distribution follows the same procedure used for the previous case.

Figure 3.12 shows the CST model of the 3×3 discrete lens which maintains dual polarization options, zooming factor $M = 0.5$, the same dimensions of the front and back horns and input angle of the feed $\theta_{in}^{max} = 16.2°$ to provide a pointing towards $\theta_{out}^{max} = 8°$. Smaller-size feed horns with a peak directivity of 11.5 dBi are employed to improve the compactness of the system. The RMWs cluster presents a height between profiles of $\Delta_z = 10\lambda_0$ to minimize space and simultaneously avoid reactive effects between the arrays.

Figure 3.13 shows a zoom on the CST model of the RMWs cluster designed to support dual polarization, while providing the desired phase delays between back and front arrays for focalization. The cross-section of the RMWs incorporates rounded corners, facilitating the fabrication process through AM.

The number of employed feeds is increased to 7 this time in order to enhance the multibeam system capabilities. The performances of phase aberrations will be exactly zero in the three focal points, while different from zero considering the other four feed positions. These feeds are distributed as following: 3 in the focal point positions corresponding to $\phi_{in} = [0, 120, 240]°$, 3 in the mirrored angles as $\phi_{in} = [60, 180, 300]°$ and 1 in the center for the scanning in boresight direction.

The final prototype has been manufactured by SWISSto12 employing the SLM technique and is depicted in Fig. 3.14 in different perspectives. The RF functional part (antennas, feeds, cluster of RMWs) has been manufactured by SLM using raw Aluminium finishing, while conventional machining is used to fabricate the fixture that holds all parts together.

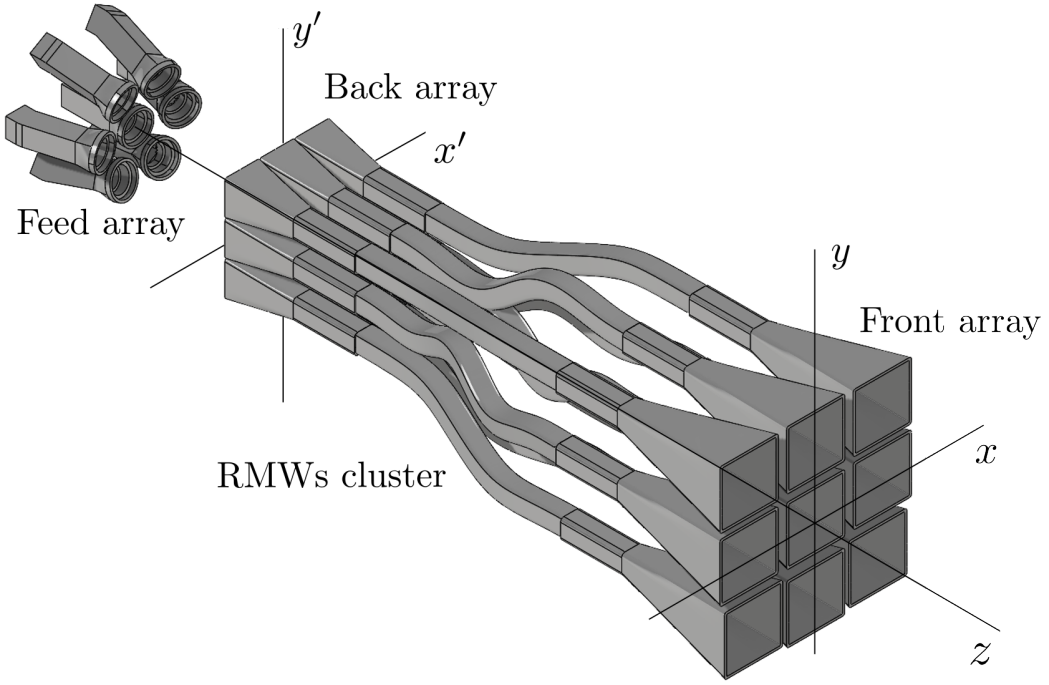

Figure 3.12 – CST model of 3×3 discrete lens antenna with a feed array of 7 horns.

The prototype consists synthetically in the following parts:

- 1 monolithic part that includes the RMWs cluster and the back septum-horns, which is 3D printed vertically to preserve the symmetries of the structure and ensure that the phase delays will be reproduced in the best possible way;
- 9 standalone monolithic front septum-horns (note that the arrangement of horns in the front array is not purely periodic, as previously explained);
- 1 monolithic 7-feed cluster, and a separate 2-waveguide expander to connect the coaxial to waveguide transitions;
- multiple Aluminum plates and bars to build and support the assembly feed with the lens. Once assembled, these bars and plates are covered with absorbers.

The measurement of the fabricated prototype has been conducted in collaboration with SWISSto12 in Switzerland and WaveLab Engineering AG in Germany. In Fig. 3.15, the experimental results are compared with the ones simulated in MATLAB when the lens is illuminated by feeds in Left-Hand Circular Polarization (LHCP) placed in two perfect focal points placed in $\phi_{in} = 0°$ and $\phi_{in} = 120°$, respectively. The patterns are plotted in the cut-planes corresponding to the specific azimuth angle. These plots show

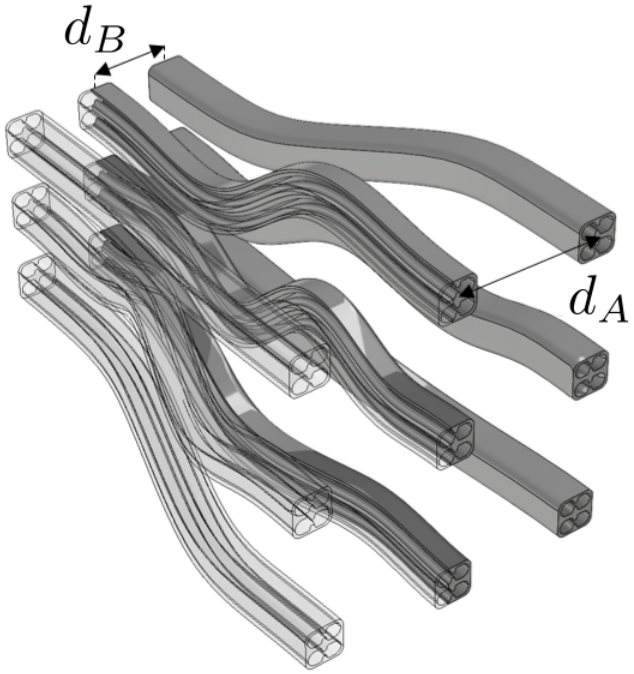

Figure 3.13 – 3×3 RMW cluster connecting front and back arrays with $d_A \approx 3\lambda_0$ and $d_B = 1.5\lambda_0$ considering a vertical height between profiles $\Delta_z = 10\lambda_0$.

the good agreement between the co-polarized simulated and measured patterns, which experimentally validates the design of entire 3D discrete lens presenting a FoV of $\pm 8°$. The numerical cross-polar results (considering the Right-Hand Circular Polarization (RHCP)) are omitted in this representation, as the initial analysis in MATLAB employs a scalar radiation pattern to describe 3D discrete lenses. The measured XPD levels remain around 20 dB in the direction of the radiated beam for both cases, highlighting good performances of the system.

The manufactured lens is able to support dual polarization features, as displayed in Fig. 3.16. The measured results obtained for both LHCP and RHCP excitations, along the one obtained from CST, are overlapped, directing the main beam toward the desired direction of $\theta_{out}^{max} = 8°$ and $\phi_{out} = 180°$.

Figure 3.17 shows the measured radiation patterns for a feed placed in a non focal point in the extreme of the frequency bandwidth, respectively at 27.5 GHz and 30 GHz. The beam pointing remains stable at both frequencies, which proves the broadband characteristic of the RMWs with respect to conventional waveguides. These measurements show that all the beams point at $\theta_{out}^{max} = 8°$ despite not being illuminated from

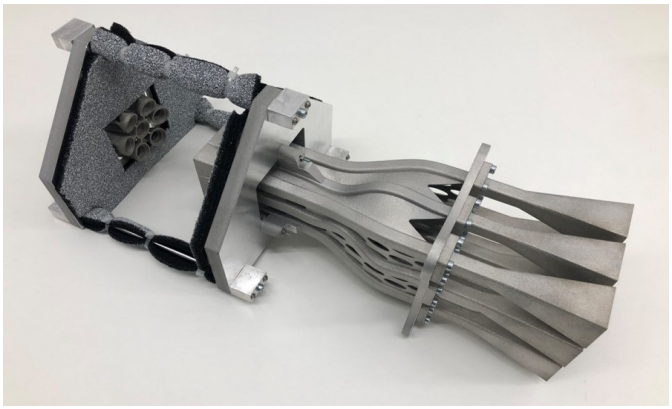

(a)

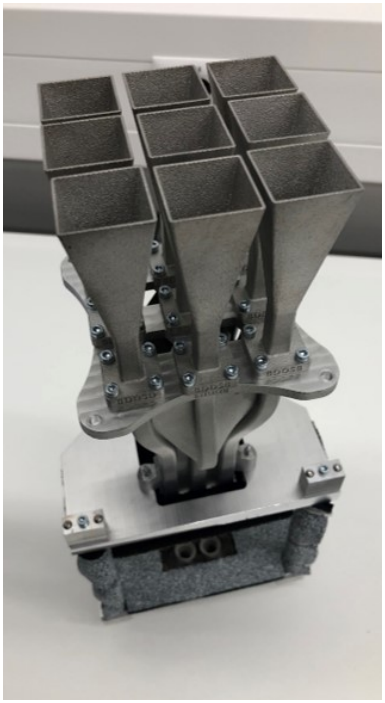

(b)

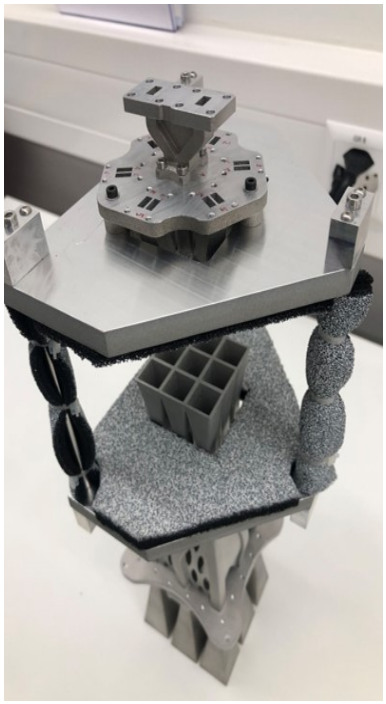

(c)

Figure 3.14 – (a) Lateral, (b) front and (c) back view of the 3×3 lens manufactured by SWISSto12 using SLM technique.

a focal point, which validates this lens antenna for multibeam applications through a true-time delay solution.

For the sake of completeness, Fig. 3.18 presents the reflection losses below 13 dB for all feed horns exciting both polarizations (LHCP and RHCP) throughout the entire bandwidth, showing also a good matching.

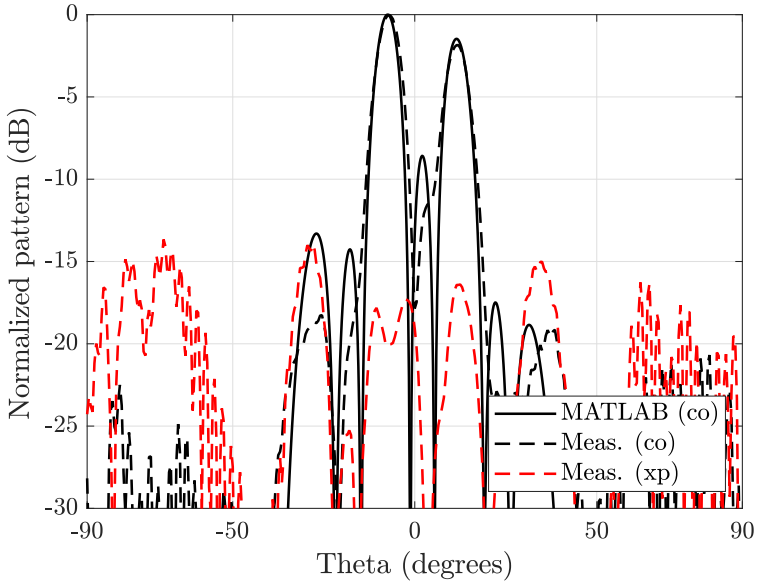

(a)

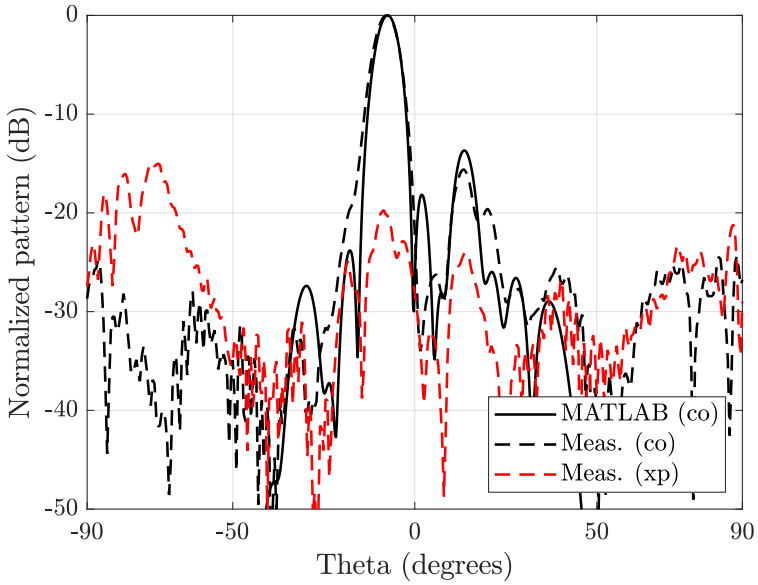

(b)

Figure 3.15 – Numerical (MATLAB) and measured radiation patterns of the 3×3 lens antenna at $f_0 = 28.5$ GHz. The feeds are placed respectively in the focal points: (a) $F_1 = (\theta_{in}^{max} = 16.2°, \phi_{in} = 0°)$ and (b) $F_2 = (\theta_{in}^{max} = 16.2°, \phi_{in} = 120°)$. Co-polarization (co): LHCP, Cross-polarization (xp): RHCP.

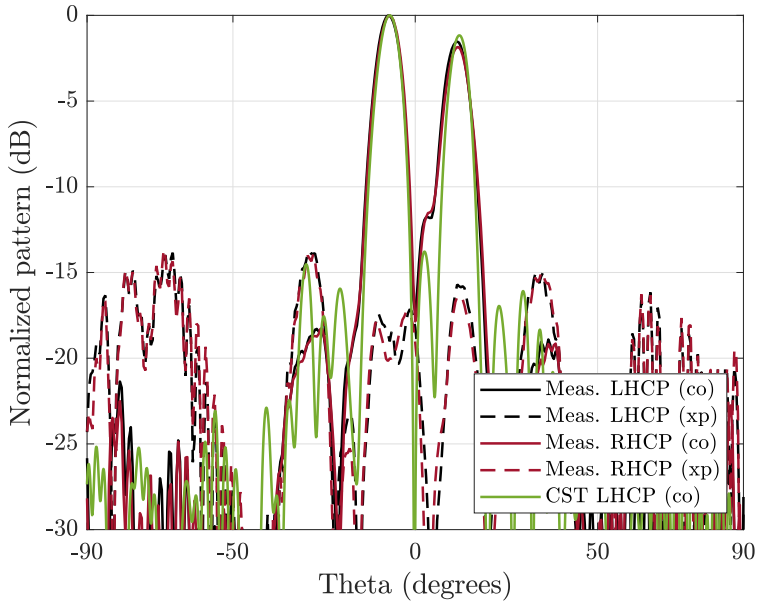

Figure 3.16 – Full-wave simulated (in green) and measured patterns at $f_0 = 28.5$ GHz considering LHCP and RHCP. The feed is placed in $\theta_{in}^{max} = 16.2°$, $\phi_{in} = 0°$.

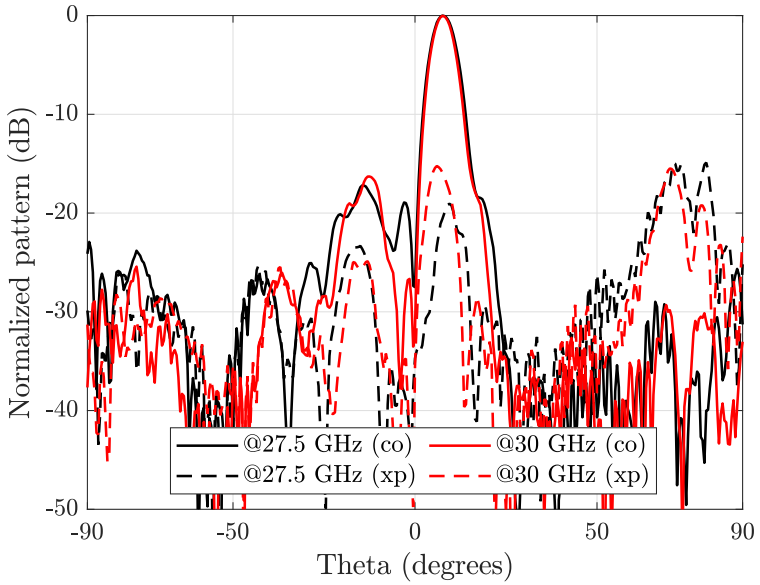

Figure 3.17 – Measured patterns at 27.5 and 30 GHz and for the cut-plane $\phi_{cut} = 240°$ of the 3×3 lens antenna. The feed is placed in $\theta_{in}^{max} = 16.2°$, $\phi_{in} = 240°$; Co-polarization (co): LHCP, Cross-polarization (xp): RHCP.

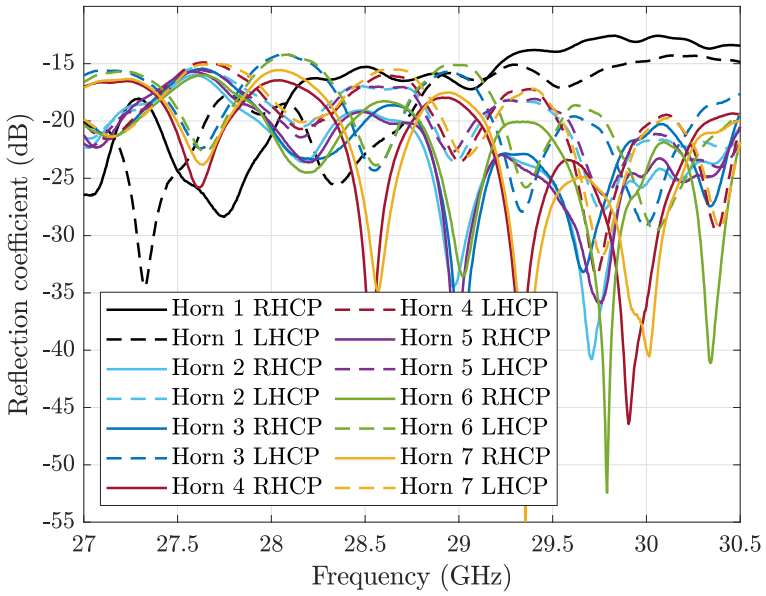

Figure 3.18 – Measured reflection coefficient (RHCP & LHCP components) for the 7 feed ports.

3.5 Conclusion

In this chapter, the innovative concept of employing AM processes to design full-metal 3D discrete lens antennas employed for scanning scenarios with a narrow FoV is presented. As potential application case, the design of a multibeam antenna for GEO satellites with FoV limited to $\pm 8°$ working in Ka-band is considered. In particular, two 3D discrete lens antennas with a magnification factor $M = 0.5$ (one with 7×7 elements, one with 3×3 elements) are conceived, where the delays lines connecting the two profiles are implemented using clusters of RMWs.

RMWs are integrated into these 3D discrete lenses to ensure spatial routing and phase control across a broad frequency range while minimizing losses with extreme flexibility in curvature. The analysis of the 7×7 element lens includes a full-wave simulation and its performance are compared to GO predictions, showing remarkable agreement between the two methodologies. On the other hand, the 3×3 element lens has been physically manufactured and its measured results exhibit a very good agreement with the numerical simulations.

This study validates 3D discrete lenses realized in AM technologies for narrow FoV applications scenarios, pointing a specific application case employed for GEO payload.

In particular, the use magnification factor smaller than one permits to meet the scanning requirements within a restricted FoV without encountering any undesirable GLs inside of it. Moreover, the incorporation of RMWs in such systems present a promising and reliable solution for low loss and broadband phase control, as demonstrated by the measured results.

The following chapter investigates a full-metal 3D discrete lens employed in a wide FoV scenario.

CHAPTER 4

Design of a 3D discrete lens for wide field of view scenarios

4.1 Introduction

In this chapter the attention is focused on AAs that provide a very large FoV (i.e. a quasi hemispherical coverage). Typical challenges in the design of AAs include increased efficiency of active elements, active and passive components with dimensions compatible with the radiating elements, large frequency bandwidth, thermal cooling, fast calibration, reduced lead time, reduced costs, low losses [149]. The target application determines which of these challenges are a priority. For example, low loss, high efficiency and accommodation in airborne and space-borne antennas [176], high power handling, large bandwidth for on-ground antenna systems including gateway stations [5]. In this scenario, the emphasis is placed terrestrial antennas designed for wide FoV. The need for this type of antenna is emerging especially for gateway antennas, that need to be connected with several LEO satellites [177].

The most consolidated antenna for gateway stations is constituted by mechanically scanning reflector antennas, with a single reflector [38] creating a single beam able to track a single satellite. Gateway stations may require a significant number of these reflectors (i.e. 50 or 60); they are expensive, require a continuous maintenance and a large separation between them in order to limit shadowing effects.

In order to reduce the cost and complexity of these gateway stations, AAs represent a

natural choice and for this reason are considered in several ongoing developments [5]. In fact, a single AA can generate multiple beams so it could replace several reflector antennas. In particular, conformal antennas constituted by different planar arrays with different inclinations to form a truncated pyramid [178] are a promising solution.

A less conventional AA solution is here proposed. This solution can enhance compactness and a trade-off between complexity and flexibility. It is based on 3D constrained lenses [125], [127]. These antennas guarantee a large FoV, multiple beams with dual polarization and large frequency bandwidth (because based on a true-time delay BFN). In the previous chapter, a proof-of concept based on 3D discrete lenses implementing RMWs manufactured in SLM, for limited scanning capabilities has been presented. In Section 1.3.4 it is also demonstrated that it is possible to increase the scanning capability of these lenses by adopting a magnification factor.

In this chapter it is presented the feasibility to attain full-metal wide angle scanning antennas based on magnified 3D lenses. In particular, here it is shown that it is possible to guarantee scanning capabilities up to 70° in a conical FoV. To the best knowledge of the author, this is the first time that such an achievement is proven possible. These antennas can be fabricated monolithically through AM. It is important to note that, unlike the situation in Chapter 3 where the FoV was limited to 8°, achieving wide FoV requires electrically large lenses. The computational cost of the simulations of these last ones is high, and full-wave simulation with commercial softwares is not even possible with good quality desktops.

To alleviate this problem, a rigorous methodology is proposed that allows to significantly reduce the computational burden, exploiting the symmetries in the front array. The proposed theoretical developments allow to prove that in order to attain wide FoV it is necessary to consider an array with a significant amount of elements. The cost associated to the fabrication of such a prototype is high and unfortunately, it is not affordable in the frame of this project. Still, since the main building blocks of the lenses were already demostrated experimentally in the previous chapter, in this one full-wave results are found to be sufficient to validate the concept. The full-wave rigorous analysis combined with a GO procedure for the back part of the lens permits demonstrating the radiative properties of the entire discrete lens antenna.

This chapter is structured as follows: the initial section presents the architecture of a magnified 3D discrete lens which aims to achieve a wide FoV. In the second part, each constitutive element in the front lens, back lens and feed array is described. The third

part is dedicated to the finite lens analysis and its validation process, starting from the sizing of the front array to achieve the large targeted FoV. A detailed explanation of the methodology employed for simulating large arrays is provided, along with a validation case study. Finally, conclusive results regarding the wide FoV scanning and multibeam functionality of the examined lens are presented.

4.2 Lens architecture

In this section, an analysis of the architecture of a magnified 3D waveguide lens for achieving wide FoV is presented. The first part consists on providing an overview of the geometry of the lens profiles, including magnification factor, focal points and DoFs. The second part is focused on some considerations related to the feed array, in order to facilitate multibeam scanning across multiple directions.

4.2.1 Magnification factor

As described in Section 1.3.4 when implementing BFNs based on discrete lenses, the designer has some freedom in scaling the pointing direction of every beam $\theta_{out,k}$ as compared to the angular position of the homologous feed generating it, associated to $\theta_{in,k}$. In particular, a zooming factor can be introduced. To provide a more comprehensive understanding of the chapter, a step further on the definition of the magnification factor is here provided. The extended definition is articulated below:

$$M = \frac{\sin(\theta_{out,k}^{GO})}{\sin(\theta_{in,k})} \approx \frac{\sin(\theta_{out,k})}{\sin(\theta_{in,k})} \tag{4.1}$$

If the FoV is narrow or the front array is sufficiently large, the output angle coincides with the one derived from the GO theory (i.e., $\theta_{out,k}^{GO} = \theta_{out,k}$), as explained in [174]. However, in the case of wide FoV scanning employing finite arrays, the scanning capabilities are constrained by the embedded patterns of the array, resulting in $\theta_{out,k}$. The difference between the two output angles becomes smaller as the array size increases.

In this work, the goal is to increase the FoV of the antenna. For this reason, the configuration with $M > 1$ is selected in order to obtain the condition on the angles: $\theta_{out,k} > \theta_{in,k}$. As a consequence, the back array size is M times larger as compared to the front array and the periodicities of the two arrays are scaled by the same factor M.

A magnification factor $M = 2$ is chosen to improve the scanning capabilities of this system, while guaranteeing large periodicity among the elements of the back array, allowing the accommodation of larger antennas.

4.2.2 Array profiles coordinates and focal point

A rotationally symmetric 3D discrete lens with flat front, spherical back arrays is chosen. A sketch is depicted in Fig. 4.1 in all its constitutive elements.

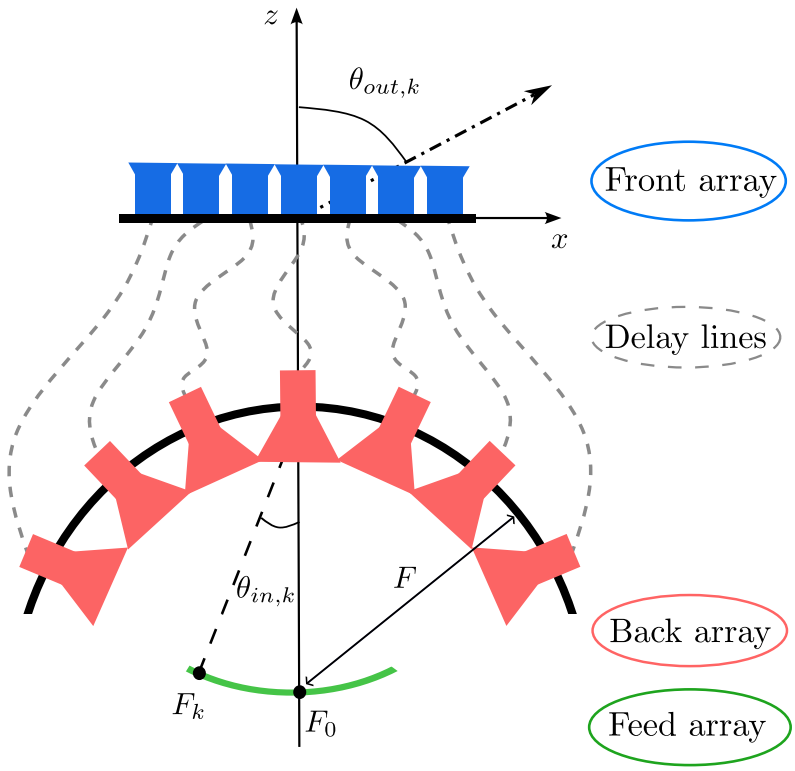

Figure 4.1 – Sketch of 3D magnified (with $M > 1$) discrete lens with flat front (in blue), spherical back (in red) and feed (in green) arrays in the xOz-plane.

The flat front array is selected to simplify the fabrication of the lens and to minimize the optical aberrations, as discussed in [122], [179]. While the spherical back array guarantees a rotational symmetry and similar illumination conditions, hence similar amplitude taperings for all the feeds. 3D discrete lenses featuring a flat front and a spherical back arrays exhibit a singular focal point and iso-phase delay lines connecting the front and back arrays [122]. By following the theoretical framework introduced in Section 1.3.3, in this case 6 out of the 7 variables are assigned (X_{A_i}, Y_{A_i}, Z_{A_i} for the front

array; X_{B_i}, Y_{B_i}, Z_{B_i} for the back array), resulting in $7 - 6 = 1$ DoF or focal point.

The focal point, represented as F_0 in Fig. 4.1, is situated on the lens axis, coinciding with the center of the sphere including the back array. This sphere has a radius equal to the focal distance F. The position of the focal point guarantees the absence of phase aberrations, as from the GO analysis in Section 1.3.3. To perform a steering of $\theta_{out,k}$ from a generic not focal point F_k (as in Fig. 4.1), a feed array (named here focal surface) is implemented. This focal surface follows the methodology outlined in [122], aiming to minimize phase aberrations within the lens. The main guidelines are described in the next subsection.

4.2.3 Optimal focal surface for multibeam scanning

Achieving multibeam scanning in discrete lenses involves strategically positioning multiple feeds at angles $\theta_{in,k}$, to point towards the corresponding $\theta_{out,k}$, as illustrated in Fig. 4.1. For the considered lens, the single focal point F_0 located in the lens axis allows zero phase aberrations in the direction of the corresponding generated wavefront Γ_0, represented in green in Fig. 4.2a. The implemented delay lines are defined to maintain the same phase delays between the back and front arrays, resulting in an optimal phase profile when considering the focal point. However, when scanning away from this focal point, some phase aberrations appear in the desired wavefront Γ_k, highlighted in green in Fig. 4.2b. These deviations are illustrated in red as Γ_{ab}, indicating the presence of aberrations in the optical system.

The proposed method (already employed on page 18 of [122]) aims to minimize the phase aberrations generated by the k-th feed in the highest number of points of the lens. In this approach, the input angle of the k-th feed ($\theta_{in,k}$) is defined, while the distance between this feed and the center of the back array (referred to as $|\overrightarrow{F_k B_1}|$) remains an unknown to be determined.

The phase path of the i-th element is illustrated by a dashed blue curve in Fig. 4.2b, connecting F_k and Γ_{ab} and it can be expressed as follows:

$$\Phi_{i,k} = k_0|\overrightarrow{F_k B_i}| + k_g W_i + k_0|\overrightarrow{A_i P_{i,k}}| \tag{4.2}$$

Ideally, $\Phi_{i,k}$ should remain constant, presenting minimal aberrations. The reference phase path is similarly shown in Fig. 4.2a, represented by a dashed blue curve connecting the central focal point F_0 and the wavefront Γ_0, denoted as $\Phi_{i,0}$. In this instance, $\Phi_{i,0}$

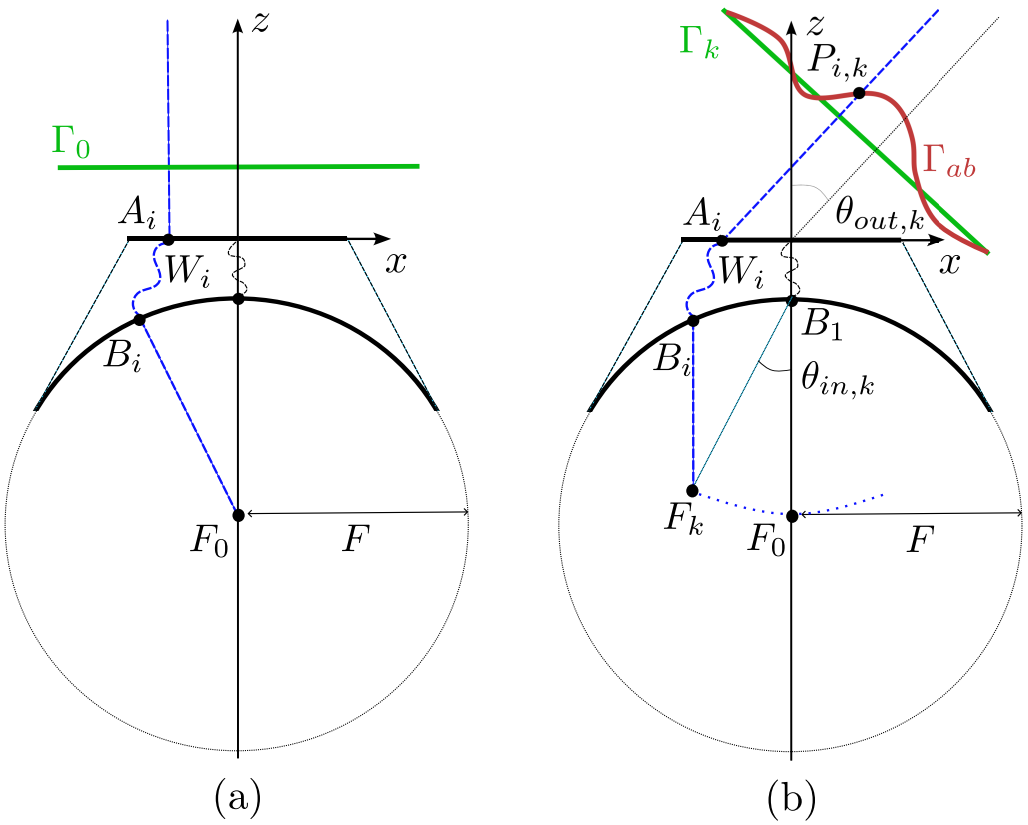

Figure 4.2 – Wavefront (in green) generated from: (a) a focal point F_0 (b) a generic feed F_k to scan up to $\theta_{out,k}$ and with phase aberrations (in red).

remains constant for all elements of the lens (being a focal point).

The implemented procedure involves varying the distance $|\overrightarrow{F_k B_1}|$ while maintaining the same input angle and minimizing the maximum difference in the phase paths as $|\Phi_{i,k} - \Phi_{i,0}|$ for every point on the lens. This allows for the identification of the optimal distance for the k-th feed, minimizing the associated phase aberrations. By repeating this routine for a wide range of input angles, it becomes possible to obtain the shape of the focal surface, as highlighted by the dotted blue curve in Fig. 4.2b.

4.3 Design of a magnified discrete lens

Once the main guidelines are established, the considerations related to the design of a magnified discrete lens to achieve scanning up to $70°$ using a magnification factor $M = 2$ are presented here. The following subsections includes the detailed design considerations for each constitutive element of the lens, addressing the front, back and

feed arrays. The goal is to ensure wide scanning angles within a conical FoV fixing the maximum output angle as $\theta_{out}^{max} = 70°$.

4.3.1 Front array

As already anticipated, a flat rotationally symmetric front array is selected. The periodicity of a phased array determines the maximum scanning angle without generating significant GLs [180]. In particular, for wide scanning angles, the periodicity of the array should be half a wavelength at the highest operation frequency [174]. In this chapter, a triangular lattice is selected for both front and back arrays to slightly increase the radiating elements dimensions (and slightly reducing their number) keeping a similar GLs rejection [174].

For the radiating elements of the front array, the Evanescent Quadridge Antenna (EQA) developed in [73] has been selected. This radiating element is specially suitable for the discrete lens, since it has an electrically small size, it is fully metallic and can be manufactured through AM [136] and it allows dual polarization operation. It also presents good scanning capabilities in all directions, without exhibiting scan blindness or spikes in the FoV (see chapter 8 in [174]). The antenna depicted in Fig. 4.3 presents $N = 4$ evanescent sections with a periodicity of $P = 0.56\lambda_0$ (evaluated at the central frequency $f_0 = 28.5\,\text{GHz}$) to prevent GLs appearing within the desired angular range of $\theta_{out}^{max} = \pm 70°$. This choice verify the corresponding condition necessary for the specified FoV: $P \leq 0.59\lambda_0$.

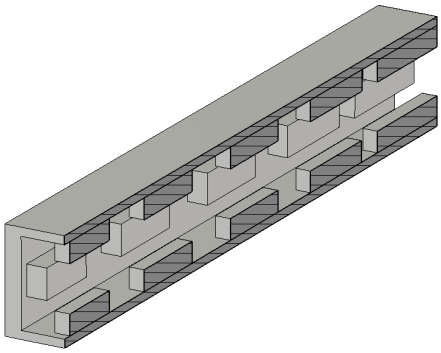

Figure 4.3 – EQA with $N = 4$ and $P = 0.56\lambda_0$ in Ka-band with $f_0 = 28.5$ GHz.

The simulated embedded pattern in an infinite environment is displayed in Fig. 4.4 for different cut-planes showing a maximum realized gain in the broadside direction

of 5.93 dBi. As expected, the pattern is not affected by any spikes within the FoV, facilitating the scanning in all the directions. In order to select the appropriate dimensions for the finite front array, a detailed analysis is conducted in Section 4.4.1.

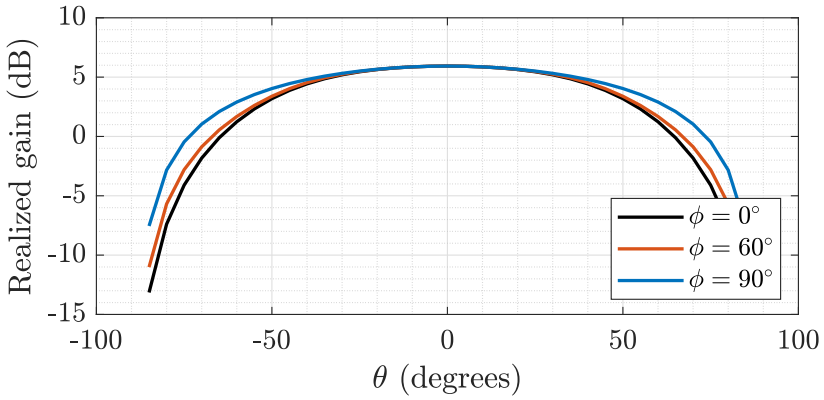

Figure 4.4 – Realized gain of the EQA simulated in an infinite environment considering three different cuts $\phi = [0,\ 60,\ 90]°$.

4.3.2 Back and feed arrays

A rotationally symmetric back array is also examined. While, the feed position is computed from the routine described in Section 4.2.3. To estimate the coupling between each feed and the elements of the back array the model in Fig. 4.5 is used. Each element of the back array is considered oriented towards the center of the sphere, coinciding with the axial focal point. $\theta_{F_{i,k}}$ and $\theta_{B_{i,k}}$ correspond to the observation angles between the vector connecting the i-th back array element and the k-th arbitrary feed and the corresponding normal to each aperture.

To compute the excitation weights of the back elements $a_{i,k}$, a simplified scalar analysis is performed (extending Eq. 1.4 in Section 1.3.5):

$$\frac{a_{i,k}}{a_{1,0}} = \frac{1}{a_{1,0}} E_{F_{i,k}} E_{B_{i,k}} \frac{e^{-jk_o|\overrightarrow{F_k B_i}|}}{|\overrightarrow{F_k B_i}|} \tag{4.3}$$

considering the normalization with respect to the central element of the back array of the lens: $a_{1,0} = E_{F_{1,0}} E_{B_{1,0}} \frac{e^{-jk_o|\overrightarrow{F_0 B_1}|}}{|\overrightarrow{F_0 B_1}|}$. The patterns $E_{F_{i,k}}$ and $E_{B_{i,k}}$ are evaluated assuming, for the k-th feed and the i-th elements in the back lens, a rotationally symmetric cosine radiation pattern with the factor q related to the horn dimensions [181]: $E_{F_{i,k}} = \cos^{q_F}(\theta_{F_{i,k}})$ and $E_{B_{i,k}} = \cos^{q_B}(\theta_{B_{i,k}})$. The factor in the denominator of Eq. 4.5

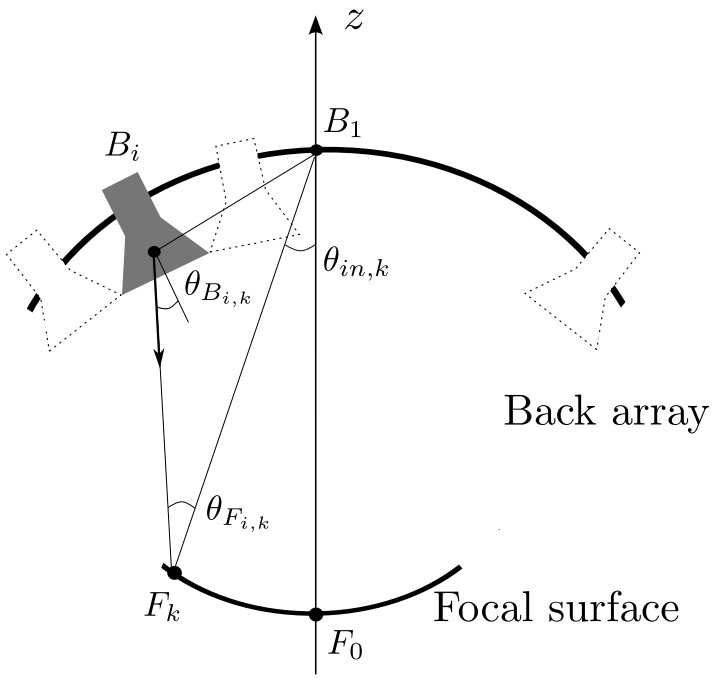

Figure 4.5 – Model to estimate the amplitude coupling between an arbitrary feed F_k pointing to the center with an angle $\theta_{in,k}$ and every element of the back array.

$\frac{1}{|\overrightarrow{F_k B_i}|}$ represents the spherical free-space propagation term from the feed to the back array, as analyzed in [182].

A value for the focal ratio $F/D_B = 1.5$ is chosen since it represents a good trade-off between illuminating the back array effectively and minimizing aberrations. The choice of the magnification factor, the front array periodicity and the focal ratio permits to define analytically the entire lens [122]. In particular, the choice of the magnification factor $M = 2$ permits to define the periodicity of the back array as the double of the one used for the front array (about $1.12\lambda_0$). The design of the back array elements is thus less challenging. Accordingly, for these larger radiating elements an exponential factor $q_B = 3$ can be expressed, in accordance with the cosine model pattern [181].

Some considerations on spillover losses should also be added. It is important to note that for passive reflectors and lenses, typical levels of the fields on the edges of the antennas are about -10 or -12 dB lower compared to the illumination of the center [38]. These edge taper illuminations guarantee negligible spillover losses. However, the discrete lens antennas considered in this thesis are particularly suitable for multi-beam AAs. For active discrete lens antennas, very high spillover losses (up to -2 or -3 dB) can be acceptable because the power level, in the front lens array, is further in-

creased with active elements [125], [127]. Hence, the spillover losses represent only low power losses that are chosen negligible in the power budget of the entire AA. These considerations justify the quite high illumination levels of the back array edges (around -6 dB). For this reason, the feed horn is modeled with the exponential $q_F = 15$ in order to present about -6 dB of apodization over the edges for the maximum steering angles $\theta_{out}^{max} = 70°$.

4.3.3 Delay lines cluster

The spherical-planar discrete lens considered in this work is characterized by equi-length and equi-phase delay lines connecting every element in the back array with its homologous element in the front array. The equi-length lines permit to convert the equi-phase phase front in the back array when illuminated from the focal point, into an equi-phase phase front in the planar front lens. This condition guarantees the perfect phase tapering to create a plane wave in the boresight direction (see Fig. 4.2b).

It is important to introduce a cluster of iso-phase delay lines with minimal losses for the connections between the back and front array. Various solutions can be employed for these delay lines including coaxial cables [125] and MWs [149]. Following the same principles outlined in the Chapter 3 for a 3D discrete lens, a cluster of RMWs is considered. These waveguides offer notable advantages, including high flexibility, low losses, a broad frequency bandwidth and compatibility with full-metal technology [149]. Consequently, the entire lens system can be manufactured as a monolithic structure using AM. The excitation port of the EQA would be fed by a septum polarizer that connects to two MWs in parallel (as in previous chapter) and then to another septum polarizer at the input of the horns in the back array.

In this context, the phase delays are considered uniform and the waveguides are assumed to be ideal, without losses along their modulated path, in line with the principles discussed in the previous chapter.

4.4 Finite lens analysis and validation

In the previous section, all the elements composing the 3D discrete lens have been dimensioned, with the aim of achieving a maximum scanning angle of $\theta_{out}^{max} = 70°$ in all directions. The main parameters selected are: $M = 2$, $P = 0.56\lambda_0$, $F/D_B = 1.5$ and

dimensions of back and feed horns to achieve specific apodization on the lens edges. In this section, a comprehensive simulation of a discrete lens is presented to validate the concept of a magnified 3D discrete lens for a wide FoV scanning. The section begins by examining the sizing of the front array of sub-wavelength EQAs. Subsequently, a methodology that allows to simulate large arrays, including a validation step for a smaller-scale problem is proposed. Lastly, the section presents the results obtained, highlighting a variety of scanning scenarios.

4.4.1 Sizing of the front array

The front radiating array in Fig. 4.21 is proposed to enable scanning capabilities of up to $70°$ in all the planes. A triangular lattice is adopted and a periodicity denoted as P, as previously defined in Section 4.3.1. The front array is configured with a circular shape to guarantee rotational symmetry. Its diameter $D_T = 2Pn_r$ considers a central element that is surrounded by $n_r = 8$ rings of identical elements.

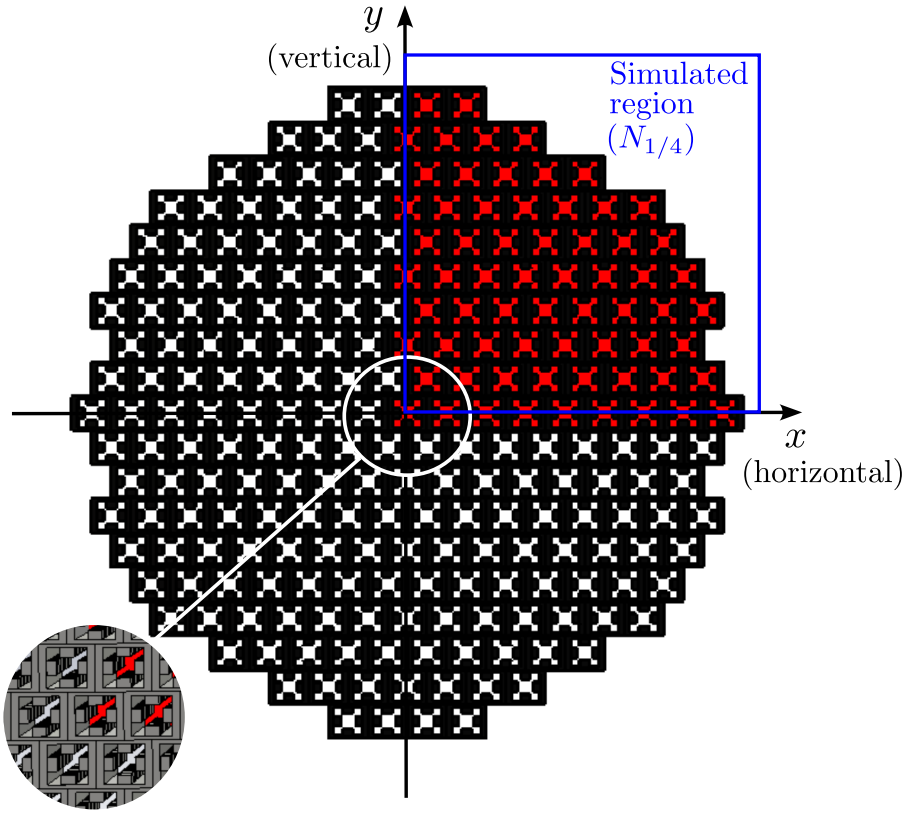

Figure 4.6 – Finite front array with $n_r = 8$ rings, periodicity $P = 0.56\lambda_0$ and diameter of $D_A = 8.96\lambda_0$ allowing for scanning up to $\theta_{out}^{max} = 70°$.

As it is well known from theory [174], the size of a radiating aperture determines the directivity of the radiation pattern and it also affects the maximum scanning angle. The relationship between the sine of the pointing angle $\sin(\theta_{out,k})$ of the lens, the sine of the input angle $\sin(\theta_{in,k})$ (as expressed in Eq. 4.1), and the dimensions of the front array is depicted in Fig. 4.7. The figure is derived by computing the steered pattern and identifying its peak value at each output angle. The analyzed pattern incorporates the embedded pattern within an infinite periodic environment for $\phi = 0°$, representing the worst scenario in terms of scanning losses (displayed in Fig. 4.4). This representation allows to identify the minimum number of rings in the front array in order to attain a desired maximum scanning angle. In particular, the value $\theta_{out}^{max} = 70°$ is considered, which corresponds to the horizontal light blue dashed line.

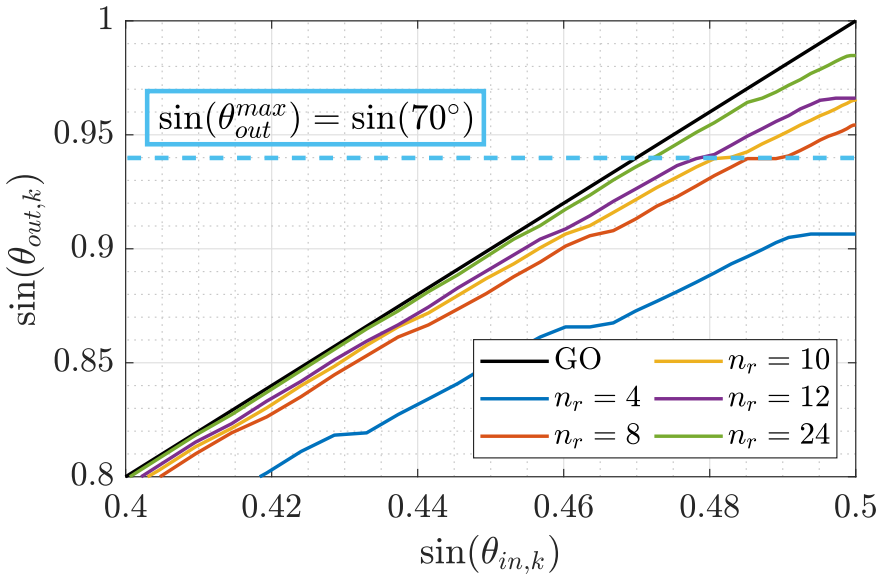

Figure 4.7 – Sizing of the front array to scan up to $\theta_{out}^{max} = 70°$ (dashed horizontal light-blue line). The front array periodicity is $P = 0.56\lambda_0$ with a triangular lattice and magnification factor $M = 2$. The black curve corresponds to the infinite number of rings array satisfying the GO relation in Eq. 4.1.

As the number of elements in the array increases (thus increasing the array diameter), the curves gradually converge towards the black curve, thus implying that $\theta_{out,k} = \theta_{out,k}^{GO}$. This convergence is coherent with the fact that large arrays are less affected by the embedded pattern of the radiating element so they tend to behave according to the GO approximation.

Figure 4.7 shows that small arrays, specifically those with less than 8 rings (denoted as $n_r < 8$), do not have the capability to attain the targeted scanning angle of $70°$ (since no value of $\theta_{in,k}$ allows to reach the light blue dashed line). Indeed, according to the theoretical framework outlined in [174], achieving wide scanning angles requires the use of large apertures. Consequently, it becomes apparent that only large arrays with $n_r \geq 8$, can fulfill the desired scanning performance criteria. The array with $n_r = 8$ rings illustrated in Fig. 4.21 is the smallest one that allows to achieve the desired scanning objective. Therefore, in order to reduce the computational burden of the simulations, this array size has been chosen for the study.

4.4.2 Modelling of front array: methodology and validation

To simulate the 3D discrete lens, the full-wave simulation of the front array is combined with the GO results considering the back lens illumination. This subsection focuses on the rigorous full-wave analysis to simulate the front array constituting the 3D lens and its validation through a smaller case. Regarding the simulation of the back lens, the next subsection shows the corresponding results.

Due to computational constraints (Intel(R) Xeon(R), CPU E5-2640 v4 2.40GHz, RAM 192Go), the direct full-wave simulation of the complete front array with 8 rings is not feasible. For this reason, a novel methodology to simulate large arrays and reduce their complexity is presented. As it can be observed in Fig. 4.21, the front array geometry features two main symmetry planes (vertical and horizontal), but it is not possible to exploit them directly in the full-wave array simulation when considering a scanned beam, since the complex excitation coefficients of the array elements are not symmetrical. For this reason, a new rigorous routine exploiting the symmetries is proposed:

- simulation of the embedded patterns of each of the elements in the array, exploiting the symmetries and reducing the computational time;
- reconstruction of the entire array pattern by adding the actual embedded patterns with the desired weights (in magnitude and phase) for scanning.

The simulations of embedded patterns for each element within the front array, implementing symmetry planes, are carried out in CST. In Fig. 4.21, two symmetry planes permit to divide the full front array almost in four quarters. This methodology allows to simulate only one quarter of array (highlighted in red) by exploiting the planes of symmetry and recombining the results to reconstruct the correspondent embedded patterns. This method effectively reduces the simulation complexity while preserving ac-

curacy. In the case of the 8 rings array, the simulation of one quarter involves $N_{1/4} = 66$ elements utilizing the vertical and horizontal symmetry planes instead of simulating the complete array with $N_{tot} = 237$ elements. The elements (in red in Fig. 4.21) are fed considering a vertical excitation along the y-axis.

When simulating a quarter array, the radiation pattern of a group of four elements is obtained. This group includes the element that is fed and the three symmetric ones. The methodology for extracting the actual embedded pattern of a singular element follows the well-established even/odd analysis method [183]–[185]. This process involves combining patterns obtained from four distinct symmetry plane configurations, incorporating both Perfect Electric Wall (PEW) and Perfect Magnetic Wall (PMW). Specifically, the configurations considered are PEW/PEW, PEW/PMW, PMW/PEW, and PMW/PMW, addressing both vertical and horizontal planes. Specific weighting factors are employed in this combination, which are dependent not only on the symmetry configuration but also on the feeding mode of the element (electric field along the y-axis, in this case).

For elements intersected by a single symmetry plane, either along the x- or y- axis, the embedded patterns are derived by combining the following configurations: respectively, PMW/PEW and PEW/PEW for elements along the x-axis or PMW/PEW and PMW/PMW for elements along the y-axis. For the elements along the x-axis, the horizontal plane is kept PEW, since the electric field is oriented perpendicular it. Similarly, analogous considerations are applied to the elements along the y-axis axis, which maintain the vertical plane as PMW. For the central element, the configuration PMW/PEW is implemented, to guarantee the boundary conditions on the electric field along the axes. To sum up, Fig. 4.8 categorizes the elements within the simulated quarter array into four distinct groups based on their symmetry properties: central element (group A), element along x and y-axes (groups B and C) and other elements (group D). Table 4.1 gives the complex weights to reconstruct the embedded patterns of the elements within the array quarter. For the patterns of the symmetrical elements, they still can be deduced by combining the results obtained from the simulated quarter array but with other weights.

The validation of this methodology is carried out considering a smaller array that can be entirely simulated in CST. This hexagonal-shaped array depicted in Fig. 4.9a consists of $n_r = 2$ rings, characterized by $N_{tot} = 19$ elements in total and $N_{1/4} = 7$ elements in a single quarter including the axial ones. A comparison is performed between the

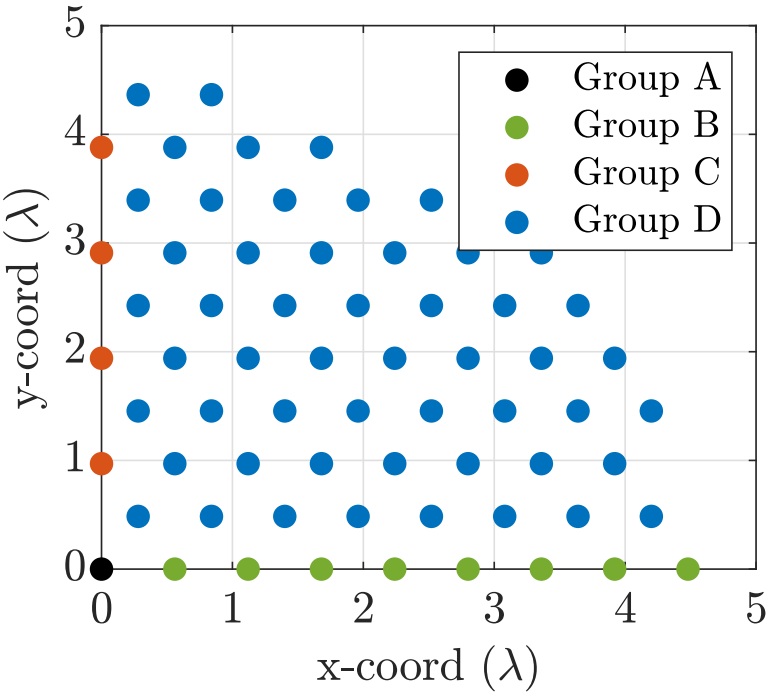

Figure 4.8 – Classification of the simulated quarter front array of $N_{1/4} = 66$ elements. Group A: central element, group B: horizontal axis elements, group C: vertical axis elements, group D: oblique axis elements.

	Planes of symmetry (vertical/horizontal)			
Group	**PMW/PEW**	**PEW/PEW**	**PEW/PMW**	**PMW/PMW**
A	$1\angle 0°$	0	0	0
B	$0.5\angle 0°$	$0.5\angle 0°$	0	0
C	$0.5\angle 0°$	0	0	$0.5\angle 0°$
D	$0.25\angle 0°$	$0.25\angle 0°$	$0.25\angle 0°$	$0.25\angle 0°$

Table 4.1 – Complex weights to reconstruct the embedded patterns of each group of front array using vertical and/or horizontal magnetic and/or electric walls.

simulated embedded patterns of all elements, both without using (NS) and with using symmetry planes (WS). The magnitude and phase of the embedded pattern of one of the elements belonging to group D is displayed in Fig. 4.9b for the cut plane $\phi = 60°$. Remarkably, a perfect match is achieved comparing the NS and WS simulations (19 vs 7 elements simulated).

For the sake of completeness, Fig. 4.10 illustrates the validation of steering perfor-

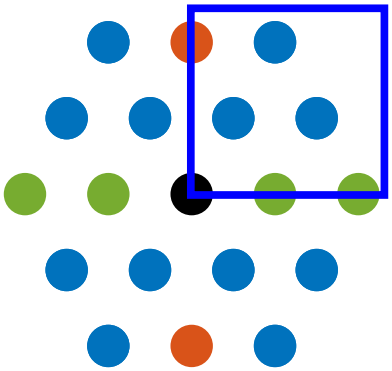

(a)

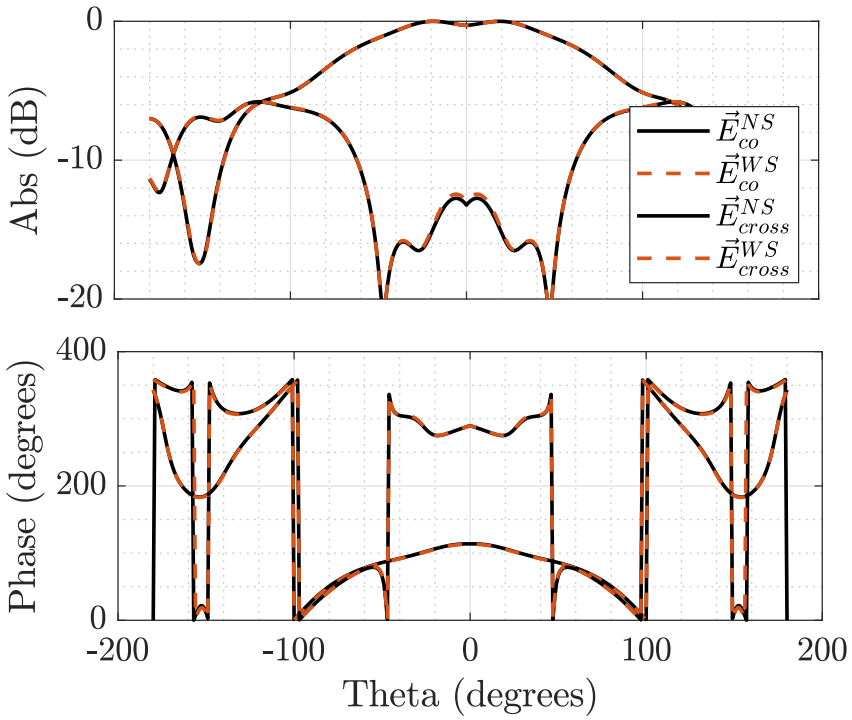

(b)

Figure 4.9 – (a) $n_r = 2$ rings hexagonal array with $N_{tot} = 19$ total elements and $N_{1/4} = 7$ simulated ones. (b) Normalized embedded pattern of an element within the group D for the cut plane $\phi = 60°$ comparing both cases NS and WS.

mances for the entire front array with 2 rings. This evaluation encompasses both NS and WS simulations, reconstructing embedded patterns for all elements. The example

chosen involves steering towards directions with $\theta_{out}^{max} = 30°$ for $\phi = 60°$, exhibiting indeed a perfect overlap. This validation completely demonstrates the effectiveness of the methodology and its applicability to full-wave simulation of large arrays, significantly enhancing computational efficiency.

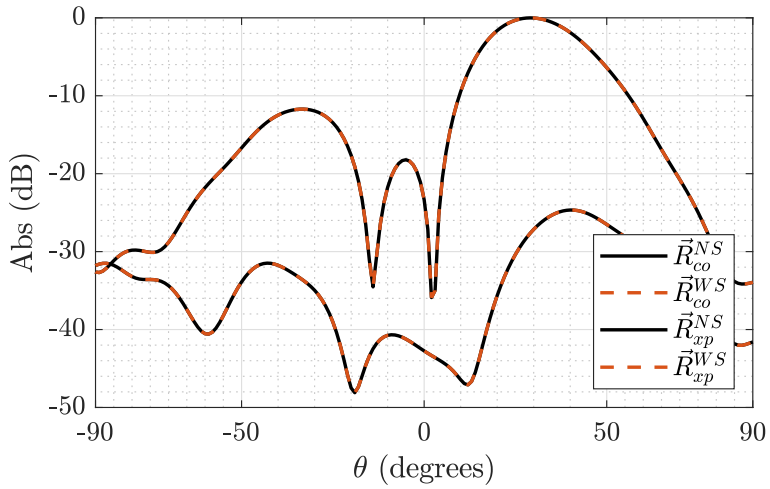

Figure 4.10 – Normalized pattern for the 2 rings array pointing at the direction $\theta_{out}^{max} = 30°$, $\phi = 60°$, by comparing the NS and WS configurations. Both co-polar and cross-polar components are shown.

4.4.3 Results of 3D Magnified Lens

As the main concepts for achieving wide-angle scanning involve the modeling of the front array and the magnification factor $M > 1$; and considering that the previous chapter extensively covered full-wave simulations of the back lens and the RMWs, the comprehensive full-wave results behind the front array are not presented in this context. In order to characterize the scanning performances of the complete 3D lens, the following steps are implemented. The methodology just described for the front array is employed. The embedded patterns of the front array are effectively combined including also the complex illumination patterns associated to the back lens, with the distribution specified in Eq. 4.3.

Some computed patterns of the 3D discrete lens having $M = 2$ and $n_r = 8$ rings, and pointing at $\theta_{out}^{max} = 70°$, are displayed in Fig. 4.11 in the uv-plane. In Fig. 4.11a, the co-polar component of the pattern for the feed placed in the x-axis ($\phi = 0°$) and pointing at $\theta_{out}^{max} = 70°$ is shown. Note that the cross-polar pattern is not displayed since the XPD

is around 60 dB along principal axes. Figure 4.11b shows the co-polar and cross-polar patterns originated when using a feed located in the plane $\phi = 60°$ are represented. The maximum XPD level is 11.34 dB for $\theta_{out}^{max} = 70°$, related to the maximum scanning angle.

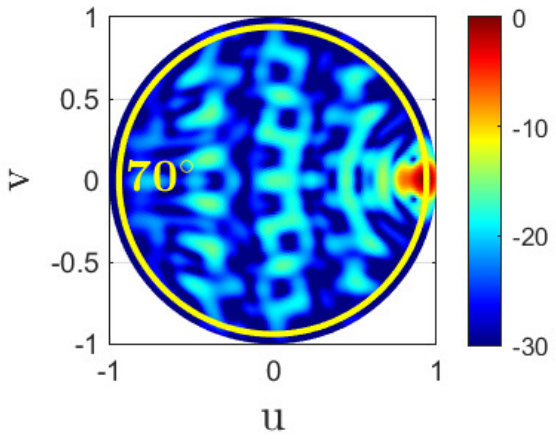

(a)

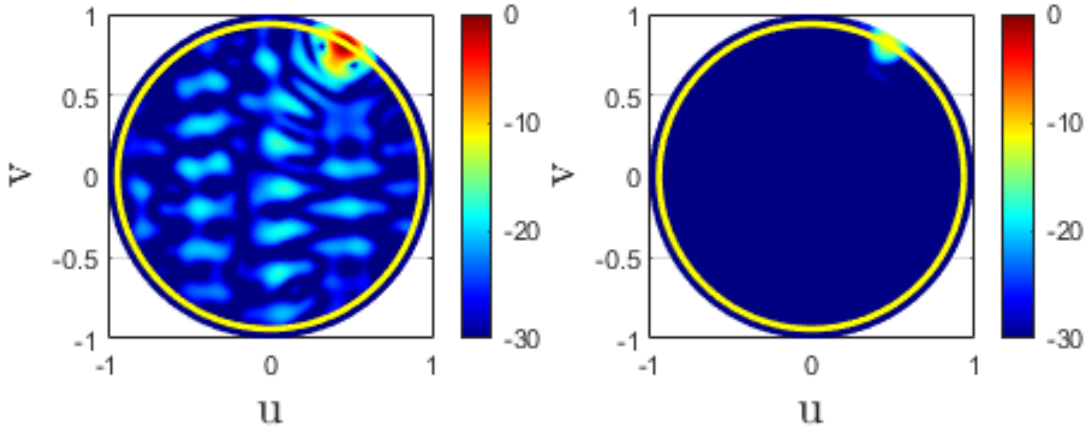

(b)

Figure 4.11 – Directivity pattern, in the uv-plane, for the 3D discrete lens pointing at $\theta_{out}^{max} = 70°$ (yellow circle). In (a) the co-polar pattern for $\phi = 0°$. In (b) the co-polar (on the left side) and cross-polar (on the right side) for $\phi = 60°$.

As an additional example, in Fig. 4.12 two patterns pointing at $\theta_{out}^{max} = 30°$ and characterized by the ϕ-angles equal to $[0, 60]°$, are plotted. The XPD level is around 60dB in the horizontal plane and 27.22dB along in the $\phi = 60°$ plane. The size of the feed is not changed for all the pointing angles; it could be adjusted by slightly increasing the

feed dimensions when increasing the scanning angle in order to keep stable spillover losses and back lens aperture efficiency.

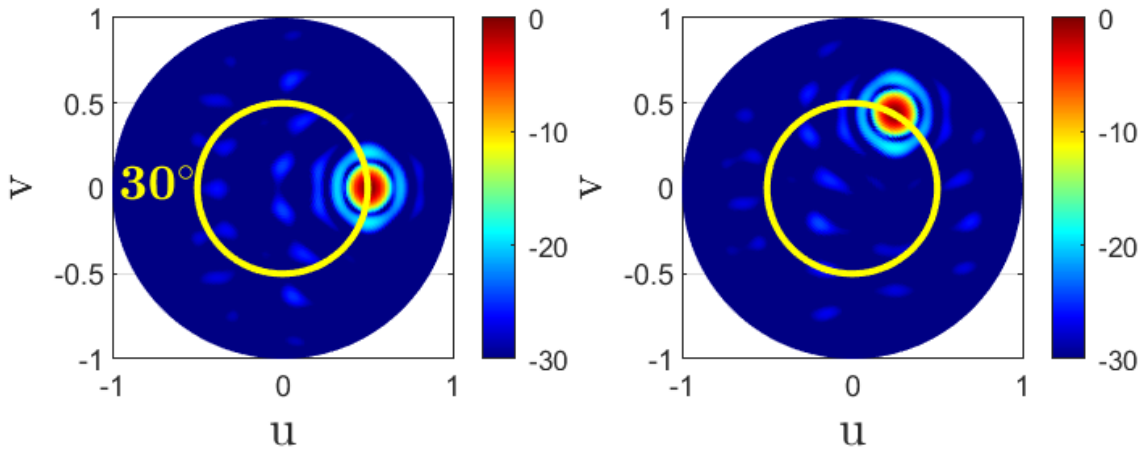

Figure 4.12 – Co-polar directivity pattern, in the uv-plane, for the 3D discrete lens pointing at $\theta_{out}^{max} = 30°$, $\phi = 0°$ (on the left side) and $\phi = 60°$ (on the right side).

Figure 4.13 presents a comparison of the multibeam performance achieved in this work adopting a magnification factor $M = 2$ (continuous lines) as compared to a conventional configuration with $M = 1$ (dashed lines). It is important to observe that for small and medium scanning angles the performance with the two types of lenses are practically identical. In these conditions, the lens with $M = 1$ should be preferred because more compact. For such configuration, the front and back arrays have the same diameter, as well as input and output angles (see Fig. 1.26 in Section 1.3.4).

For larger pointing angles (from $50°$ to $70°$), the $M = 2$ solution exhibits significant advantages. The improved scanning capabilities have a cost associated mainly to the increased volume for the back lens, feeding array, and focal distance. This cost can be acceptable for professional ground antennas. Viceversa, for on-board satellites a discrete lens with increased back part could be acceptable only if the platform offers sufficient

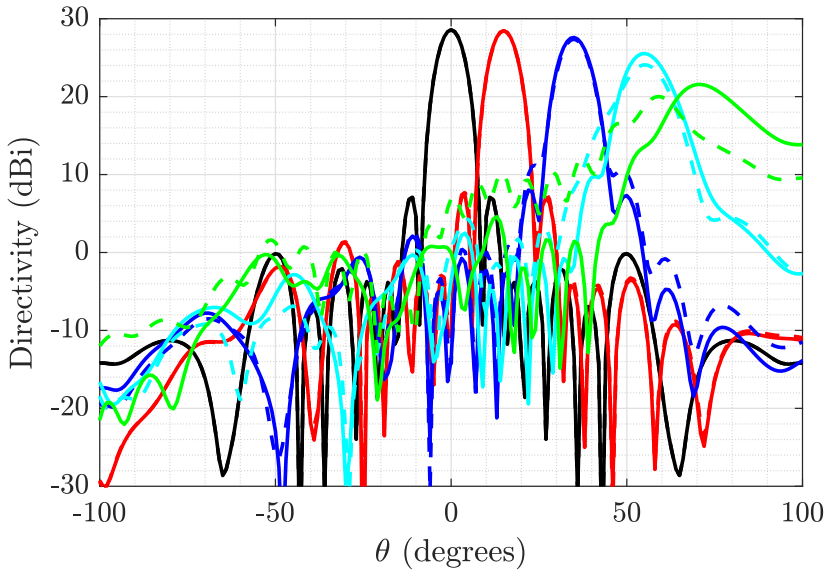

(a)

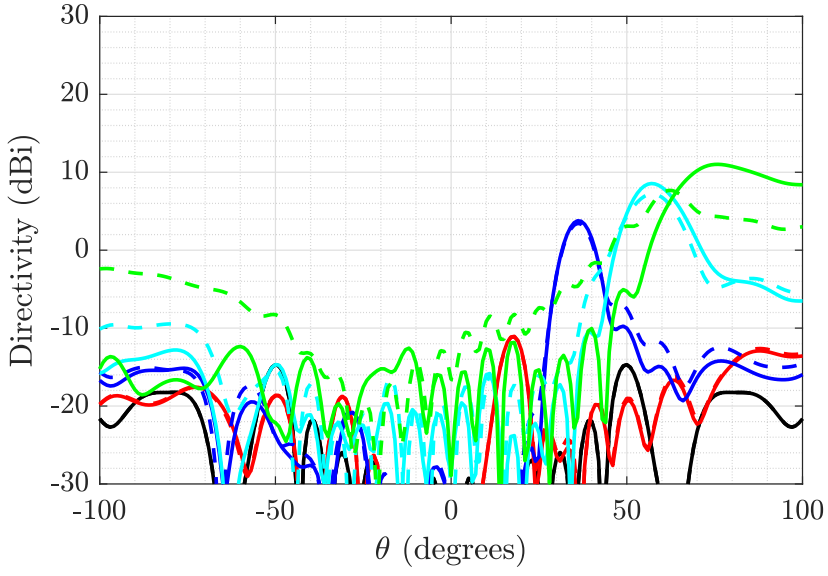

(b)

Figure 4.13 – Comparison of the (a) co-polar and (b) cross-polar directivity patterns of the lens pointing at the angles $\theta_{out,m} = [0, 15, 35, 55, 70]^\circ$ in the plane $\phi = 60^\circ$ considering $M = 2$ (solid lines) and $M = 1$ (dashed lines).

accommodation volume (an increased frequency can help in order to miniaturize this type of lens with $M > 1$).

In Fig. 4.14 the magnitude and phase taperings on the back lens aperture when illu-

minated by a feed allowing to point at the maximum angle $70°$ in the plane $\phi = 60°$ are represented for discrete lenses characterized by $M = 1$ and $M = 2$. The considerations done in Section 4.3.2 justify the magnitude levels (around -6 dB) on the back array in the configurations with $M = 2$ when considering the maximum scanning angle in Fig. 4.14a. Viceversa, in the configuration with $M = 1$, the back lens is poorly illuminated by the feed pointing in the same maximum angle as demonstrated by the amplitude levels in Fig. 4.14b).

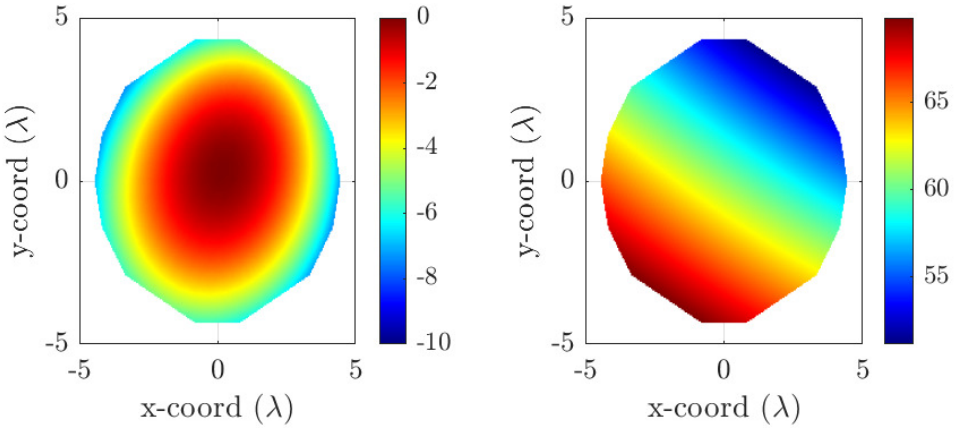

(a)

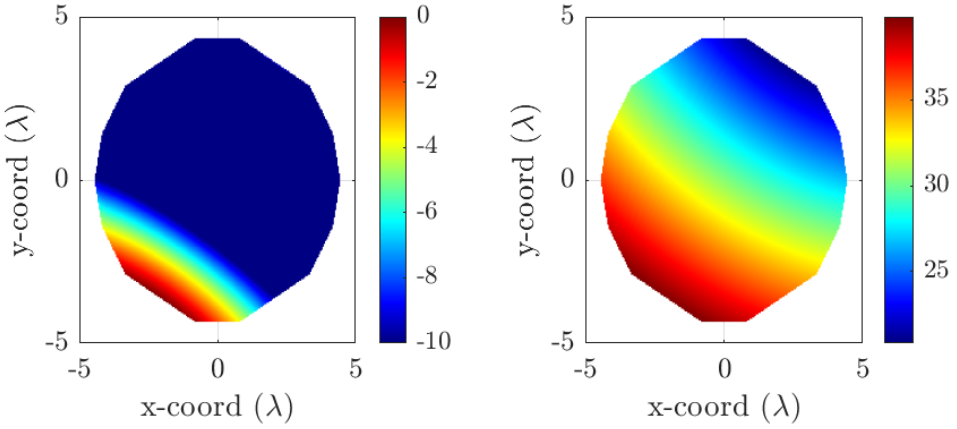

(b)

Figure 4.14 – Amplitude (on the left) and phase (on the right) taperings over the back array considering the scanning $\theta_{out}^{max} = 70°$, in the plane $\phi = 60°$ for (a) $M = 2$ and (b) $M = 1$.

For the sake of completeness, Fig. 4.15 shows additional results concerning the comparison of the proposed full-wave methodology and a commonly employed approximation. The latter consists in considering that all the elements in the front array have

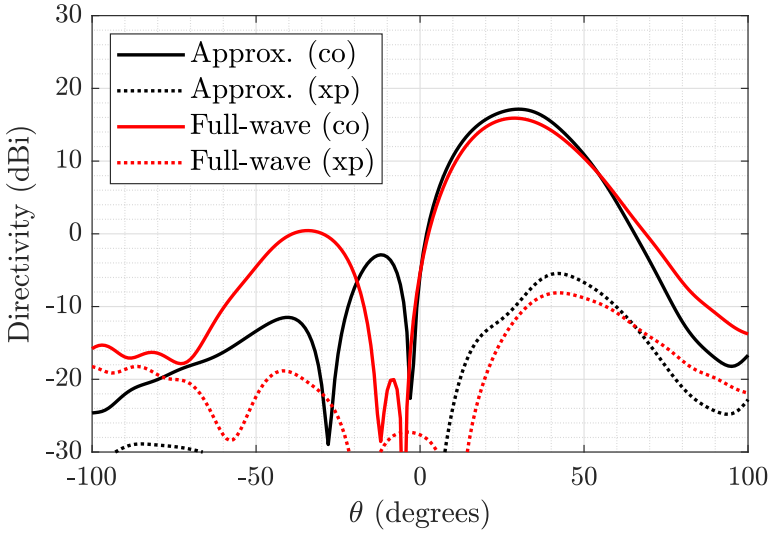

(a)

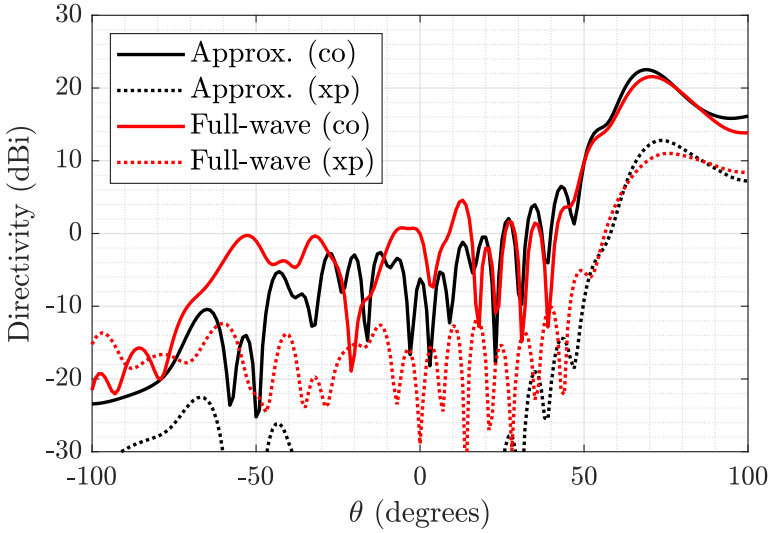

(b)

Figure 4.15 – Comparison between the approximated and the full-wave approach results for the co-polar and cross-polar patterns in $\phi = 60°$. (a) $\theta_{out}^{max} = 30°$ for the 2 rings array, (b) $\theta_{out}^{max} = 70°$ for the 8 rings array.

the same embedded pattern as the central one in the 8 rings array. Two specific scenarios are analyzed, the first one is shown in Fig. 4.15a and concerns the 2 rings array presented in Fig. 4.9a for the case $\theta_{out}^{max} = 30°$, $\phi = 60°$. The second one is presented in Fig. 4.15b and considers the 8 ring lens when scanning at $\theta_{out}^{max} = 70°$ in $\phi = 60°$. These results show that assuming an identical element factor (evaluated adopting a full-wave

technique for an infinite periodic array) for all the elements constituting the finite front array of the lens implies some not negligible errors in both the co-polar and cross-polar patterns evaluations.

As a final remark, in order to assess the improvements achieved with the discrete lens with a magnification factor $M = 2$ proposed in this chapter, it has been demonstrated that the scanning capability has been increased from about $50°$ to about $70°$ in all the azimuthal planes as compared to 3D discrete lenses not exploiting the magnification factor. This increase corresponds to an enlargement of about 50% in a conical field of view in the uv-plane because the scanning region extension is proportional to the area covered which is proportional to $\sin^2(\theta_{out}^{max})$ as following: $(\pi \sin^2(50))/(\pi \sin^2(70)) = 1.5$. In practice, this means that the lens proposed in this chapter is able to increase by 50% the number of realizable beams generated by the active discrete lens thanks to the magnification factor.

4.5 Conclusions

In this chapter, the design of a magnified 3D discrete lens for wide FoV scanning has been proposed. By exploiting a magnification of the back part of the lens, a maximum scanning angle of about $70°$ has been demonstrated. The shape of the radiation pattern of the radiating elements in the front lens tend to limit the direction of pointing of the realized beams. However, by selecting discrete lenses with a sufficiently large front array this effect can be minimized. The electromagnetic simulation of 3D magnified discrete lenses is computationally cumbersome. For this reason a rigorous methodology exploiting different types of symmetries has been successfully employed and validated for the front lens array. This efficient full-wave analysis for the front lens, combined with the GO employed for the back lens permits to characterize accurately the entire discrete lens antenna deriving its radiation patterns. To demonstrate the concept, a 8 rings 3D discrete lens characterized by a magnification factor of $M = 2$ with 237 elements and assuring a maximum scanning angle of at least $70°$ in all the azimuthal planes has been demonstrated. By doubling the magnification factor, from $M = 1$ to $M = 2$, the maximum scanning angle has been increased from about $50°$ to about $70°$. This increase corresponds to an enlargement of about 50% in the extension of the conical FoV of the antenna which corresponds to an increase by 50% in the number of realizable beams.

Conclusions and future perspectives

Overview

This chapter presents the main results achieved in this thesis. The general conclusions from Chapter 1 to Chapter 4 are first discussed and the main contributions are enumerated concisely. The research lines opened by this thesis are then outlined, showing the future perspectives. Finally, a list of the author's publications related to the present work are provided.

General conclusions

As the demand for high capacity, enhanced power efficiency and multibeam coverages continues to increase across spatial and terrestrial platforms, there is a notable evolution towards the development of full-metal AA systems. 3D discrete lenses in waveguide technology represent a possible solution to reach good performance in terms of low losses, scanning flexibility, dual polarization and wide bandwidth. The development of full-metal 3D discrete lenses is proven to be possible in this thesis by AM techniques to minimize losses, also to enhance compactness and provide high power handling. The present thesis is devoted to the modeling and design of these systems for multiple scenarios. In the following, the general conclusions concerning each chapter are listed.

The first part of Chapter 1 focuses on a comprehensive review of high-gain full-metal antennas intended for multibeam scanning applications, whether for on-board or on-ground platforms. The analysis includes a comparative examination, featuring various solutions such as reflector-based systems, antenna arrays and lenses. Addition-

ally, the essential properties of AM are outlined, enabling the fabrication of full-metal 3D discrete lenses, identified as promising candidates for the aforementioned features. Subsequently, the theoretical aspects of these lenses are examined across all their constitutive elements.

Chapter 2 begins with an analysis of MWs through AM techniques used to synthesize specific phase delays. This involves the utilization of curved and flexible devices to establish connections between two arbitrary points. These components not only enable low losses but also support dual polarization features, wide frequency bandwidths and exhibit extreme versatility in their geometries. Their applicability spans a wide range of scenarios. Several examples are provided to validate the effectiveness for both building and simulation methodologies. Furthermore, the simulation and validation of a cluster of RMWs intended for deployment in space systems across various scenarios are also presented.

In Chapter 3, full-metal 3D discrete lenses to achieve a narrow FoV are analyzed and tested. The study is centered on a specific example related to GEO satellites requiring a FoV of 8°. By choosing a magnification factor smaller than one, it is possible to attain narrow FoVs, leading to smaller accommodations, particularly suitable for space platforms. The chapter details the implementation of a RMWs cluster designed to provide the desired phase delays for focalization within the specified FoV. Two examples are presented: a large one, analyzed in simulation and a smaller one, manufactured through full-metal additive manufacturing. The latter demonstrates the measured performances emphasizing the overlap with simulated results. This dual example approach contributes to a comprehensive understanding of the practical applications and effectiveness of the proposed techniques.

Chapter 4 introduces the design process for a 3D magnified discrete lens using waveguide technology, enabling wide angle scanning in multiple directions. The example case is this time focused on gateway antennas for ground applications. The use of a magnification factor greater than one allows for large scanning angles. To demonstrate this capability, a FoV up to 70° is pointed out. To achieve this, a new methodology is proposed to implement a full-wave analysis of such 3D discrete lens to speed up the computation. Adopting both GO and rigorous full-wave analysis, it is shown that this type of antennas is able to create beams pointing up to wide scanning angles in a conical FoV.

Original contributions

This thesis examines the concept related to the fabrication of 3D discrete lenses through AM techniques, exploring their potential applications across multiple scenarios. In this section the original contributions are summarized and organized according to the objectives reported in the introduction.

Ridged meandered waveguides:

- Introduction of full-metal RMWs in AM to provide some degree of flexibility in spatial routing between two points while maintaining a broad bandwidth, a desired phase delay, low losses and high power handling.
- Analytic formulation of the meandered trajectory, including the definition of the step baseline function and the application of the parallel transport approach to modulate the trajectory and optimize the phase delay.
- Introduction of a methodology for building and synthesizing efficiently clusters of RMWs to synthesize a group of phase delays, employed in several scenarios.

3D discrete lenses for narrow FoV scenarios:

- Design and full-wave simulation of a 7x7 3D discrete lens employing a cluster of RMWs and a magnification factor smaller than one to reach a FoV of $\pm 8^{\circ}$ compatible with GEO scenarios.
- Experimental validation through AM and measurement of a 3x3 prototype.

3D discrete lenses for wide FoV scenarios:

- Design and analysis of a rotational symmetric 3D discrete lens to reach scanning up to 70° towards multiple directions, employing magnification greater than one, suitable for gateway antenna systems.
- Study and validation of a rigorous full-wave methodology exploiting different types of symmetries, reducing the computational burden to simulate large array problems.
- Complete analysis of a 3D discrete lens combining GO and the rigorous full-wave analysis to create beams pointing up to wide angles from the boresight direction in a conical FoV.

Future perspectives

In this work several concepts related to the development of full-metal 3D discrete lenses for several space scenarios have been presented, leading to some future research perspectives. These latter are summarized in the following:

- Improvement and study of an analytic formulation to describe the reactive effects related to the implementation of MWs (e.g. equivalent circuits).
- Implementation of polarization features and the full-wave pattern of the feed and back horns in the GO radiation pattern computation for a generic 3D discrete lens.
- Manufacturing of an intermediate prototype of 3D discrete lens for wide scanning angles to point up to 50° employing 4 rings lens array.
- Theoretical procedure for the design of not rotationally symmetric 3D discrete lenses with minimized the optical aberrations for extended FoV.
- Use of the full-wave methodology to simulate large arrays with more geometrical symmetries (e.g. triangular lattice with symmetries for each 60°).
- Design and prototyping of an active 3D discrete lens employing amplifiers between cluster of MWs and front array.

List of publications

Papers in international journals

- **L. Berretti**, R. Loison, E. Menargues, L. Polo-López, G. Toso and M. García-Vigueras, "Multibeam Antennas based on 3D Discrete Lenses with Magnified Field-of-View" (under review).
- **L. Berretti**, R. Loison, E. Menargues, S. Capdevila, L. Polo-López, G. Toso and M. García-Vigueras, "Ridged Meandered Waveguides for 3-D Routing and Phase Delay Control and Its Application to Discrete Lenses," in *IEEE Transactions on Antennas and Propagation*, vol. 71, no. 5, pp. 4017-4027, May 2023.

Papers in international conferences

- **L. Berretti**, L. Polo-Lopez, E. Menargues, R. Loison, G. Toso and M. García-Vigueras, "The role of Additive Manufacturing in Space-borne Active Antenna," 2023 17th *European Conference on Antennas and Propagation* (EuCAP), Florence, Italy, 2023, pp. 1-4.
- L. Polo-López, **L. Berretti**, C, Molero, E. Menargues, R. Contreres, J. Córcoles, J. A. Ruiz-Cruz and M. García-Vigueras, "Application of FSS-cells Stacking to the Conception of Compact Inline Waveguide Polarizers Lucas," 2023 17th *European Conference on Antennas and Propagation* (EuCAP), Florence, Italy, 2023, pp. 1-5.

Papers in national conferences

- **L. Berretti**, M. García-Vigueras, G. Toso, L. Polo-López, E. Menargues and R. Loison, "Méthode paire/impaire pour alléger la simulation électromagnétique rigoureuse de réseaux phasés à fort dépointage," *XXIIIèmes Journées Nationales Microondes* (JNM), 5-7 juin 2024 - Antibes Juan-Les-Pins, France (submitted).

- **L. Berretti**, G. Toso, M. García-Vigueras, E. Menargues, S. Capdevila and R. Loison, "Etude de faisabilité de lentilles discrètes 3D réalisées par fabrication additive," *XXIIèmes Journées Nationales Microondes* (JNM), 4-7 juin 2022 - Limoges, pp. 1-4, France.

Bibliography

[1] G. Denis, D. Alary, X. Pasco, N. Pisot, D. Texier, and S. Toulza, « From new space to big space: how commercial space dream is becoming a reality », *Acta Astronautica*, vol. 166, pp. 431–443, 2020.

[2] A. Golkar and A. Salado, « Definition of new space—expert survey results and key technology trends », *IEEE Journal on Miniaturization for Air and Space Systems*, vol. 2, *1*, pp. 2–9, 2021.

[3] OCDE, *The Space Economy in Figures: How Space Contributes to the Global Economy, Editions OCDE, Paris*. 2019, pp. 107–117.

[4] *Newspace constellation index*, `https://www.newspace.im/`, © Made by Erik Kulu, 2016 - 2023.

[5] G. He, X. Gao, L. Sun, and R. Zhang, « A review of multibeam phased array antennas as LEO satellite constellation ground station », *IEEE Access*, vol. 9, pp. 147 142–147 154, 2021.

[6] R. De Gaudenzi, P. Angeletti, D. Petrolati, and E. Re, « Future technologies for very high throughput satellite systems », *International Journal of Satellite Communications and Networking*, vol. 38, *2*, pp. 141–161, 2020.

[7] H. A.-D. Kokez, « On terrestrial and satellite communications for telecommunication future », *2020 2nd Annual International Conference on Information and Sciences (AiCIS)Symposium on Antennas and Propagation (ISAP), Fallujah, Iraq*, 2020, pp. 58–67.

[8] S. Rao, « Workshop 4: satellite communication antennas: challenges for the next generation payloads », *2017 International Symposium on Antennas and Propagation (ISAP)*, 2017, pp. 1–1.

[9] S. Amos and H. Fenech, « Flexibility in multi-beam satellite antennas: requirements, challenges and solutions », *12th European Conference on Antennas and Propagation (EuCAP 2018)*, 2018, pp. 1–5.

[10] B. Palacin, N. J. G. Fonseca, M. Romier, R. Contreres, J.-C. Angevain, G. Toso, and C. Mangenot, « Multibeam antennas for very high throughput satellites in europe: technologies and trends », *2017 11th European Conference on Antennas and Propagation (EUCAP)*, 2017, pp. 2413–2417.

[11] *Airbus presents ground-breaking technology for eutelsat quantum*, `https://www.airbus.com/en/newsroom/press-releases/2019-11-airbus-presents-ground-breaking-technology-for-eutelsat-quantum`, Madrid, November 21, 2019.

[12] *Hispasat 36w-1*, `https://www.hispasat.com/en/satellite-fleet/hispasat-36w-1`, 2017.

[13] *One sat*, `https://www.airbus.com/en/space/telecom/onesat`, 2022.

[14] *Aramis flexible payload*, `https://swissto12.com/aramis-flexible-payload/`, March 21, 2022.

[15] M. Yajima, T. Kuroda, T. Maeda, M. Shimada, S. Kitao, and K. Hariu, « Active phased array antenna for WINDS satellite », *25th AIAA International Communications Satellite Systems Conference (organized by APSCC)*.

[16] « Thinkom unveils new multi-beam, reconfigurable, phased-array gateway solution for next-gen satellites ». (2019), [Online]. Available: `https://www.thinkom.com/announces-multi-beam-phased-array-gateway-antennas/`.

[17] C. Arnold. « An overview of how Starlink's phased array antenna "dishy mcflatface" works ». (2023), [Online]. Available: `https://www.linkedin.com/pulse/overview-how-starlinks-phased-array-antenna-dishy-works-curtis-arnold/`.

[18] R. J. Mailloux, S. G. Santarelli, T. M. Roberts, and D. Luu, « Irregular polyomino-shaped subarrays for space-based active arrays », *International Journal of Antennas and Propagation*, vol. 3, *2*, pp. 1687–5869, 2009.

[19] P. Angeletti, G. Toso, and G. Ruggerini, « Array antennas with jointly optimized elements positions and dimensions part II: planar circular arrays », *IEEE Transactions on Antennas and Propagation*, vol. 62, *4*, pp. 1627–1639, 2014.

[20] V. Tugend and A. Thain, « Hybrid beamforming with reduced grating lobes for satellite applications », *12th European Conference on Antennas and Propagation (EuCAP 2018)*, 2018, pp. 1–5.

[21] J. Belluot, G. L. Rhun, P. Augoyat, G. Mouchon, A. Maati, A. Katz, B. Gray, and R. Dorval, « A 40 w Ka-band RF amplification chain for space telecommunication SSPA applications », *2019 49th European Microwave Conference (EuMC)*, 2019, pp. 404–407.

[22] G. Toso and P. Angeletti, *Two-dimensional and three-dimensional discrete constrained lenses with minimized optical aberrations*, Patent WO/2022/161633 Aug. 4th 2022.

[23] I. Gibson, D. Rosen, and B. Stucker, *Additive Manufacturing Technologies: 3D Printing, Rapid Prototyping, and Direct Digital Manufacturing*. Springer New York, 2014.

[24] J. O. Milewski, « Additive manufacturing of metals: from fundamental technology to rocket nozzles, medical implants, and custom jewelry », *Additive Manufacturing of Metals*, 2017.

[25] B. Redwood, F. Schffer, and B. Garret, *The 3D Printing Handbook: Technologies, Design and Applications*, 1st. 2017.

[26] O. A. Peverini, M. Lumia, G. Addamo, G. Virone, and N. J. G. Fonseca, « How 3D-printing is changing RF front-end design for space applications », *IEEE Journal of Microwaves*, vol. 3, *2*, pp. 800–814, 2023.

[27] O. Yurduseven, J. N. Gollub, D. L. Marks, and D. R. Smith, « Metallization of a 3D printed cavity for imaging », *2016 IEEE International Symposium on Antennas and Propagation (APSURSI)*, 2016, pp. 855–856.

[28] M. García-Vigueras, E. Menargues, T. Debogovic, J. Silva, A. Dimitriadis, S. Capdevila, J. R. Mosig, and E. de Rijk, « Mm-wave antennas and components: profiting from 3D-printing », *2017 International Conference on Electromagnetics in Advanced Applications (ICEAA)*, 2017, pp. 1016–1020.

[29] M. Hollenbeck, K. Wamick, C. Cathey, J. Opra, and R. Smith, « Selective laser melting aluminum waveguide attenuation at K-band », *2017 IEEE MTT-S International Microwave Symposium (IMS)*, 2017, pp. 45–47.

[30] T.-H. Chio, G.-L. Huang, and S.-G. Zhou, « Application of direct metal laser sintering to waveguide-based passive microwave components, antennas, and antenna arrays », *Proceedings of the IEEE*, vol. 105, *4*, pp. 632–644, 2017.

[31] T. Pereira, J. Kennedy, and J. Potgieter, « A comparison of traditional manufacturing vs additive manufacturing, the best method for the job », *Procedia Manufacturing*, vol. 30, pp. 11–18, Jan. 2019.

[32] *Metal 3D printing vs. traditional manufacturing: which should you choose?*, `https://www.thesteelprinters.com/news/metal-3d-printing-vs.-traditional-manufacturing-which-should-you-choose`.

[33] *Comparing traditional manufacturing vs additive manufacturing*, `https://www.linkedin.com/pulse/comparing-traditional-manufacturing-vs-additive-albert-sebastian/`, October 16, 2017.

[34] H. Fenech, Amos, Tomatis, and Soumpholphkakdy, « Ka-Sat and future HTS systems », *2013 IEEE 14th International Vacuum Electronics Conference (IVEC)*, 2013, pp. 1–2.

[35] E. Calà, M. Baldelli, A. Catalani, E. Menargues, G. Toso, and P. Angeletti, « Development of a Ka-band non-regular multibeam coverage antenna », *IEEE Transactions on Antennas and Propagation*, vol. 71, *1*, pp. 7–17, 2023.

[36] V. Griseri, « Behavior of dielectrics in a charging space environment and related anomalies in flight », *Dielectrics and Electrical Insulation, IEEE Transactions on*, vol. 16, pp. 689–695, Jul. 2009.

[37] Y. Zuo, J. Wang, S. Niu, and Y. Wei, « Simulations of internal charging effects of artificial radiation belt on dielectric material », *IEEE Transactions on Nuclear Science*, vol. 68, *5*, pp. 1120–1128, 2021.

[38] S. Rao, L. Shafai, and S. Sharma, *Handbook of Reflector Antennas and Feed Systems Volume I: Theory and Design of Reflectors*. Artech, 2013.

[39] S. Hay and T. Bird, « Applications of phased array feeders in reflector antennas ». Oct. 2016, pp. 3139–3187.

[40] S. Rao, « Design and analysis of multiple-beam reflector antennas », *IEEE Antennas and Propagation Magazine*, vol. 41, *4*, pp. 53–59, 1999.

[41] L. Lei, J. Wan, and Q. Gong, « Multibeam antennas with reflector for high throughput satellite applications », *IEEE Aerospace and Electronic Systems Magazine*, vol. 37, *2*, pp. 34–46, 2022.

[42] D. L. Doan, E. Amyotte, C. Mok, and J. Uher, « Anik-F2 Ka-band transmit multi-beam antenna », *2004 10th International Symposium on Antenna Technology and Applied Electromagnetics and URSI Conference*, 2004, pp. 1–4.

[43] *Ipstar-1* (*thaicom 4, measat 5, synertone 1*), `https://space.skyrocket.de/doc_sdat/ipstar-1.html`.

[44] *Eutelsat 172b*, `https://www.eutelsat.com/en/satellites/eutelsat-172-east.html`.

[45] E. Reiche and M. Schneider, « Challenges in the EM-based design of modern telecommunication satellite antennass », *COMPEL - The international journal for computation and mathematics in electrical and electronic engineering*, vol. 37, 2017, pp. 1461–1480.

[46] C. Leclerc, H. Aubert, M. Romier, and A. Annabi, « Design of multiple feed per beam antenna based on a 3D directional coupler topology », *2012 15 International Symposium on Antenna Technology and Applied Electromagnetics*, 2012, pp. 1–5.

[47] P. Angeletti and M. Lisi, « Multimode beamforming networks », *32nd ESA Antenna Workshop, Noordwijk, The Netherlands*, Aug. 2010.

[48] *Intelsat*, https://www.intelsat.com/.

[49] C. Wang, Y. Wang, P. Lian, S. Xue, Q. Xu, Y. Shi, Y. Jia, B. Du, J. Liu, and B. Tang, « Space phased array antenna developments: a perspective on structural design », *IEEE Aerospace and Electronic Systems Magazine*, vol. 35, *7*, pp. 44–63, 2020.

[50] D. Parker and D. Zimmermann, « Phased arrays - part I: theory and architectures », *IEEE Transactions on Microwave Theory and Techniques*, vol. 50, *3*, pp. 678–687, 2002.

[51] D. Parker and D. Zimmermann, « Phased arrays-part II: implementations, applications, and future trends », *IEEE Transactions on Microwave Theory and Techniques*, vol. 50, *3*, pp. 688–698, 2002.

[52] P. Angeletti and M. Lisi, « Multimode beamforming networks for space applications », *Antennas and Propagation Magazine, IEEE*, vol. 56, pp. 62–78, Feb. 2014.

[53] A. I. Zaghloul, F. T. Assal, and R. M. Sorbello, « Multibeam active phased array system configurations for communications satellites », *MILCOM 1987 - IEEE Military Communications Conference - Crisis Communications: The Promise and Reality*, vol. 1, 1987, pp. 0289–0293.

[54] L. Yu, J. Wan, K. Zhang, F. Teng, L. Lei, and Y. Liu, « Spaceborne multibeam phased array antennas for satellite communications », *IEEE Aerospace and Electronic Systems Magazine*, vol. 38, *3*, pp. 28–47, 2023.

[55] C. Wang, Y. Wang, P. Lian, S. Xue, Q. Xu, Y. Shi, Y. Jia, B. Du, J. Liu, and B. Tang, « Space phased array antenna developments: a perspective on structural design », *IEEE Aerospace and Electronic Systems Magazine*, vol. 35, *7*, pp. 44–63, 2020.

[56] M. Li, S.-L. Chen, Y. Liu, and Y. J. Guo, « Wide-angle beam scanning phased array antennas: a review », *IEEE Open Journal of Antennas and Propagation*, vol. 4, pp. 695–712, 2023.

[57] J. Schuss, J. Upton, B. Myers, T. Sikina, A. Rohwer, P. Makridakas, R. Francois, L. Wardle, and R. Smith, « The IRIDIUM main mission antenna concept », *IEEE Transactions on Antennas and Propagation*, vol. 47, *3*, pp. 416–424, 1999.

[58] F. Croq, E. Vourch, M. Reynaud, B. Lejay, C. Benoist, A. Couarraze, M. Soudet, P. Carati, J. Vicentini, and G. Mannocchi, « The GLOBALSTAR 2 antenna subsystem », *2009 3rd European Conference on Antennas and Propagation*, 2009, pp. 598–602.

[59] G. Toso, C. Mangenot, and A. Roederer, « Sparse and thinned arrays for multiple beam satellite applications », vol. 2007, Dec. 2007, pp. 1–4.

[60] G. Caille, Y. Cailloce, C. Guiraud, D. Auroux, T. Touya, and M. Masmousdi, « Large multibeam array antennas with reduced number of active chains », *The Second European Conference on Antennas and Propagation, EuCAP 2007*, 2007, pp. 1–9.

[61] T. Isernia, M. D'Urso, and O. M. Bucci, « A simple idea for an effective subarraying of large planar sources », *IEEE Antennas and Wireless Propagation Letters*, vol. 8, pp. 169–172, 2009.

[62] R. J. Mailloux, S. Santarelli, and T. M. Roberts, « Wideband arrays using irregular (polyomino) shaped subarrays », *Electronics Letters*, vol. 42, pp. 1019–1020, 2006.

[63] R. L. Haupt, « Adaptively thinned arrays », *IEEE Transactions on Antennas and Propagation*, vol. 63, *4*, pp. 1626–1632, 2015.

[64] R. Haupt, J. Menozzi, and C. McCormack, « Thinned arrays using genetic algorithms », *Proceedings of IEEE Antennas and Propagation Society International Symposium*, 1993, 712–715 vol.2.

[65] A. S. Karasev and M. A. Stepanov, « Genetic algorithm for antenna array thinning with minimization of side lobe level », *2021 XV International Scientific-Technical Conference on Actual Problems Of Electronic Instrument Engineering (APEIE)*, 2021, pp. 268–272.

[66] J. Belluot, G. L. Rhun, P. Augoyat, G. Mouchon, A. Maati, A. Katz, B. Gray, and R. Dorval, « A 40 W Ka-Band RF amplification chain for space telecommunication SSPA applications », *2019 49th European Microwave Conference (EuMC)*, 2019, pp. 404–407.

[67] *Analog Devices develops Ka-band beamformer ICs for aerospace and defense applications*, `https://www.everythingrf.com/News/details/12283-analog-devices-develops-ka-band-beamformer-ics-for-aerospace-and-defense-applications`, May 6, 2021 - Editorial Team.

[68] R. W. Kindt and B. T. Binder, « Dual-polarized Vivaldi array on a triangular lattice », *IEEE Transactions on Antennas and Propagation*, vol. 69, *4*, pp. 2083–2091, 2021.

[69] H. Kähkönen, J. Ala-Laurinaho, and V. Viikari, « A modular dual-polarized Ka-band Vivaldi antenna array », *IEEE Access*, vol. 10, pp. 36 362–36 372, 2022.

[70] R. W. Kindt and W. R. Pickles, « Ultrawideband all-metal flared-notch array radiator », *IEEE Transactions on Antennas and Propagation*, vol. 58, *11*, pp. 3568–3575, 2010.

[71] Y. Zhang, A. R. Vilenskiy, and M. V. Ivashina, « Wideband open-ended ridge gap waveguide antenna elements for 1D and 2D wide-angle scanning phased arrays at 100 GHz », *IEEE Antennas and Wireless Propagation Letters*, vol. 21, *5*, pp. 883–887, 2022.

[72] L. Sun, Y. Lu, L. Xu, Y. You, J. Xu, Y. Wang, and J. Huang, « All-metal phased array with full polarization reconfigurability », *IEEE Transactions on Antennas and Propagation*, vol. 71, *4*, pp. 3349–3360, 2023.

[73] L. Polo-López, E. Menargues, S. Capdevila, G. Toso, and M. García-Vigueras, « Solving sub-wavelength lattice reduction in full-metal front-ends for dual-polarized active antennas », *IEEE Transactions on Antennas and Propagation*, vol. 70, *9*, pp. 7413–7426, 2022.

[74] Y. Chairi, S. Abedrrabba, R. Allanic, A.-C. Amiaud, A. El Oualkadi, C. Quendo, T. Merlet, K. Reklaoui, and T. Le Gouguec, « Design of a slotted waveguide antenna based on TE20 mode in Ku-Band suitable for direct metal laser sintering », *Electronics*, vol. 11, p. 2079, Jul. 2022.

[75] C. Stoumpos, T. L. Gouguec, R. Allanic, M. García-Vigueras, and A.-C. Amiaud, « Compact additively manufactured conformal slotted waveguide antenna array », *IEEE Antennas and Wireless Propagation Letters*, vol. 22, *8*, pp. 1843–1847, 2023.

[76] E. Garcia-Marin, P. Sanchez-Olivares, J. L. Masa-Campos, J. A. Ruiz-Cruz, and J. Herranz-Alpanseque, « Dual circularly polarized waveguide array antenna formed by full-metallic bow-tie radiating cavities », *2020 14th European Conference on Antennas and Propagation (EuCAP)*, 2020, pp. 1–5.

[77] R. W. Kindt and B. T. Binder, « Wideband, low-profile, dual-polarized machined-metal array on a triangular lattice », *IEEE Transactions on Antennas and Propagation*, vol. 70, *2*, pp. 1097–1106, 2022.

[78] « Analysis and design of reflectarray elements », *Reflectarray Antennas*. John Wiley and Sons, Ltd, 2018, ch. 2, pp. 9–48.

[79] J. A. Encinar, C. Tienda, M. Barba, E. Carrasco, and M. Arrebola, « Analysis, design and prototyping of reflectarray antennas for space applications », *2013 Loughborough Antennas and Propagation Conference (LAPC)*, 2013, pp. 1–5.

[80] J. Velasco, I. Parellada-Serrano, and C. Molero, « Fully metallic reflectarray for the Ku-Band based on a 3D architecture », *Electronics*, vol. 10, *21*, 2021.

[81] Á. Palomares-Caballero, C. Molero, P. Padilla, M. García-Vigueras, and R. Gillard, « Wideband 3D-printed metal-only reflectarray for controlling orthogonal linear polarizations », *IEEE Transactions on Antennas and Propagation*, vol. 71, *3*, pp. 2247–2258, 2023.

[82] Y. H. Cho, W. J. Byun, and M. S. Song, « High gain metal-only reflectarray antenna composed of multiple rectangular grooves », *IEEE Transactions on Antennas and Propagation*, vol. 59, *12*, pp. 4559–4568, 2011.

[83] Z. An, T. Makdissy, M. G. Vigueras, S. Vaudreuil, and R. Gillard, « A metal-only reflectarray made of 3D phoenix cells », *2022 16th European Conference on Antennas and Propagation (EuCAP)*, 2022, pp. 1–5.

[84] H.-T. Chou, C.-Y. Lin, and M.-H. Wu, « A high efficient reflectarray antenna consisted of periodic all-metallic elements forthe Ku-band DTV applications », *IEEE Antennas and Wireless Propagation Letters*, vol. 14, pp. 1542–1545, 2015.

[85] I.-J. Nam, S. Lee, and D. Kim, « Miniaturized beam reconfigurable reflectarray antenna with wide 3D beam coverage », *IEEE Transactions on Antennas and Propagation*, vol. 70, *4*, pp. 2613–2622, 2022.

[86] Y.-H. Nam, Y. Kim, S.-G. Lee, and J.-H. Lee, « Hybrid reflectarray antenna of passive and active unit cells for highly directive two-direction beam steering », *IEEE Access*, vol. 11, pp. 6299–6304, 2023.

[87] J. R. Reis, M. Vala, and R. F. S. Caldeirinha, « Review paper on transmitarray antennas », *IEEE Access*, vol. 7, pp. 94 171–94 188, 2019.

[88] M. O. Bagheri, H. R. Hassani, and B. Rahmati, « Dual-band, dual-polarised metallic slot transmitarray antenna », *IET Microwaves, Antennas & Propagation*, vol. 11, *3*, pp. 402–409, 2017.

[89] X. Wang, Y. Cheng, and Y. Dong, « Millimeter-wave dual-polarized metal transmitarray antenna with wide gain bandwidth », *IEEE Antennas and Wireless Propagation Letters*, vol. 21, *2*, pp. 381–385, 2022.

[90] K. T. Pham, A. Clemente, E. Fourn, F. Diaby, L. Dussopt, and R. Sauleau, « Low-cost metal-only transmitarray antennas at Ka-band », *IEEE Antennas and Wireless Propagation Letters*, vol. 18, *6*, pp. 1243–1247, 2019.

[91] X. Zhao, C. Yuan, L. Liu, S. Peng, Q. Zhang, and H. Zhou, « All-metal transmitarray for circular polarization design using rotated cross-slot elements for high-power microwave applications », *IEEE Transactions on Antennas and Propagation*, vol. 65, *6*, pp. 3253–3256, 2017.

[92] W. Hu, J. Dong, Q. Luo, Y. Cai, X. Liu, L. Wen, W. Jiang, and S. Gao, « A wideband metal-only transmitarray with two-layer configuration », *IEEE Antennas and Wireless Propagation Letters*, vol. 20, *7*, pp. 1347–1351, 2021.

[93] W. Hu, J. Dong, Q. Luo, Y. Cai, X. Liu, L. Wen, W. Jiang, and S. Gao, « Demonstration of a wideband multipolarization transmitarray antenna for satellite communication », *Hindawi, International Journal of RF and Microwave Computer-Aided Engineering*, *1096-4290*, pp. 1347–1351, 2023.

[94] S. V. Hum and J. Perruisseau-Carrier, « Reconfigurable reflectarrays and array lenses for dynamic antenna beam control: a review », *IEEE Transactions on Antennas and Propagation*, vol. 62, *1*, pp. 183–198, 2014.

[95] F. A. Jenkins and H. E. White, « Fundamentals of optics », *McGraw-Hill New York, 4th ed*. 1976, pp. 1–7.

[96] C. Fernandes and E. Lima, « Dielectric lens antennas ». Sep. 2016, pp. 1001–1064.

[97] I. Munina, I. Grigoriev, G. O'donnell, and D. Trimble, « A review of 3D printed gradient refractive index lens antennas », *IEEE Access*, vol. 11, pp. 8790–8809, 2023.

[98] O. Björkqvist, O. Zetterström, and O. Quevedo-Teruel, « Additive manufactured dielectric Gutman lens », *Electronics Letters*, vol. 55, Dec. 2019.

[99] Q. Lou and Z. N. Chen, « Flat-focal-plane dual-metasurface lens for low scan loss and sidelobe level of a metalens antenna », *IEEE Transactions on Antennas and Propagation*, vol. 70, *10*, pp. 9849–9854, 2022.

[100] W. Kock, « Metal-lens antennas », *Proceedings of the IRE*, vol. 34, *11*, pp. 828–836, 1946.

[101] A. Dion, « A broadband compound waveguide lens », *IEEE Transactions on Antennas and Propagation*, vol. 26, *5*, pp. 751–755, 1978.

[102] W. Kock, « Path-length microwave lenses », *Proceedings of the IRE*, vol. 37, *8*, pp. 852–855, 1949.

[103] J. Ruze, « Wide-angle metal-plate optics », *Proceedings of the IRE*, vol. 38, *1*, pp. 53–59, 1950.

[104] G. Toso and P. Angeletti, « An optimal procedure for the design of discrete constrained lens antennas with minimized optical aberrations. part I: two-dimensional architectures », *Electronics*, vol. 11, *3*, 2022.

[105] Y.-J. Park and W. Wiesbeck, « Angular independency of a parallel-plate Luneburg lens with hexagonal lattice and circular metal posts », *IEEE Antennas and Wireless Propagation Letters*, vol. 1, pp. 128–130, 2002.

[106] H. Lu, Z. Liu, Y. Liu, H. Ni, and X. Lv, « Compact air-filled Luneburg lens antennas based on almost-parallel plate waveguide loaded with equal-sized metallic posts », *IEEE Transactions on Antennas and Propagation*, vol. 67, *11*, pp. 6829–6838, 2019.

[107] O. Quevedo-Teruel, J. Miao, M. Mattsson, A. Algaba-Brazalez, M. Johansson, and L. Manholm, « Glide-symmetric fully metallic Luneburg lens for 5G communications at Ka-band », *IEEE Antennas and Wireless Propagation Letters*, vol. 17, *9*, pp. 1588–1592, 2018.

[108] R. F. Rinehart, « A solution of the problem of rapid scanning for radar antennae », *Journal of Applied Physics*, vol. 19, *9*, pp. 860–862, Apr. 2004.

[109] J. Rico-Fernández, F. V. Vidarsson, M. Arrebola, N. J. G. Fonseca, and O. Quevedo-Teruel, « Compact and lightweight additive manufactured parallel-plate waveguide half-Luneburg geodesic lens multiple-beam antenna in the Ka-band », *IEEE Antennas and Wireless Propagation Letters*, vol. 22, *4*, pp. 684–688, 2023.

[110] N. J. Fonseca, Q. Liao, and O. Quevedo-Teruel, « The water drop lens: a modulated geodesic lens antenna based on parallel curves », *2018 International Symposium on Antennas and Propagation (ISAP)*, 2018, pp. 1–2.

[111] Q. Liao, N. J. G. Fonseca, and O. Quevedo-Teruel, « Compact multibeam fully metallic geodesic Luneburg lens antenna based on non-euclidean transformation optics », *IEEE Transactions on Antennas and Propagation*, vol. 66, *12*, pp. 7383–7388, 2018.

[112] W. Rotman and R. Turner, « Wide-angle microwave lens for line source applications », *IEEE Transactions on Antennas and Propagation*, vol. 11, *6*, pp. 623–632, 1963.

[113] A. Peterson and E. Rausch, « Scattering matrix integral equation analysis for the design of a waveguide Rotman lens », *IEEE Transactions on Antennas and Propagation*, vol. 47, *5*, pp. 870–878, 1999.

[114] N. J. G. Fonseca, S.-A. Gomanne, J. Rico-Fernández, P. Jankovic, J. Galdeano, G. Toso, P. Angeletti, M. Arrebola, and O. Quevedo-Teruel, « Fully-metallic additively manufactured monolithic double-ridged waveguide Rotman lens in the K/Ka-band », *Sensors*, vol. 23, *14*, 2023.

[115] K. V. Hoel, S. Kristoffersen, N. Jastram, and D. S. Filipovic, « 3D printed Rotman lens », *2017 47th European Microwave Conference (EuMC)*, 2017, pp. 125–128.

[116] E. Rausch, A. Peterson, and W. Wiebach, « Electronically scanned millimeter wave antenna using a Rotman lens », *Radar 97 (Conf. Publ. No. 449)*, 1997, pp. 374–378.

[117] F. V. Vidarsson, O. Zetterstrom, A. Algaba-Brazález, N. J. G. Fonseca, M. Johansson, L. Manholm, and O. Quevedo-Teruel, « Conformal parallel plate waveguide polarizer integrated in a geodesic lens antenna », *IEEE Transactions on Antennas and Propagation*, vol. 70, *11*, pp. 10 327–10 337, 2022.

[118] P. Castillo-Tapia, O. Zetterstrom, A. Algaba-Brazález, L. Manholm, M. Johansson, N. J. G. Fonseca, and O. Quevedo-Teruel, « Two-dimensional beam steering using a stacked modulated geodesic Luneburg lens array antenna for 5G and beyond », *IEEE Transactions on Antennas and Propagation*, vol. 71, *1*, pp. 487–496, 2023.

[119] G. León, O. Orgeira, N. J. G. Fonseca, and O. Quevedo-Teruel, « Stacked geodesic lenses for radar applications in the W-band », *2022 16th European Conference on Antennas and Propagation (EuCAP)*, 2022, pp. 1–5.

[120] P. Castillo-Tapia, Q. Liao, N. J. G. Fonseca, and O. Quevedo-Teruel, « Modulated geodesic lens antenna array », *2021 15th European Conference on Antennas and Propagation (EuCAP)*, 2021, pp. 1–4.

[121] D. Nussler, R. Brauns, and H.-H. Fuchs, « A two dimensional lens stack design for 94 GHz », *2009 German Microwave Conference*, 2009, pp. 1–4.

[122] G. Toso and P. Angeletti, « An optimal procedure for the design of discrete constrained lens antennas with minimized optical aberrations. part II: three-dimensional multifocal architectures », *Electronics*, vol. 11, *3*, 2022.

[123] D. McGrath, « Planar three-dimensional constrained lenses », *IEEE Transactions on Antennas and Propagation*, vol. 34, *1*, pp. 46–50, 1986.

[124] J. Rao, « Multifocal three-dimensional bootlace lenses », *IEEE Transactions on Antennas and Propagation*, vol. 30, *6*, pp. 1050–1056, 1982.

[125] G. Ruggerini, P. G. Nicolaci, G. Toso, and P. Angeletti, « A Ka-band active aperiodic constrained lens antenna for multibeam applications: active discrete lens antennas are promising alternative solutions for multibeam coverage using a single aperture », *IEEE Antennas and Propagation Magazine*, vol. 61, *5*, pp. 60–68, 2019.

[126] G. Ruggerini, G. Toso, and P. Angeletti, « A single aperture active aperidic lens for multibeam satellite applications », Jan. 2010.

[127] G. Ruggerini, P. G. Nicolaci, and G. Toso, « A Ku-band magnified active Tx/Rx multibeam antenna based on a discrete constrained lens », *Electronics*, vol. 10, *22*, 2021.

[128] A. A. Norman, S. Das, T. Rohr, and T. Ghidini, « Advanced manufacturing for space applications », *CEAS Space Journal*, vol. 15, *1868-2510*, 2023.

[129] E. Sacco and S. K. Moon, « Additive manufacturing for space: status and promises », *The International Journal of Advanced Manufacturing Technology*, vol. 105, *1433-3015*, 2019.

[130] R. Sorrentino and O. A. Peverini, « Additive manufacturing: a key enabling technology for next-generation microwave and millimeter-wave systems [point of view] », *Proceedings of the IEEE*, vol. 104, *7*, pp. 1362–1366, 2016.

[131] G.-L. Huang, S.-G. Zhou, T.-H. Chio, and T.-S. Yeo, « Fabrication of a high-efficiency waveguide antenna array via direct metal laser sintering », *IEEE Antennas and Wireless Propagation Letters*, vol. 15, pp. 622–625, 2016.

[132] A. I. Dimitriadis, T. Debogović, M. Favre, M. Billod, L. Barloggio, J.-P. Ansermet, and E. de Rijk, « Polymer-based additive manufacturing of high-performance waveguide and antenna components », *Proceedings of the IEEE*, vol. 105, *4*, pp. 668–676, 2017.

[133] R. Kronberger, S. Grünwald, V. Wienstroer, and V. Tsatsos, « New low-cost FDM technology for printing antennas », *2020 International Symposium on Antennas and Propagation (ISAP)*, 2021, pp. 571–572.

[134] E. De Rijk, M. Favre, M. Billod, and A. Dimitriades, *Waveguide device comprising a core having a waveguide channel, where a smoothing layer and a conductive layer of at least 5 skin depth are formed on an inner surface of the waveguide channel*, Patent 10862186, Dec. 8th 2020.

[135] M. Billod, *Method for manufacturing a waveguide device by additive manufacturing and electrodeposition, and semi-finished product*, US Patent 17/596660 Sept. 22nd 2022.

[136] M. García-Vigueras, L. Polo-Lopez, C. Stoumpos, A. Dorlé, C. Molero, and R. Gillard, « Metal 3D-printing of waveguide components and antennas: guidelines and new perspectives », *Hybrid Planar*, M. D. Fernandez, J. A. Ballesteros, H. Esteban, and Á. Belenguer, Eds., Rijeka: IntechOpen, 2022, ch. 6.

[137] G. C. Sole and M. S. Smith, « Multiple beam forming for planar antenna arrays using a three-dimensional Rotman lens », 1987.

[138] J. L. McFarland and J. Ajioka, « Multiple beam constrained lenses », *Microwaves*, *2*, pp. 81–89, 1963.

[139] J. B. L. Rao, « Bisherical constrained lens antenna », *IEEE Transactions on Antennas and Propagation*, vol. 30, pp. 1224–1228, 1986.

[140] J. Lizarraga, G. Crespo, and C. del-Río, « Discrete lenses for multibeam applications », *Proceedings of the 5th European Conference on Antennas and Propagation (EUCAP)*, 2011, pp. 3513–3517.

[141] D. Archer and M. Maybell, « Rotman lens development history at Raytheon Electronic warfare systems 1967-1995 », *2005 IEEE Antennas and Propagation Society International Symposium*, vol. 2B, 2005, 31–34 vol. 2B.

[142] C. Sciannella and G. Toso, « Imaging antenna systems with compensated optical aberrations based on unshaped surface reflectors », *International Patent US20160372835A1*, Publication Date: 22.09.2015 International Filing Date: 05.03.2014.

[143] C. Sciannella and G. Toso, « An imaging reflector system with reduced scanning aberrations », *IEEE Transactions on Antennas and Propagation*, vol. 63, *4*, pp. 1342–1350, 2015.

[144] A. K. Pandey, « Design of multimode tracking system for earth station antenna », *2016 Asia-Pacific Microwave Conference (APMC)*, 2016, pp. 1–4.

[145] A. Mallet, A. Anakabe, J. Sombrin, and R. Rodriguez, « Multiport-amplifier-based architecture versus classical architecture for space telecommunication payloads », *IEEE Transactions on Microwave Theory and Techniques*, vol. 54, *12*, pp. 4353–4361, 2006.

[146] A. B. Numan, J.-F. Frigon, and J.-J. Laurin, « Printed W-band multibeam antenna with Luneburg lens-based beamforming network », *IEEE Transactions on Antennas and Propagation*, vol. 66, *10*, pp. 5614–5619, 2018.

[147] M. Elmusrati and V. Hasu, « Random switched beamforming for uplink wireless sensor networks », *2007 IEEE 65th Vehicular Technology Conference - VTC2007-Spring*, 2007, pp. 3150–3154.

[148] N. A. Sutton and D. S. Filipovic, « V-band monolithically integrated four-arm spiral antenna and beamforming network », *Proceedings of the 2012 IEEE International Symposium on Antennas and Propagation*, 2012, pp. 1–2.

[149] E. Menargues, M. García-Vigueras, S. Capdevila, P. Angeletti, and G. Toso, « Meandered waveguides for active antennas », *2021 15th European Conference on Antennas and Propagation (EuCAP)*, 2021, pp. 1–5.

[150] D. W. Woo, K. Oh, and D. K. Kong, « Hybrid waveguide feed network for aperiodic subarray beamforming », *IEEE Antennas and Wireless Propagation Letters*, pp. 1–5, 2022.

[151] K. Ding, X. Fang, Y. Wang, and A. Chen, « Printed dual-layer three-way directional coupler utilized as 3×3 beamforming network for orthogonal three-beam antenna array », *IEEE Antennas and Wireless Propagation Letters*, vol. 13, pp. 911–914, 2014.

[152] S.-K. Zhao, M. Lv, Z.-y. Zhang, Q. Chen, and G. Fu, « Planar two-dimensional scanning multibeam array antenna based on a 3×3 Butler matrix network », *IEEE Antennas and Wireless Propagation Letters*, vol. 21, *6*, pp. 1163–1167, 2022.

[153] A. Le Pera, I. Morris, G. Thomas, P. James, N. Wheatley, and P. Jung, « Novel spread spectrum approach to multi-port amplifier calibration », *2014 7th Advanced Satellite Multimedia Systems Conference and the 13th Signal Processing for Space Communications Workshop (ASMS/SPSC)*, 2014, pp. 346–351.

[154] C. Koenen, U. Siart, T. F. Eibert, G. D. Conway, and U. Stroth, « Design of a millimeter-wave phased array antenna for Gaussian beam shaping and steering », *2016 IEEE International Symposium on Phased Array Systems and Technology (PAST)*, 2016, pp. 1–4.

[155] N. J. G. Fonseca, S.-A. Gomanne, P. Castillo-Tapia, O. Quevedo-Teruel, T. Tomura, and J. Hirokawa, « Connecting networks for two-dimensional Butler matrices generating a triangular lattice of beams », *IEEE Journal of Microwaves*, vol. 1, *2*, pp. 646–658, 2021.

[156] Y. Quan, H. Wang, S. Tao, and J. Yang, « A double-layer multibeam antenna with 45° linear polarization based on gap waveguide technology », *IEEE Transactions on Antennas and Propagation*, vol. 70, *1*, pp. 56–66, 2022.

[157] J. Fan, Z. Liu, J. Zhao, P. Zhen, H. Lu, Y. Liu, and X. Lv, « Millimeter-wave multimode beamforming network based on double-ridged waveguides », *2021 International Conference on Microwave and Millimeter Wave Technology (ICMMT)*, 2021, pp. 1–3.

[158] J.-W. Lian, Y.-L. Ban, Q.-L. Yang, B. Fu, Z.-F. Yu, and L.-K. Sun, « Planar millimeter-wave 2D beam-scanning multibeam array antenna fed by compact SIW beamforming network », *IEEE Transactions on Antennas and Propagation*, vol. 66, *3*, pp. 1299–1310, 2018.

[159] I. Lima de Paula, S. Lemey, D. Bosman, Q. V. d. Brande, O. Caytan, J. Lambrecht, M. Cauwe, G. Torfs, and H. Rogier, « Cost-effective high-performance air-filled SIW antenna array for the global 5G 26 GHz and 28 GHz bands », *IEEE Antennas and Wireless Propagation Letters*, vol. 20, *2*, pp. 194–198, 2021.

[160] A. Vafadar, F. Guzzomi, A. Rassau, and K. Hayward, « Advances in metal additive manufacturing: a review of common processes, industrial applications, and current challenges », *Applied Sciences*, vol. 11, *3*, 2021.

[161] *Council of europe contribution to the united nations 2030 agenda for sustainable development goals*, `https://www.coe.int/en/web/un-agenda-2030/home?desktop=true`.

[162] B. Zhang and H. Zirath, « Metallic 3D printed rectangular waveguides for millimeter-wave applications », *IEEE Transactions on Components, Packaging and Manufacturing Technology*, vol. 6, *5*, pp. 796–804, 2016.

[163] Axone, *Microwave coaxial assemblies*, https://www.axon-cable.com/publications/axon-microwave-assemblies_cg.pdf.

[164] F. Parment, A. Ghiotto, T.-P. Vuong, J.-M. Duchamp, and K. Wu, « Air-filled substrate integrated waveguide for low-loss and high power-handling millimeter-wave substrate integrated circuits », *IEEE Transactions on Microwave Theory and Techniques*, vol. 63, *4*, pp. 1228–1238, 2015.

[165] A. Iliev, N. Kyurkchiev, and S. Markov, « On the approximation of the cut and step functions by logistic and Gompertz functions », *BIOMATH*, vol. 4, Oct. 2015.

[166] A. J. Hanson and H. Ma, « Parallel transport approach to curve framing », Tech. Rep., 1995.

[167] « Framing parametric curves », Tech. Rep., 30 Jun 2017.

[168] D. Carl, *The parallel transport frame* (Ed. Game programming Gems 2). Mark DeLouraCharles River Media, 2001.

[169] J. Ryan, *How to select antenna front-end components for non-GEO space applications*, 1st Jan 2023.

[170] A. Bhattacharyya and G. Goyette, « A novel horn radiator with high aperture efficiency and low cross-polarization and applications in arrays and multibeam reflector antennas », *IEEE Transactions on Antennas and Propagation*, vol. 52, *11*, pp. 2850–2859, 2004.

[171] C. Stoumpos, J.-P. Fraysse, G. Goussetis, R. Sauleau, and H. Legay, « Quadfurcated profiled horn: the next generation highly efficient GEO antenna in additive manufacturing », *IEEE Open Journal of Antennas and Propagation*, vol. 3, pp. 69–82, 2022.

[172] G. Ruggerini, « A compact circular horn with high efficiency », *Proceedings of the Fourth European Conference on Antennas and Propagation*, 2010, pp. 1–3.

[173] V. Pascale, D. Maiarelli, L. D'Agristina, and N. Gatti, « Design and qualification of Ku-band-radiating chains for receive active array antennas of flexible telecommunication satellites », *International Journal of Microwave and Wireless Technologies*, vol. 12, *6*, pp. 487–503, 2020.

[174] A. Bhattacharyya, *Phased Array Antennas: Floquet Analysis, Synthesis, BFNs, and Active Array Systems*. Wiley-Interscience, 2006.

[175] M. H. Dahri, M. H. Jamaluddin, F. C. Seman, M. I. Abbasi, N. F. Sallehuddin, A. Y. I. Ashyap, and M. R. Kamarudin, « Aspects of efficiency enhancement in reflectarrays with analytical investigation and accurate measurement », *Electronics*, vol. 9, *11*, 2020.

[176] S. D'Addio, P. Angeletti, N. Ayllon, I. Davies, V. Valenta, B. Cortazar, F. Deborgies, B.-M. Folio, G. Toso, N. Fonseca, and C. Ernst, « Technology developments and R&D activities at the European Space Agency for satellite communication payloads based on active antennas and digital processors », *2022 IEEE International Symposium on Phased Array Systems & Technology (PAST)*, 2022, pp. 1–6.

[177] I. Merino-Fernandez, S. L. Khemchandani, J. del Pino, and J. Saiz-Perez, « Phased array antenna analysis workflow applied to gateways for LEO satellite communications », *Sensors*, vol. 22, *23*, 2022.

[178] M. Henderson, M. B. Davis, and M. Huisjen, « GDPAA advanced technology demonstration overview and results », *2010 IEEE International Symposium on Phased Array Systems and Technology*, 2010, pp. 140–143.

[179] G. Toso and P. Angeletti, « An optimal procedure for the design of discrete constrained lens antennas with minimized optical aberrations. part III: three-dimensional architectures with an extended field of view », *Electronics*, vol. 11, *3*, 2022.

[180] R. Mailloux, *Phased Array Antenna Handbook, Third Edition*. Artech House classic, 2017.

[181] P. Angeletti, F. Frezza, R. Vescovo, and G. Toso, « On the directivity of planar arrays with cosq(theta) element patterns », May 2008, pp. 27–30.

[182] M. Maybell, « Ray structure method for coupling coefficient analysis of the two dimensional Rotman lens », *1981 Antennas and Propagation Society International Symposium*, vol. 19, 1981, pp. 144–147.

[183] L. Sun, Y. Li, Z. Zhang, and H. Wang, « Antenna decoupling by common and differential modes cancellation », *IEEE Transactions on Antennas and Propagation*, vol. 69, *2*, pp. 672–682, 2021.

[184] H. Bilel and A. Taoufik, « Intuition and symmetries in electromagnetism: eigenstates of four antennas », *Applied Sciences*, vol. 12, *23*, 2022.

[185] D. Crouch, « On the use of symmetry to reduce the computational requirements for FDTD analyses of finite phased arrays », *Microwave and Optical Technology Letters*, vol. 13, *3*, pp. 123–128, 1996.

List of Figures

List of Tables

Résumé étendu

Aujourd'hui, l'industrie spatiale connaît un changement radical qui s'inscrit dans le paradigme du New Space comme un pas en avant en termes de débits très élevés, de connectivité des réseaux, de fiabilité et de haute efficacité, mais aussi une démocratisation de l'espace et l'apparition de constellations de petits satellites [1]–[4].

La flexibilité est devenue une priorité dans la conception des systèmes radiofréquences (RF), principalement en termes de couverture, d'allocation de puissance, d'utilisation du spectre, de polarisation et de nombre et de forme des faisceaux. Cette flexibilité est nécessaire à la fois au niveau terrestre et non terrestre [5]–[7]. La reconfiguration multifaisceaux, les techniques de saut de faisceau, la réutilisation des fréquences et de la polarisation sont en effet sur le point de devenir quelques-unes des exigences des systèmes émergents [8]–[10]. En plus de cette flexibilité, la gestion d'une puissance élevée est une exigence supplémentaire pour les applications spatiales. En effet, il est nécessaire d'assurer un budget de liaison avec le satellite. Le rôle et la position de l'antenne sont donc cruciaux dans la conception de ces systèmes et représentent en particulier l'une des motivations de la thèse.

La solution offrant la plus grande flexibilité est l'Antenne Active électroniquement reconfigurable (AA). Contrairement aux antennes passives, les AAs permettent une reconfiguration électronique (sans pièces mécaniques mobiles) de la mission (c'est-à-dire un nombre flexible de faisceaux et, pour chaque faisceau, une orientation flexible, une forme flexible du faisceau ou une allocation flexible de la puissance). Nous assistons actuellement à une tendance commune dans l'industrie spatiale, liée au développement de systèmes flexibles (par exemple Eutelsat Quantum [11], Hispasat 36W-1 [12], OneSat [13], HummingSat [14] (Europe) ou Winds [15] (Japon)). De même, ces nouvelles solutions basées sur les AAs ont été introduites pour les applications terrestres (par exemple, le nouveau concept de réseaux de Thinkom [16], Starlink [17]). Toutefois,

l'introduction de ces caractéristiques entraîne une augmentation des coûts de fabrication et de la complexité de l'intégration de l'amplification, des modules de refroidissement, du traitement numérique et des blocs de calibration en temps réel. Il y a aussi une augmentation des pertes et de la consommation d'énergie.

Le défi de rendre les AAs plus abordables est une grande source de motivation, tant au niveau de l'industrie que de la recherche. Des efforts sont faits pour réduire leur complexité et augmenter leur efficacité énergétique, par exemple en utilisant des réseaux lacunaires ou irréguliers [18], [19], des charges utiles hybrides [20] ou encore en améliorant la technologie GaN [21].

En ce qui concerne la fabrication, la fabrication additive (FA) ou l'impression 3D [23]–[25] a été identifiée comme l'une des technologies habilitantes qui peuvent contribuer à faciliter le développement des AAs [26]. L'exploration du potentiel de la FA est une autre motivation de la thèse.

L'utilisation des techniques FA dans la conception de composants RF a représenté une opportunité attrayante d'atteindre une plus grande liberté de conception, mais aussi de réduire le volume et les coûts et d'améliorer les performances RF. Cette évolution va de l'application de revêtements métalliques sur des composants en plastique imprimés en 3D, tels que ceux produits par stéréolithographie [27], [28], à l'émergence de méthodes de FA entièrement métalliques telles que la fusion sélective par laser [29] et le frittage direct de métaux par laser [30]. Ces méthodes avancées atteignent des degrés élevés de flexibilité, permettant l'intégration de géométries complexes dans des composants monoblocs tout en réduisant les pertes, en économisant de l'énergie et en permettant une utilisation à forte puissance - une capacité que les approches de fabrication conventionnelles ne peuvent pas reproduire [31]–[33].

Cette thèse vise à proposer des solutions innovantes d'AAs avec un coût et une flexibilité réduits. Les principaux objectifs sont les suivants :

- concevoir des antennes multifaisceaux à gain élevé;
- développer des systèmes à faibles pertes et à haut rendement;
- permettre une double polarisation et des capacités de large bande;
- améliorer la capacité et simplifier l'adaptation du système.

Le travail présenté dans cette thèse est basé sur l'hypothèse que l'exploitation des lentilles discrètes 3D fabriquées avec la FA, peut conduire à des AAs avec un coût réduit et une grande flexibilité. Ces systèmes peuvent prendre en charge de grandes largeurs de bande de fréquence et permettre des caractéristiques de double polarisation. En

outre, ils peuvent être utilisés dans divers scénarios, couvrant à la fois les champs de vision réduits et larges. Des lentilles discrètes en 3D ont été proposées dans la littérature [22] et représentent une solution prometteuse à explorer car elles offrent un compromis entre complexité et flexibilité.

Une représentation générique d'une lentille discrète 3D est présentée en Fig. 4.16 pour générer des faisceaux pointant dans des directions multiples telles que : dans la directions normale (faisceau $\#1$), dans le plan horizontal (faisceau $\#2$) et dans un plan oblique générique (faisceau $\#3$).

En général, ces systèmes de focalisation (déjà examinés dans [22]) sont principalement caractérisés par la cascade de blocs multiples, comme décrit ci-après :

- un réseau rayonnant avant (en bleu) de diamètre D_A pour obtenir le pointage du faisceau dans les directions souhaitées;
- un bloc de lignes à retard pour relier les réseaux arrière et avant (lignes noires en pointillés dans le bloc gris);
- un réseau arrière (en rouge) de diamètre D_B éclairé par les sources sélectionnées;
- un réseau de sources placés dans les points focaux (en vert).

Contrairement aux lentilles diélectriques ou aux antennes à réflecteur, les lentilles discrètes 3D effectuent la collimation (pour la transmission) et la focalisation (pour la réception) de manière discrète en utilisant des réseaux d'antennes arrière et avant (en rouge et en bleu respectivement). Essentiellement à travers ces systèmes, l'onde incidente ne suit pas nécessairement la loi de Snell lorsqu'elle passe à travers les réseaux de lentilles. Au lieu de cela, elle est contrainte de suivre les lignes de retard, telles que définies par les points reliés par des lignes en pointillés dans la Fig. 4.16. Par exemple, lors de la transmission, l'onde sphérique incidente provient de l'alimentation et se propage vers le réseau arrière, qui transfère ensuite l'énergie au réseau avant par l'intermédiaire de lignes de retard effectuant les retards de phase appropriés.

Diverses technologies peuvent être utilisées pour créer ces lignes à retard, notamment les câbles coaxiaux [126], les guides d'ondes métalliques [140] et les lignes microrubans [123]. Cependant, puisque une solution entièrement métallique a été envisagée, les lignes à retard réalisées par des guides d'ondes en FA sont considérées. Ce choix est motivé par leur capacité à présenter de faibles pertes de signal et à gérer efficacement des niveaux de puissance élevés, ce qui en fait un choix pertinent pour l'étude de la thèse.

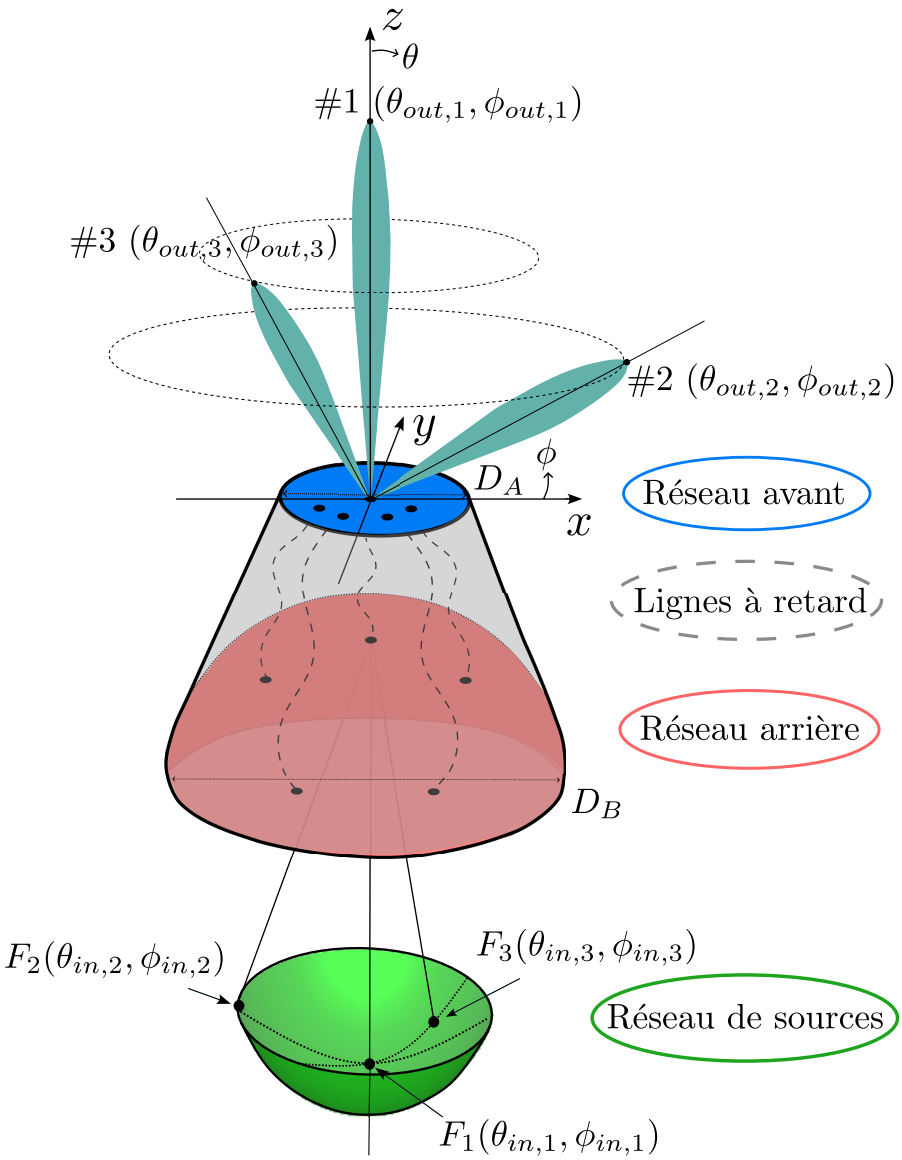

Figure 4.16 – Représentation d'une lentille discrète en 3D, comprenant un réseau avant (en bleu), un réseau arrière (en rouge), un bloc de lignes à retard (en gris) et un réseau d'alimentation (en vert).

La première partie de la thèse se concentre sur les guides d'ondes à méandres en tant que solution innovante employée dans les lentilles métalliques 3D discrètes pour permettre le routage spatial entre les deux réseaux avant et arrière. Ils peuvent atteindre une flexibilité très élevée et de faibles pertes le long de leurs chemins modulés reliant deux points arbitraires. Tout d'abord, les points généraux pour construire les trajectoires modulées sont mis en évidence. Ensuite, la synthèse du retard de phase est effec-

tuée, en proposant des exemples de méandres exotiques et en comparant les résultats attendus et simulés. En outre, quelques implémentations de guides d'ondes à méandres par la conception de cluster 3D à faibles pertes sont présentées, comme visualisé en Fig. 4.17. Le cluster de guides d'ondes méandrés permet en effet de connecter des réseaux ayant des périodicités différentes.

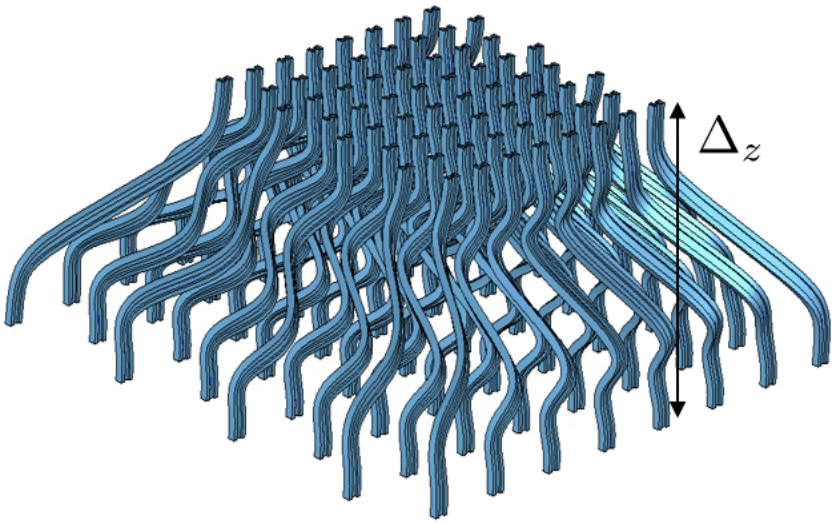

Figure 4.17 – Vue en perspective d'un cluster de guide d'ondes en méandres dans le logiciel électromagnétique CST avec avec une hauteur entre les profils de $\Delta_z = 10\lambda_0$.

Concernant les réseaux avant et arrière de la lentille 3D, il y a la possibilité d'introduire un facteur de zoom entre eux, dans le dimensionnement de la lentille. Le facteur M permet notamment de régler la taille du réseau arrière quand la surface du réseau avant a été choisie ou viceversa. Avec M, la relation entre l'angle d'entrée maximum θ_{in}^{max} et le correspondant angle de sortie θ_{out}^{max} est donnée par :

$$\sin(\theta_{out}^{max}) = M \cdot \sin(\theta_{in}^{max}) \tag{4.4}$$

La Fig. 4.18 illustre l'impact de ce facteur de zoom M sur les performances radiatives de la lentille, lorsque les dimensions du réseau avant (D_A) et l'angle d'entrée (θ_{in}^{max}) sont fixés.

Lorsque $M = 1$ dans la Fig. 4.18a, les tailles des réseaux avant et arrière sont sensiblement les mêmes et il n'y a pas de variation du champ de vision du système $(\theta_{out}^{max} = \theta_{in}^{max})$. En choisissant $M < 1$ (voir Fig. 4.18b), la taille de la partie arrière de la lentille est diminuée mais le champ de vision est aussi réduit $(\theta_{out}^{max} < \theta_{in}^{max})$. A

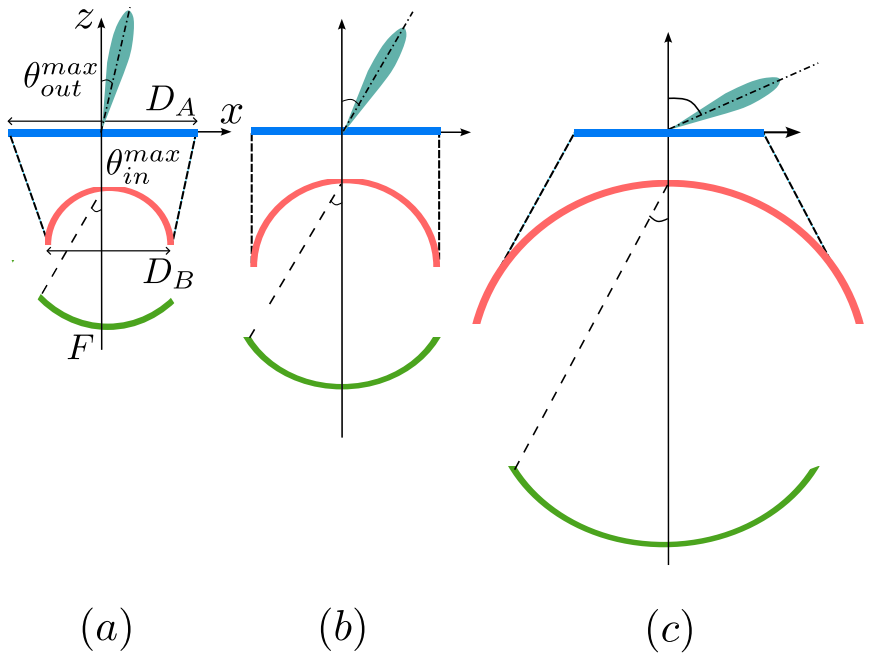

Figure 4.18 – Représentation bi-dimensionnelle d'une lentille discrète 3D pour : (a) $M < 1$, (b) $M = 1$, (c) $M > 1$.

l'inverse, pour $M > 1$ en Fig. 4.18c, il y a une augmentation de la taille de la partie arrière mais également une augmentation de la possibilité de balayage ($\theta_{out}^{max} > \theta_{in}^{max}$). Il est important de noter que le facteur de zoom s'applique à n'importe quelle forme de profil avant ou arrière.

Par conséquent, lors de la conception d'une lentille discrète 3D, il est possible de choisir différentes options sur le facteur de zoom en fonction du scénario d'application particulier. Ce choix tient compte de facteurs tels que le balayage dans le champ de vision et l'encombrement de l'ensemble du système. C'est pourquoi deux scénarios d'application différents ont été identifiés dans cette thèse, afin de démontrer la flexibilité du facteur de zoom dans les lentilles discrètes 3D.

Un premier exemple analysé et développé de cette thèse concerne la conception de lentilles discrètes 3D pour une application satellite géostationnaire avec un champ de vision réduit à $\pm 8°$, en fixant effectivement l'angle de sortie maximal à $\theta_{out}^{max} = 8°$. Dans ce cas, un facteur de zoom inférieur à un est choisi afin de réduire le volume de la lentille. $M = 0.5$ a donc été selectioné. Pour ces valeurs, l'angle d'entrée correspondant est $\theta_{in}^{max} = 16.2°$ (calculé à partir de $\sin(\theta_{in}^{max}) = \sin(\theta_{out}^{max})/M$) [122]). Bien sûr, la taille du réseau avant est deux fois plus grande que celle arrière.

Une lentille discrète 3D avec ce facteur de zoom entre les réseaux plats avant et arrière, incluant le cluster des guides d'ondes à méandres, est conçue dans un système de 7x7 éléments et simulée dans toutes ses parties (voir Fig. 4.19) pour valider l'analyse.

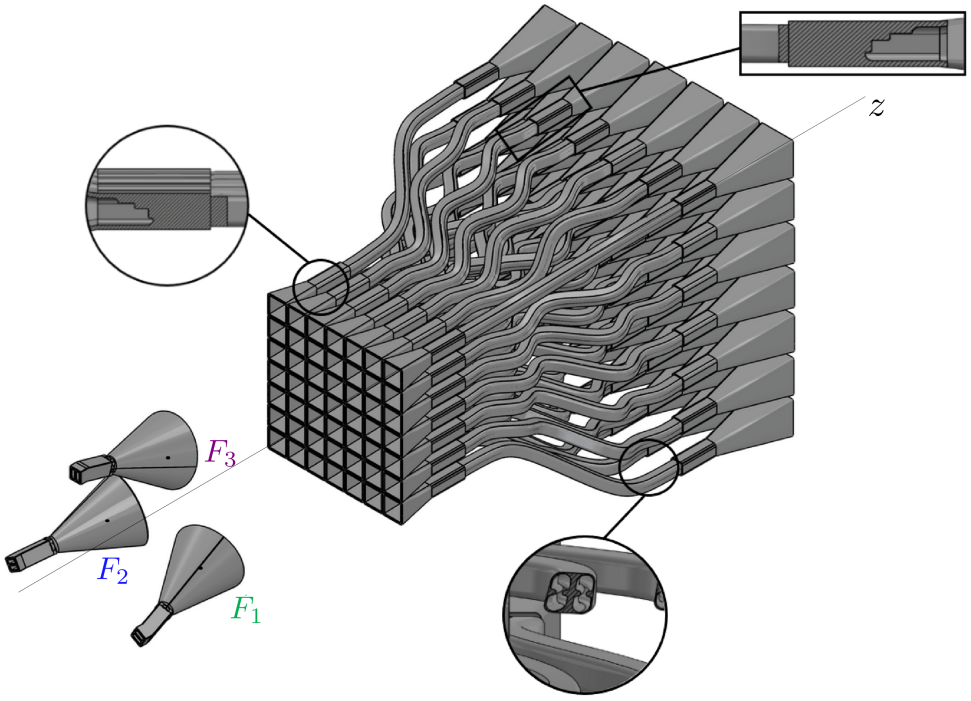

Figure 4.19 – Modèle CST à 7×7 de l'antenne 3D à lentille discrète avec $M = 0.5$ en incluant le cluster des guides d'ondes à méandres et 3 sources (F_1, F_2, F_3).

Un prototype plus petit de lentille 3x3 est également realisé par FA (voir Fig. 4.20) et mesuré, montrant les performances réelles atteintes de focalisation.

Un deuxième exemple concerne la conception d'une lentille discrète en 3D dans la technologie des guides d'ondes, destinée à des applications à large champ de vision telles que les antennes au sol ou les satellites en orbite basse. Cette fois, en choisissant un facteur de zoom supérieur à un, il est possible d'élargir le champ de vision par rapport à l'entrée, mais un agrandissement de la taille du réseau arrière ne peut pas être évité. Un exemple de lentilles discrètes 3D a été analysé et permet d'atteindre $\theta_{out}^{max} = 70°$ de balayage pour toutes les directions. Le facteur de zoom a été choisi égal à $M = 2$. En théorie, pour atteindre de larges angles de balayage, un très grand réseau doit être envisagé avec une faible périodicité, comme illustré en Fig. 4.21 où le réseau avant est affiché.

Pour cette raison, afin de réduire la charge de calcul en simulation électromagné-

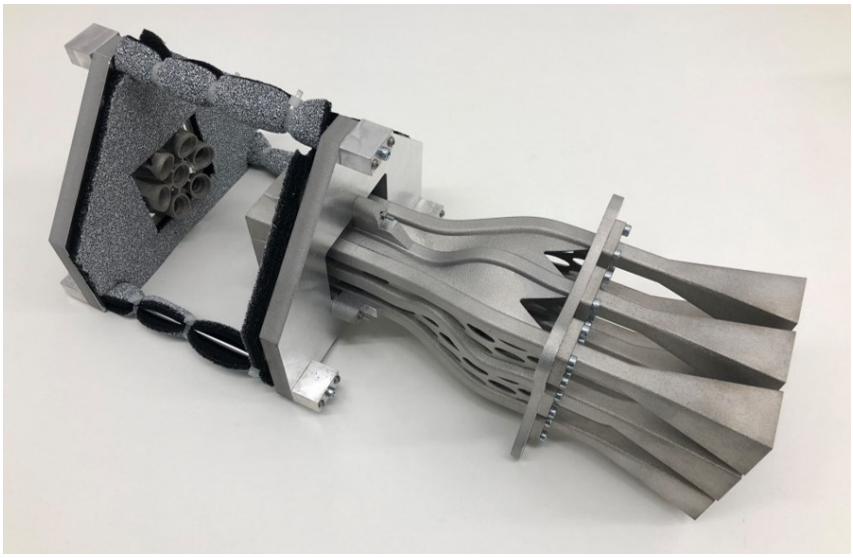

Figure 4.20 – Prototype de 3×3 lentille 3D fabriqué à l'aide de la FA.

tique, une méthodologie rigoureuse exploitant différents types de symétries et une analyse en mode pair/impair pour la simulation des grand réseaux est également proposée, comme illustré en Fig. 4.21.

Dans l'analyse du systeme entier, l'optique géométrique est adoptée pour le réseau arrière et la simulation électromagnétique rigoureuse est utilisée pour le vaste réseau avant afin de créer des lentilles discrètes 3D purement métalliques avec des faisceaux pointant jusqu'à $70°$.

De très bons résultats sont obtenus pour des lentilles discrètes en 3D exploitant le facteur de zoom, dans des scénarios de balayage réduits et larges. Ces systèmes, comprenant des clusters de guides sinueux pour fournir les retards de phase souhaités pour la focalisation, représentent une solution innovante pouvant être fabriqué de manière monolithique en métal grâce à la FA.

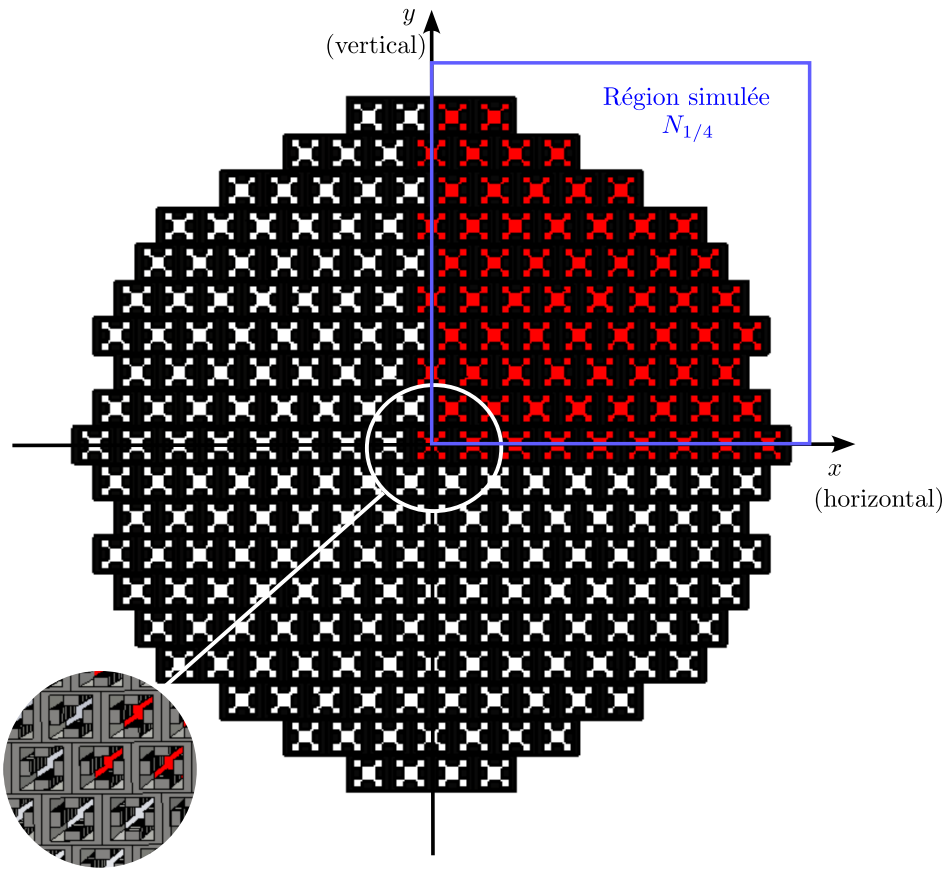

Figure 4.21 – Réseau avant avec des anneaux $n_r = 8$, periodicité $P = 0,56\lambda_0$ et un diamètre de $D_A = 8,96\lambda_0$ permettant un balayage jusqu'à $\theta_{out}^{max} = 70°$.

COLLEGE DOCTORAL BRETAGNE
MATHS, TELECOMS
INFORMATIQUE, SIGNAL
SYSTEMES, ELECTRONIQUE

INSA INSTITUT NATIONAL DES SCIENCES APPLIQUÉES RENNES

Titre : Antennes basées sur des lentilles discrètes tridimensionnelles purement métalliques : fabrication additive et applications spatiales.

Mot clés : Antenne active, fabrication additive, guide d'ondes à méandres, lentille discrète 3D.

Résumé : Cette thèse est réalisée en partenariat avec l'Agence Spatiale Européenne (ESA) et l'entreprise SWISSto12, dans le cadre d'une activité OSIP de l'ESA. Le travail concerne le développement d'éléments rayonnants pour des systèmes actifs de télécommunications destinés à des applications spatiales. Dans ce contexte, la conception d'antennes et de composants radio-fréquences à faibles pertes, à haute tenue en puissance et à intégration simplifiée est adressée. La structure de ces composants est spécialement conçue pour pouvoir les fabriquer à l'aide des nouvelles technologies de fabrication additive métallique, alternative aux méthodes de fabrication traditionnelle offrant moins de degrés de liberté.

Le concept développé est exploité pour le prototypage de lentilles 3D discrètes entièrement en métal, intégrant des guides d'ondes à méandres pour le routage des signaux au sein de la lentille. Ces systèmes offrent la possibilité d'une variation du champ de vision de l'antenne, une capacité de balayage multifaisceaux, ainsi qu'une double polarisation et un fonctionnement à large bande passante.

Title: Full-metal antennas based on magnified 3D discrete lenses: additive manufacturing and space applications.

Keywords: Active antenna, additive manufacturing, meandered waveguide, 3D discrete lens.

Abstract: This thesis is carried out in partnership with the European Space Agency (ESA) and the company SWISSto12, as part of an ESA OSIP activity. The work concerns the development of radiating elements in active telecommunications systems for space applications. In this context, the design of low loss, high efficiency antennas and radio-frequency components with simplified integration has been addressed. The structure of these components is specially designed to be manufactured using new full-metal additive manufacturing technologies, as an alternative to traditional subtractive manufacturing methods.

The concept has been adapted for the prototyping of full-metal 3D discrete lenses, incorporating meandered waveguides for phase routing between the radiating profiles. These systems offer the possibility of varying the field of view of the antenna depending on the application, multibeam scanning, as well as dual polarization and broad bandwidth capabilities.